AD-A069 619 PENNSYLVANIA STATE UNIV UNIVERSITY PARK APPLIED RESE--ETC F/G 20/4
INVESTIGATION OF THE UNSTEADY PRESSURE DISTRIBUTION ON THE BLAD--ETC(U)
NOV 78 G FRANKE N00024-79-C-6043
UNCLASSIFIED ARL/PSU/TM-78-300 NL

1 OF 2
AD
A069619

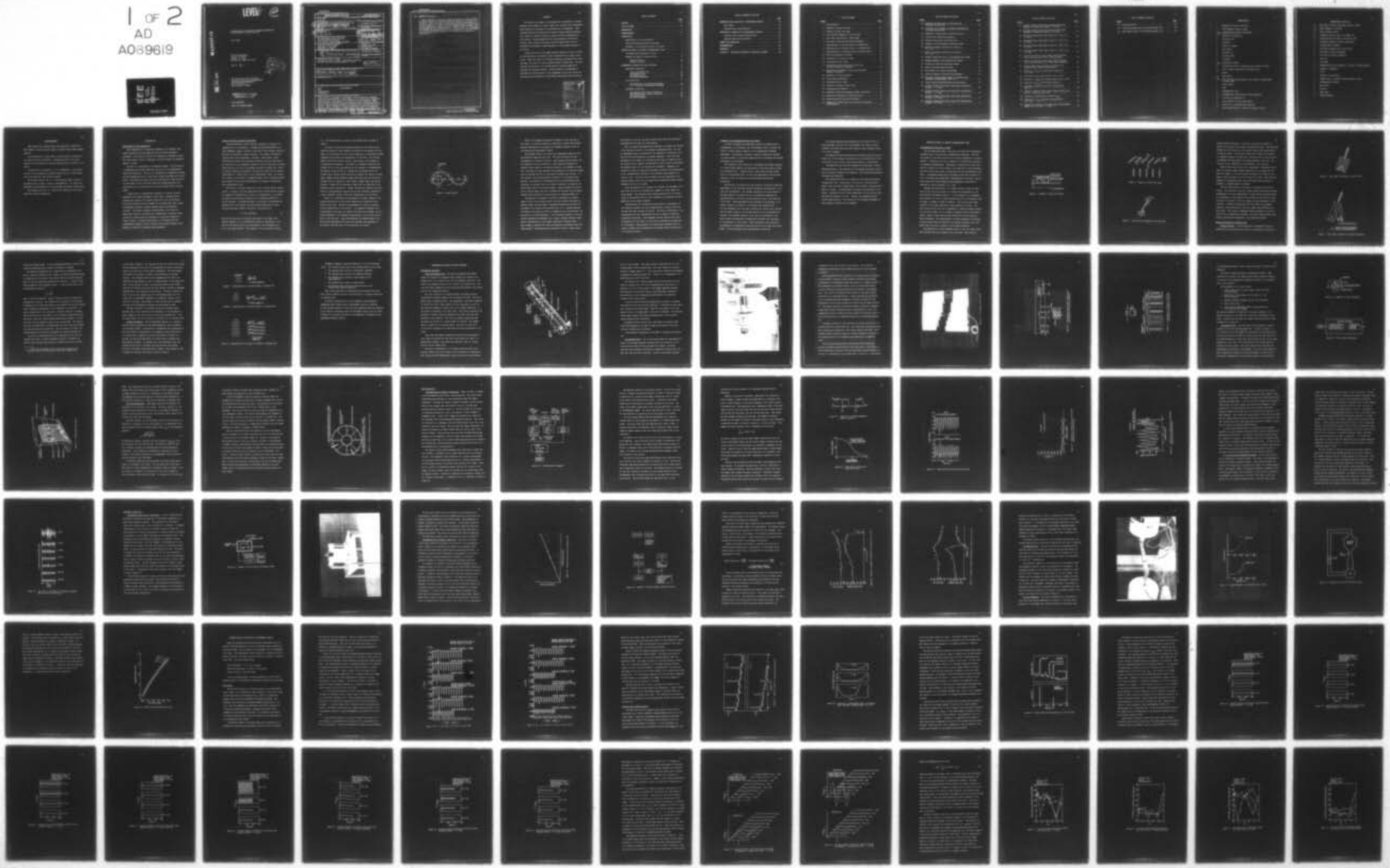

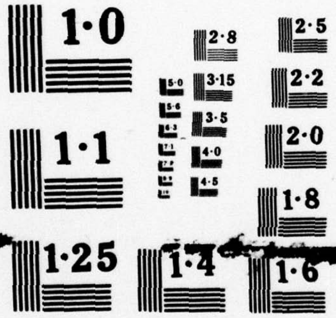
1·0
2·8
2·5
5·0
3·15
2·2
5·6
6·3
3·5
1·1
4·0
2·0
4·5
1·8
1·25
1·4
1·6

NATIONAL BUREAU OF STANDARDS
MICROCOPY RESOLUTION TEST CHART

LEVEL II

⑫ B.S.

AD A069619

INVESTIGATION OF THE UNSTEADY PRESSURE DISTRIBUTION ON THE BLADES OF AN AXIAL FLOW FAN

Gary Franke

Technical Memorandum
File No. TM 78-300
November 21, 1978
Contract No. N00024-79-C-6043

Copy No. 8

DDC RECEIVED JUN 11 1979

DDC FILE COPY

The Pennsylvania State University
Institute for Science and Engineering
APPLIED RESEARCH LABORATORY
Post Office Box 30
State College, PA 16801

APPROVED FOR PUBLIC RELEASE
DISTRIBUTION UNLIMITED

NAVY DEPARTMENT

NAVAL SEA SYSTEMS COMMAND

79 06 08 004

UNCLASSIFIED

SECURITY CLASSIFICATION OF THIS PAGE (When Data Entered)

REPORT DOCUMENTATION PAGE

READ INSTRUCTIONS BEFORE COMPLETING FORM

1. REPORT NUMBER
TM 78-300

2. GOVT ACCESSION NO.

3. RECIPIENT'S CATALOG NUMBER

4. TITLE (and Subtitle)
(6) INVESTIGATION OF THE UNSTEADY PRESSURE DISTRIBUTION ON THE BLADES OF AN AXIAL FLOW FAN,

5. TYPE OF REPORT & PERIOD COVERED
MS Thesis, May 1979

6. PERFORMING ORG. REPORT NUMBER
TM 78-300

7. AUTHOR(s)
(10) Gary Franke

8. CONTRACT OR GRANT NUMBER(s)
(15) N00024-79-C-6043
NGR-39-009-275

9. PERFORMING ORGANIZATION NAME AND ADDRESS
The Pennsylvania State University
Applied Research Laboratory
P. O. Box 30, State College, PA 16801

10. PROGRAM ELEMENT, PROJECT, TASK AREA & WORK UNIT NUMBERS
(11) 21 NOV 78

11. CONTROLLING OFFICE NAME AND ADDRESS
Naval Sea Systems Command
Department of the Navy
Washington, DC 20360

12. REPORT DATE
November 21, 1978

13. NUMBER OF PAGES
143 pages & figures

14. MONITORING AGENCY NAME & ADDRESS(if different from Controlling Office)
(9) Technical memo,

15. SECURITY CLASS. (of this report)
Unclassified, Unlimited

15a. DECLASSIFICATION/DOWNGRADING SCHEDULE

16. DISTRIBUTION STATEMENT (of this Report)
Approved for public release, distribution unlimited,
per NSSC (Naval Sea Systems Command), 2/7/79

(12) 145 p.

17. DISTRIBUTION STATEMENT (of the abstract entered in Block 20, if different from Report)
(14) ARL/PSU/TM-78-300

18. SUPPLEMENTARY NOTES

19. KEY WORDS (Continue on reverse side if necessary and identify by block number)

rotor
wake
turbomachinery
aerodynamics
hydrodynamics

20. ABSTRACT (Continue on reverse side if necessary and identify by block number)

The results of a program to investigate the distribution of unsteady pressure on the blades of a stator blade row in an axial flow turbomachine which operated in the wakes of an upstream rotor are presented. These unsteady pressure distributions were measured using a blade instrumented with a series of miniature pressure transducers which was developed in this program. Several geometrical and flow parameters--rotor/stator spacing, stator solidity, and stator incidence angle--were varied to determine the influence of these parameters on the unsteady response of the stator.

DD FORM 1 JAN 73 1473 EDITION OF 1 NOV 65 IS OBSOLETE

391 007

UNCLASSIFIED

SECURITY CLASSIFICATION OF THIS PAGE (When Data Entered)

20. **ABSTRACT (Continued)**

A major influence on the stator unsteady response is stator solidity. At high solidities, the blade-to-blade interference has a larger contribution. While the range of rotor/stator spacings investigated had a minor influence, the effect of stator incidence angle is significant. The data indicate the existence of an optimum positive incidence angle which minimizes the unsteady response. Further studies are recommended to determine the characteristics of the propagation of the rotor wakes over the stators and the behavior of the surface flow during this interaction.

ABSTRACT

The results of a program to investigate the distribution of unsteady pressure on the blades of a stator blade row in an axial flow turbomachine which operated in the wakes of an upstream rotor are presented. These unsteady pressure distributions were measured using a blade instrumented with a series of miniature pressure transducers which was developed in this program. Several geometrical and flow parameters--rotor/stator spacing, stator solidity, and stator incidence angle--were varied to determine the influence of these parameters on the unsteady response of the stator.

A major influence on the stator unsteady response is stator solidity. At high solidities, the blade-to-blade interference has a larger contribution. While the range of rotor/stator spacings investigated had a minor influence, the effect of stator incidence angle is significant. The data indicate the existence of an optimum positive incidence angle which minimizes the unsteady response. Further studies are recommended to determine the characteristics of the propagation of the rotor wakes over the stators and the behavior of the surface flow during this interaction.

Accession For
NTIS GRA&I ☒
DDC TAB ☐
Unannounced ☐
Justification____________
By____________
Distribution/
Availability Codes
Dist | Avail and/or special
A

79 06 08 004

TABLE OF CONTENTS

Page

ABSTRACT iii

LIST OF FIGURES vi

NOMENCLATURE x

ACKNOWLEDGMENTS xii

INTRODUCTION 1

  Significance of the Investigation 1

  Status of Existing Theoretical Knowledge 2

  Statement of the Problem and Scope of the Work 7

THEORETICAL MODELS OF UNSTEADY TURBOMACHINERY FLOWS 9

  Two-Dimensional Description of Flows 9

  Mathematical Models of Unsteady Flows 12

    Isolated Airfoils 12
    Cascade of Airfoils 15

EXPERIMENTAL APPARATUS AND TEST PROCEDURE 18

  Experimental Apparatus 18

    Axial Flow Research Fan 18
    Instrumented Stator 20
    Instrumented Rotor 26
    Flow Field Measurement 29

  Data Acquisition 32

    Instrumentation and Signal Conditioning 32
    A to D Conversion and Ensemble Averaging 40

  Instrument Calibration 43

    Instrumented Stator Static Calibration 43
    Instrumented Stator Dynamic Calibration 46
    Instrumented Rotor 52
    Hot-Film Anemometer 52

TABLE OF CONTENTS (Continued)

Page

PRESENTATION AND DISCUSSION OF EXPERIMENTAL RESULTS 58

Rotor Wakes 58

Unsteady Stator Blade Pressures 62

COMPARISON OF THEORETICAL AND EXPERIMENTAL RESULTS 101

Unsteady Stator Pressure Distributions 101

Unsteady Rotor Force and Moment 111

SUMMARY AND CONCLUSIONS 114

RECOMMENDATIONS 120

REFERENCES 123

APPENDIX A: THEORETICAL RESPONSE OF TUBE-CAVITY SYSTEMS 126

LIST OF FIGURES

Figure **Page**

1. Sears Function 4
2. Schematic of Axial Flow Stage 10
3. Geometry of Axial Flow Stage 11
4. Rotor Velocity Diagram at Inlet and Exit 11
5. Rotor Wake Flow Relative to Rotor Blade 13
6. Rotor Wake in Relative and Fixed Coordinates 13
7. Representation of Isolated Airfoil in Steady Flow 16
8. Representation of Isolated Airfoil in Unsteady Flow 16
9. Representation of Isolated Airfoils in Unsteady Flow . . . 16
10. Axial Flow Research Fan (AFRF) 19
11. Installation of Stators in AFRF 21
12. Instrumented Stator Blade 23
13. Instrumented Stator Blade Cross Section and Transducer Mounting Arrangement 24
14. Dimensions of Transducer Cavities and Predicted Resonant Frequencies 25
15. Schematic of Pitran Transducer 27
16. Pitran Signal Conditioner 27
17. Instrumented Rotor Blade 28
18. Location of Probes at Stator Inlet 31
19. Instrumentation Schematic 33
20. Schematic of Hot-Film Anemometer Signal Conditioner 36
21. Phase Shift Introduced by Krohn-Hite Filter 36
22. Unfiltered and Filtered Hot-Film Output 37
23. Comparison of Phase Angle of Unfiltered and Corrected Filtered Data 38

LIST OF FIGURES (Continued)

Figure **Page**

24. Comparison of Phase Angle of Unfiltered and Corrected Filtered Data 39

25. The Effect of the Number of Ensemble-Averaging Sums on Typical Pitran Output 42

26. Schematic of Pitran Static Calibration Setup 44

27. Pitran Static Calibration Apparatus 45

28. Typical Pitran Static Calibration Data 47

29. Schematic of Pitran Dynamic Calibration Setup 48

30. Results of Dynamic Calibration of Pitran at x/c = 0.15 50

31. Results of Dynamic Calibration of Pitran at x/c = 0.95 51

32. Dynamic Calibration Setup of Instrumented Rotor Blade . . . 53

33. Dynamic Response of Instrumented Rotor Blade 54

34. Schematic of Hot-Film Calibration Tunnel 55

35. Typical Hot-Film Calibration Data 57

36. Rotor Wake at the Stator Leading Edge 60

37. Spectral Analysis of Typical Hot-Film Output 63

38. Variation of Instantaneous Angle of Incidence About Time-Mean Incidence Angle, R/S = 0.5 64

39. Typical Spectral Representation of Pitran Output 66

40. Unsteady Pressure Coefficient versus Real Time-Suction Surface, i = -2 deg 68

41. Unsteady Pressure Coefficient versus Real Time-Pressure Surface, i = -2 deg 70

42. Unsteady Pressure Coefficient versus Real Time-Suction Surface, i = 17 deg 72

43. Unsteady Pressure Coefficient versus Real Time-Pressure Surface, i = 17 deg 74

LIST OF FIGURES (Continued)

Figure | Page

44. Unsteady Pressure Coefficient Variation During the Passage of a Single Rotor Wake, i = -2 deg 77

45. Unsteady Pressure Coefficient Variation During the Passage of a Single Rotor Wake, i = 17 deg 78

46. Unsteady Pressure Phase Angle versus x/c - R/S = 0.5, σ = 0.493 80

47. Unsteady Pressure Phase Angle versus x/c - R/S = 0.5, σ = 0.986 82

48. Unsteady Pressure Phase Angle versus x/c - R/S = 2.0, σ = 0.493 84

49. Unsteady Pressure Phase Angle versus x/c - R/S = 2.0, σ = 0.986 86

50. Suction and Pressure Surface Phase Angle Difference versus Incidence Angle--Blade Passing Harmonic 89

51. Suction and Pressure Surface Phase Angle Difference versus Incidence Angle--Twice Blade Passing Harmonic . . . 91

52. Relative Phase Angle Along Suction Surface with Incidence Angle--Blade Passing Harmonic 93

53. Variation of $C_{p_{rms}}$ with Rotor/Stator Spacing at x/c = 0.02 96

54. Variation of $C_{p_{rms}}$ with Solidity at x/c = 0.02 97

55. Variation of $C_{p_{rms}}$ with Incidence Angle at x/c = 0.02 . . . 98

56. Variation of $C_{p_{rms}}$ with Chordwise Position 99

57. Compressor Blade Wake Interaction Considered by Meyer (7) 103

58. Summary of Measured Peak-to-Peak Pressure Coefficients for x/c = 0.02, 0.05, and 0.15 107

59. Comparison of Measured and Predicted $C_{p_{rms}}$ 108

60. Comparison of $C_{p_{rms}}$ Measured and Predicted at x/c = 0.02 110

61. Magnitude of Unsteady Lift Gauge Output versus Harmonic Number, R/S = 0.5 and i = 17 deg 112

LIST OF FIGURES (Continued)

Figure **Page**

A-1. Cavity-Tube Model 127

A-2. Orifice Resistance Ratio versus Mach Number (33) 130

A-3. Mach Number Effects on Cavity-Tube Response (34) 131

NOMENCLATURE

C	magnitude of Fourier coefficient
c	chord length or speed of sound
$C_{P_{rms}}$	nondimensional pressure coefficient
d	diameter of pressure tap
E	end correction
f	frequency
i	angle of incidence
L	tube length
$\tilde{L}$	unsteady lift
$\tilde{M}$	unsteady moment
n	an integer
P_{atm}	atmospheric pressure
$\tilde{p}$	instantaneous value of unsteady static pressure on blade
P_s	static pressure downstream of bellmouth inlet
r	radius
r_m	mean radius
R/S	axial spacing; trailing edge of rotor blade to leading edge of stator blade
s	blade spacing
t	time
t'	nondimensional time
t'_o	nondimensional time referred to wake centerline
T	a function in reference (7)
U	linear speed of rotor at mean radius
U_Θ	velocity in a circumferential direction
V	free stream velocity or volume of transducer cavity

NOMENCLATURE (Continued)

V_d	amplitude of velocity disturbance normal to chord
V_x	axial component of velocity
W	velocity defect profile
$\overline{W}$	integrated velocity defect; from Meyer (9)
$\hat{W}$	integrated velocity defect; from Lefcort (10)
x	coordinate parallel to stator blade chord
x'	nondimensional coordinate
y	coordinate perpendicular to blade chord
α	flow angle in fixed coordinates
β	flow angle in moving coordinates
ζ	vorticity
Γ	circulation
Θ	*nondimensional blade coordinate*, or angle in Fourier analysis
λ	parameter in Appendix A
μ	$\times 10^{-6}$
ν	frequency of disturbance
ξ	stagger angle, or distance from centerline of wake
ξ'	nondimensional distance
ρ	mass density
σ	solidity
ϕ	phase angle
ω	redued frequency

ACKNOWLEDGMENTS

This research was conducted under the sponsorship of NASA Grant NGR 39-009-275, with additional support from Naval Seal Systems Command, Code 035.

The cooperation of a large number of people greatly contributed to all aspects of this investigation. Significant work on the initial design of the instrumentation had been completed prior to efforts by the author.

The influence of the advisor, Dr. R. E. Henderson, on this thesis, as well as on the approach to problem solving, will be of long lasting value, more important than technical lessons.

The frequent advice of Mr. E. P. Bruce greatly eased a variety of problems as well as being a lesson in experimentation. Mr. Bruce also developed the instrumented rotor and performed the required calibrations.

The frequent aid of Mr. W. L. Nuss in the operation of the instrumentation is greatly appreciated.

INTRODUCTION

Significance of the Investigation

The turbomachine is a significant component in our society, used almost universally in power generation and in aircraft and marine propulsion. This device is used for the conversion of mechanical energy into fluid energy, a pump or compressor, and fluid energy into mechanical energy, a turbine.

The flow in a turbomachine is exceedingly complex. The fluid may be a compressible gas in which shock waves may occur or an incompressible liquid with cavitation. The flow in a turbomachine is inherently unsteady and three dimensional with, in some cases, strong centrifugal and Coriolis forces. The blades may vibrate and will be influenced by other blades in the same blade row and in adjacent blade rows through potential flow interactions and by interaction with the viscous wakes shed by upstream blades.

A major effort in turbomachinery research is to obtain an understanding of the unsteady phenomena in such flows. Unsteady surface pressures are caused by the unsteady flows which occur on the blades. This causes unsteady forces and moments on the blades and, thus, results in mechanical vibration, airborne radiated noise, and inefficient operation. The present incomplete understanding of such flows is a significant obstacle in obtaining the turbomachinery performance characteristics of reduced noise and increased fuel efficiency required in today's society. To achieve these goals, it is necessary that the turbomachinery designer be able to predict the unsteady response of the blades as a function of available design parameters.

Status of Existing Theoretical Knowledge

Various mathematical models have been formulated to describe the unsteady flow in a turbomachine. Although the governing equations are known (momentum, energy, continuity, and state), their enormous complexity has thus far prevented a complete solution. For example, the momentum equation gives three simultaneous, nonlinear, second degree, partial differential equations whose dependent variables, velocity and pressure, are functions of four independent variables, time and three space variables. These equations can yield an approximate solution in steady flow, subject to certain simplifying assumptions, that has been shown to be an adequate approximation to certain types of real turbomachinery flows. In unsteady flow, however, the validity of assumptions made, and the resulting approximate solutions have not been demonstrated to be adequate in describing real turbomachinery flows.

Historically, unsteady analyses were first performed for an isolated airfoil. Although it has been demonstrated that isolated airfoil analyses are inadequate representations of flow in a turbomachine, it is valuable to examine isolated airfoil analyses for the techniques used and the results obtained. Von Karman and Sears (1) and Sears (2) determined the unsteady lift of an isolated flat plate airfoil subjected to a small velocity disturbance normal to the chord. The solution is:

$$\tilde{L} = \pi \rho c V V_d e^{i\nu t} S(\omega) , \qquad (1)$$

with the lift acting at the quarter chord point at all times. The reduced frequency, ω, is a nondimensional quantity proportional to the ratio of the airfoil chord to the wavelength of the disturbance, and $S(\omega)$ is the Sears function. The frequency of the disturbance is given by ν. The Sears function, plotted on the complex plane, is shown in Figure 1.

The case of velocity perturbations parallel to the chord was considered by Horlock (3) who obtained a solution for the unsteady lift and moment of an isolated flat plate airfoil subjected to a disturbance having components both parallel and perpendicular to the chord. The solution employs the Horlock function and has a form similar to the response to a perpendicular disturbance. The effect of a chordwise (parallel) disturbance can be of the same magnitude as the response to a perpendicular disturbance in some situations. Horlock (4), and Nauman and Yeh (5) extended these isolated airfoil analyses to consider the effects of blade camber, Nauman and Yeh developed design charts that show the variation of unsteady lift as a function of blade camber, stagger angle, and reduced frequency. Holmes (6) has developed a theory for the prediction of the unsteady pressure distribution. Holmes considered an isolated flat plate airfoil in incompressible, inviscid flow at zero incidence, subjected to a small sinusoidal velocity fluctuation perpendicular to the airfoil.

Meyers (7), considering the same geometry as Holmes, solved for the pressure distribution on the airfoil caused by the interaction with a moving viscous wake. The wake is approximated as a fluid jet having a velocity perpendicular to the airfoil. In a simplified expression for infinitesimally thin wakes, the shape of the wake did not appear, but the pressure depended on the integrated contribution of the velocity fluctuation in the fluid jet. Fujita and Kovasznay (8) compared Meyers' prediction with experimental data and found reasonably good agreement in the trends of the data when no flow separation was present.

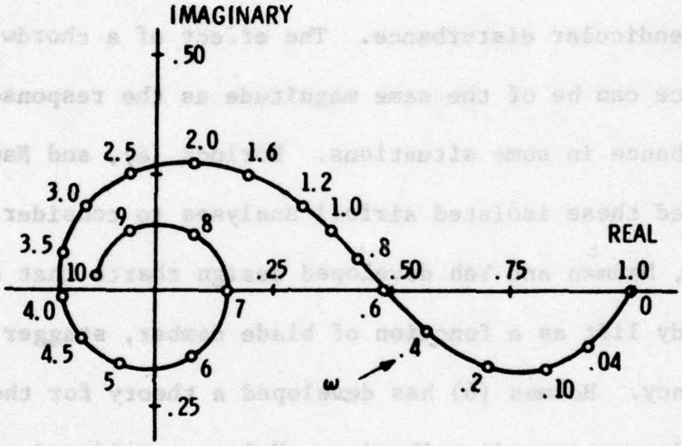

Figure 1. Sears Function

Lefcort (9) extended the analysis of Meyers to cover the case of thin wakes. As Lefcort's analysis is used here to predict the unsteady pressure distribution, the analysis is discussed in greater detail in the discussion of experimental results.

The unsteady effects of an axial flow turbomachine stage have been investigated by Kemp and Sears (10). The rotor and stator are each represented by a cascade of airfoils. Each cascade had low solidity and was composed of flat plate airfoils. Their analysis considered the unsteady effect caused by the relative motions of the cascades in steady flow. The effects of the unsteady flow considered in the upstream cascade were the unsteady flow only on the blade in question and its wake. In this respect, the unsteady analysis is similar to an isolated airfoil analysis. The effects of the unsteady flow on the downstream cascade considered the unsteady flow on the blade in question, its wake and the vortex wakes shed by the upstream cascade. Using an empirical description of viscous wakes, they also considered the unsteady lift and moment caused by the interaction of viscous wakes from upstream blades (11).

The analysis of a cascade of airfoils is performed in a similar manner as that of an isolated airfoil, but must consider the effects of adjacent blades and their wakes. Whitehead evaluated the unsteady lift and moment by an actuator disk approach (12), i.e., a cascade composed of blades of zero chord, as well as a cascade of flat plate airfoils (13) subjected to an inlet disturbance. In an alternate analysis of the same problem, Henderson and Daneshyar (14), using a slightly different mathematical representation of the blades, predicted a resonance effect: a sharp change in unsteady lift when the disturbance wavelength equals the blade spacing. This analysis also included the effect of blade camber.

The analyses of (13) and (14) give similar results when the disturbance wavelength does not equal the blade spacing.

There are meager experimental data available to evaluate the validity of the theoretical models of the unsteady turbomachine flows. The lack of experimental data is attributed to the complexity in producing a suitable flow and the measurement of unsteady parameters. Until the basic assumptions in the models are verified and the range of conditions where the theories are an adequate representation of real flows are established, the designer cannot use the theories with confidence. Henderson (15) checked his results by deducing the unsteady circulation from measurements of the circumferential variation of the time-mean total pressure rise across a rotor. The theory did not predict the exact magnitude of the unsteady response well, but the trends in the experimental results agreed reasonably well with the theory.

Bruce and Henderson (16) measured the unsteady lift and moment of an axial flow fan rotor by instrumenting a segment of a rotor blade with strain gauges. They determined that existing theories (13, 14) predict trends in experimental data, but were inadequate in predicting the exact magnitude of the unsteady response.

Satyanarayana (17) considered the interaction of a disturbance of low frequency parameter that was transported with a velocity less than the main flow and a cascade of airfoils. This type of disturbance is not representative of real turbomachine flow but is useful in evaluating theoretical predictions. Good agreement with the trends of the theory by Henderson (15) was found, but there was a deviation in the magnitude of the response. Satyanarayana also obtained good agreement with the results of Holmes (18) in predicting the unsteady pressure distribution of an isolated airfoil.

Statement of the Problem and Scope of the Work

In order to minimize the undesirable effects of unsteady flow in turbomachines, it is necessary that the designer be able to predict the effect of various design parameters on the turbomachine's unsteady performance. The designer, therefore, requires a theoretical analysis of proven validity, or sufficient empirical data to determine the unsteady performance of a new design.

The objective of this study was to investigate the unsteady response of a stator blade caused by the interaction of the stator with the wakes of an upstream rotor. A major portion of this effort was the development of an instrumented stator to allow the measurement of the unsteady pressures on both its pressure and suction sides during such an interaction.

Specifically, the objective of this study was realized by conducting measurements of the following unsteady performance characteristics of an axial flow turbomachine. The unsteady response of the stator blades to the wakes shed by an upstream rotor was determined by measuring the unsteady pressure at various locations along the chord, at the mid-span of the blade. These measurements were conducted at the mid-span of the blade to minimize the effects of the annulus wall boundary layer. A hot-film anemometer probe was used to measure the velocity field incident upon the stator blades at the mid-span position at one circumferential location. The unsteady response of the rotor to the presence of the stator blades was determined by measuring the unsteady lift and moment at the mid-span of a rotor blade. These measurements were obtained by instrumenting an independently supported section of the blade with strain gauges. This instrumented blade was developed by Bruce (19).

The unsteady response was determined for two values of rotor to stator spacing, 2 and 1/2 rotor chord lengths, two values of stator solidity, 0.493 and 0.986, and three values of stator incidence angle, -2, 5, and 17 degrees.

The unsteady pressure measurements are compared with the results of Lefcort (9) for the pressure distribution on an isolated airfoil interacting with a local velocity perturbation caused by a viscous wake.

Instrumentation and associated hardware were developed to measure unsteady pressures. New techniques for the dynamic and static calibration of pressure transducers were employed. Data reduction and analysis procedures were developed.

This investigation does not consider all the aspects of unsteady turbomachinery flow. Specifically, the effects of rotor and stator camber, rotor and stator stagger angle, rotor solidity, and blade thickness are excluded. All measurements were made at the mid-span of the blades. Although the flow is three dimensional, the flow in the radial direction was assumed to be zero. However, the assumption was not verified experimentally. The variation of the unsteady performance at other spanwise locations was not examined.

THEORETICAL MODELS OF UNSTEADY TURBOMACHINERY FLOWS

Two-Dimensional Description of Flows

The two-dimensional model of the flow in an axial flow turbomachine considers flow in the axial and circumferential directions. The flow that exists in the radial direction in an actual turbomachine is entirely ignored. In addition, the flow is assumed to be inviscid and, generally, is considered incompressible. Experimental correlations are used extensively to account for viscous effects, the prediction of flow separation, and other factors that cannot be determined from the two-dimensional flow model. Turbomachine design and/or performance predictions consider the flow to be steady and proceed with a two-dimensional flow model using the basic equations of fluid mechanics and experimental correlations as discussed in various textbooks, e.g., (20).

Consider the intersection of a cylinder concentric with the shaft and the rotor and stator blades of an axial flow turbomachine, at the mean radius of the blades, Figure 2. If the cylinder is cut lengthwise and flattened, the trace of blade intersections will be two parallel rows of blades, a cascade, as shown in Figure 3. The rotor row has linear velocity U at the mean radius due to the rotation of the rotor. The rotor inlet and exit flow can be expressed in a frame of reference moving with the rotor speed U, or in a frame of reference fixed to the machine casing. Figure 4 shows inlet and exit velocities in both moving and fixed coordinates. The transformation to fixed coordinates is performed by simply subtracting the velocity of the moving coordinates (the rotor speed) from the velocity observed in the moving coordinates.

The existence of a viscous boundary layer on the rotor blades causes lower velocity flow in the region of the rotor wake. When viewed in

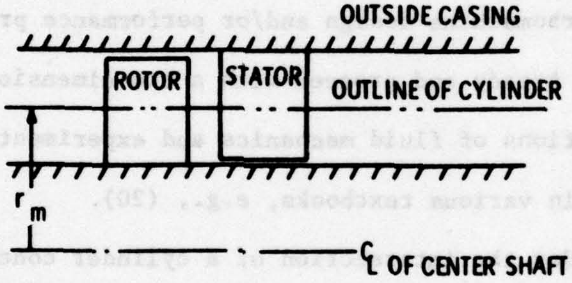
OUTSIDE CASING
ROTOR
STATOR
OUTLINE OF CYLINDER
r_m
℄ OF CENTER SHAFT

Figure 2. Schematic of Axial Flow Stage

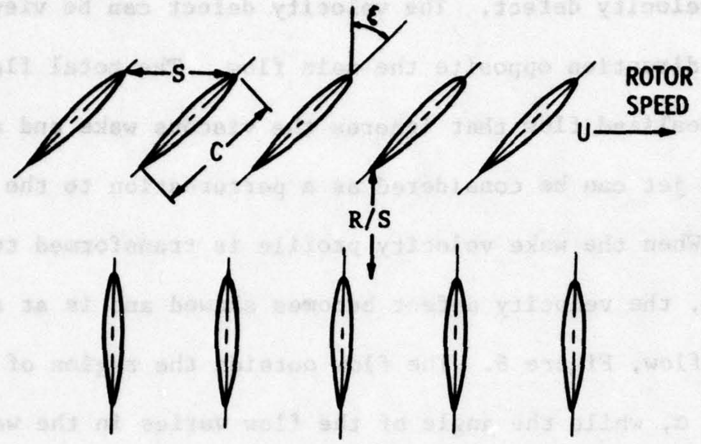
ε
S
C
ROTOR
SPEED
U
R/S

Figure 3. Geometry of Axial Flow Stage

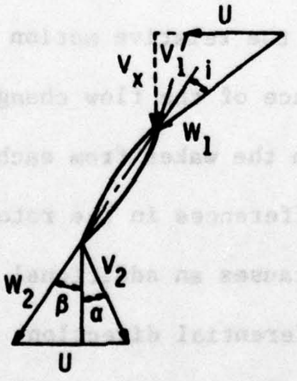
U
V_x
V_1
i
W_1
W_2
β
α
V_2
U

Figure 4. Rotor Velocity Diagram at Inlet and Exit

moving coordinates (Figure 5), this flow can be seen as uniform in direction but having a local region of decreased velocity. The difference between the local velocity and the velocity outside the viscous wake is the velocity defect. The velocity defect can be viewed as a fluid jet in a direction opposite the main flow. The total flow is then the sum of an idealized flow that ignores the viscous wake and a fluid jet. The fluid jet can be considered as a perturbation to the main flow.

When the wake velocity profile is transformed to stationary coordinates, the velocity defect becomes skewed and is at an angle with the main flow, Figure 6. The flow outside the region of the wake is at an angle α, while the angle of the flow varies in the wake. When this flow impinges on a downstream blade, the viscous wake causes the blade to experience a changing angle of incidence.

The flow interacting with the stator is unsteady due to several factors. The turbulence in the flow causes random fluctuations and hence unsteadiness in the flow independently of other factors discussed herein. As a consequence of the relative motion between the wake and the stator, the angle of incidence of the flow changes, giving unsteadiness or time variation. Although the wakes from each rotor blade are considered identical, small differences in the rotor blades cause differences in their wakes. This causes an additional spatial difference in the flow field in the circumferential direction. An airfoil moving through these spatial variations will experience a time varying flow field.

Mathematical Models of Unsteady Flows

Isolated Airfoils.

A brief discussion of mathematical models of unsteady flow over airfoils can be useful in visualizing the sources of

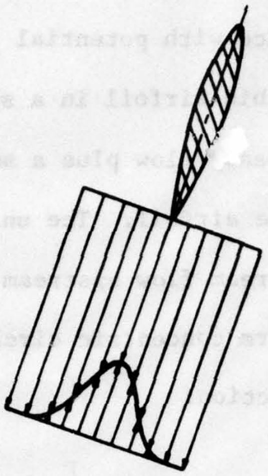

Figure 5. Rotor Wake Flow Relative to Rotor Blade

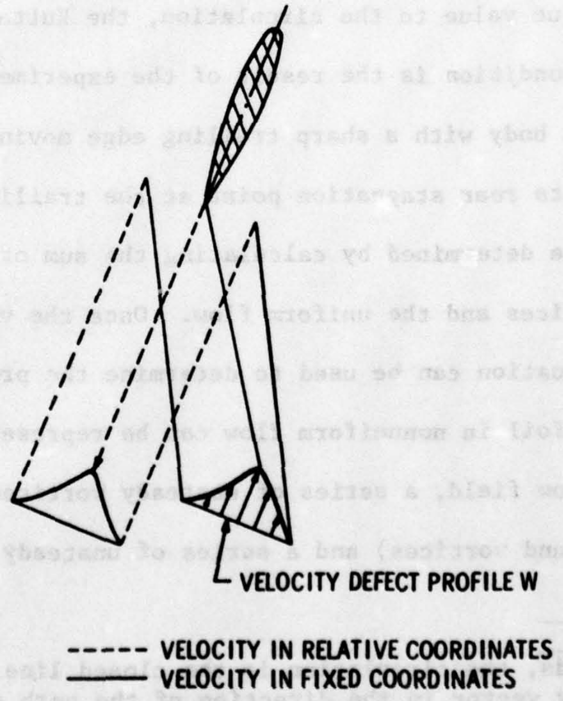
VELOCITY DEFECT PROFILE W
----- VELOCITY IN RELATIVE COORDINATES
—— VELOCITY IN FIXED COORDINATES

Figure 6. Rotor Wake in Relative and Fixed Coordinates

interaction between blades. In the following discussion of inviscid flow, a general acquaintance with potential flow theory is assumed.

An infinitely thin airfoil in a steady flow is represented by the sum of a uniform, steady flow plus a series of vortices distributed along the camberline of the airfoil. The uniform flow has constant direction equal to the free stream flow upstream of the airfoil. A vortex is flow whose streamlines form concentric circles. It has velocity only in the circumferential direction:

$$U_\Theta = \frac{\Gamma}{2\pi r} ,$$

where Γ is the circulation.[1] Figure 7 shows an airfoil in steady flow represented by vortices. The strength (or circulation) of the vortices is adjusted so the velocities induced by the uniform flow and the vortices have no component perpendicular to the camberline of the airfoil. To give a unique value to the circulation, the Kutta condition is imposed. The Kutta condition is the result of the experimental observations which show that a body with a sharp trailing edge moving uniformly in a fluid will have its rear stagnation point at the trailing edge. The velocity field can be determined by calculating the sum of the velocities induced by the vortices and the uniform flow. Once the velocity is known, the momentum equation can be used to determine the pressure distribution.

An airfoil in nonuniform flow can be represented by the sum of an unsteady flow field, a series of unsteady vortices to represent the airfoil (bound vortices) and a series of unsteady vortices in the wake of the airfoil, Figure 8. The unsteady vortices in the wake exist because the flow upstream of the airfoil is irrotational and since no rotational forces act on the flow, it must remain irrotational. The time varying circulation on the blade is related to the circulation of the wake vortices. The strength of the vortices representing the airfoil are determined at each instant in time in a manner similar to the steady flow case. At each instant in time, the velocities induced by the uniform flow and all vortices, both bound and wake vortices, can have no component perpendicular to the camberline of the airfoil. The Kutta condition is used to fix the rear stagnation point at the trailing edge as in the steady flow. An additional complexity is introduced, however, by the vortices in the wake. The strength of these vortices must be adjusted such that the flow remains irrotational at each instant in time.

---

[1] $\Gamma = \oint \bar{v} \cdot \overline{ds}$, the circulation is the closed line integral of the velocity vector in the direction of the path of integration.

The Kutta condition for unsteady flow has been verified experimentally under certain conditions (the wavelength of the disturbance is small compared to the airfoil chord) by Fujita and Kovasnay (8). It is not known whether the Kutta condition is satisfied for all unsteady flows.

Cascade of Airfoils. The two-dimensional analysis of a cascade of airfoils may be conducted with the same mathematical tools as employed with isolated airfoils. The analysis is considerably more complicated in that each airfoil is influenced by the presence of every other airfoil. In a steady flow to compute the velocity field about an airfoil in a cascade, the sum of the influences of vortices used to represent each blade must be included. In unsteady flow, the influences of the time varying vortices used to represent each blade and the time varying vortices in the wake of each blade must be added at every instant of time to compute the velocity field about an airfoil, Figure 9.

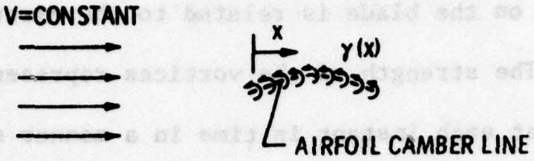
V=CONSTANT
x
γ(x)
AIRFOIL CAMBER LINE

Figure 7. Representation of Isolated Airfoil in Steady Flow

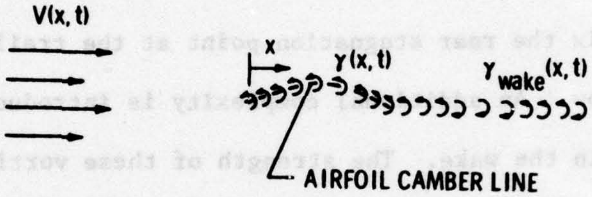
V(x, t)
x
γ(x, t)
γ wake (x, t)
AIRFOIL CAMBER LINE

Figure 8. Representation of Isolated Airfoil in Unsteady Flow

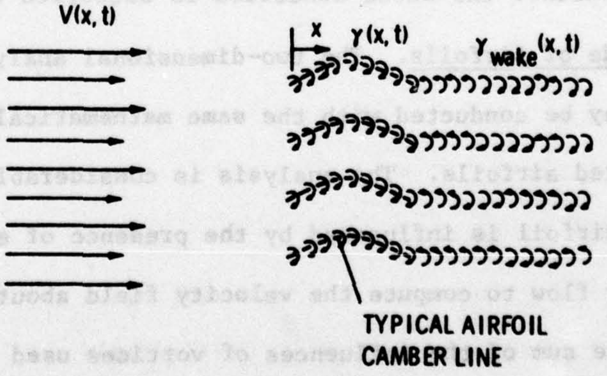
V(x, t)
x
γ(x, t)
γ wake (x, t)
TYPICAL AIRFOIL CAMBER LINE

Figure 9. Representation of Cascade of Airfoils in Unsteady Flow

Consider a compressor stage consisting of a rotor and downstream stator. The following interactions cause unsteady effects on any blade:

1. The unsteady bound vortices of the blade in question.
2. The unsteady wake vortices of the blade in question.
3. The unsteady bound vortices of other blades in the same blade row.
4. The unsteady wake vortices of these blades.
5. The unsteady bound vortices and wake vortices of the blades in the adjacent blade row.

These interactions must be considered with an unsteady flow field that could be caused by an inlet flow distortion or by viscous wakes from an upstream blade.

The above interactions are of such complexity that substantial assumptions must be made before an approximate solution is obtained. For the theories employed in this study the assumptions made are discussed in the "Status of Existing Theoretical Knowledge" section, and the theory of Meyer (7) is further discussed in the "Comparison of Theoretical and Experimental Results" section.

EXPERIMENTAL APPARATUS AND TEST PROCEDURE

Experimental Apparatus

Axial Flow Research Fan. The Axial Flow Research Fan (AFRF), Figure 10, consists of a bellmouth inlet leading to an annular flow passage 54.61 cm in diameter with a 24.13 cm diameter center hub. The annular flow passage contains a rotor, stator, and auxiliary fan. The rotor and stator comprise the test section and the auxiliary fan provides the air flow through the annulus.

The rotor consists of 12 aluminum blades, including one blade instrumented to measure unsteady lift and moment ($\tilde{L}$ and $\tilde{M}$). The instrumented blade is described later. The blades have a 10% thick uncambered C1 profile (21) with a chord length of 15.24 cm and span of 14.99 cm. The rotor was designed to produce zero lift at design conditions, i.e., zero angle of incidence at all blade radii. This feature simplifies the analysis of unsteady flows by eliminating the steady rotor lift when operated at this condition. The rotor can produce steady lift when operated with the flow at a nonzero angle of incidence. The stagger angle, ξ, equals 45° at the mean radius. The rotor is driven by a 14.9 kw motor contained in the center hub and located downstream of the stator.

Input power and signal transmission lines from the instrumented rotor blade run through the rotor hub to the hollow rotor shaft to a downstream 14-channel, coin silver slip-ring unit, then out through holes in the aft support fins.

The stator, consisting of 4 or 8 blades having the same cross-sectional shape as the rotor blades, can be positioned by changing the outer casing and hub configuration to give rotor/stator axial spacings

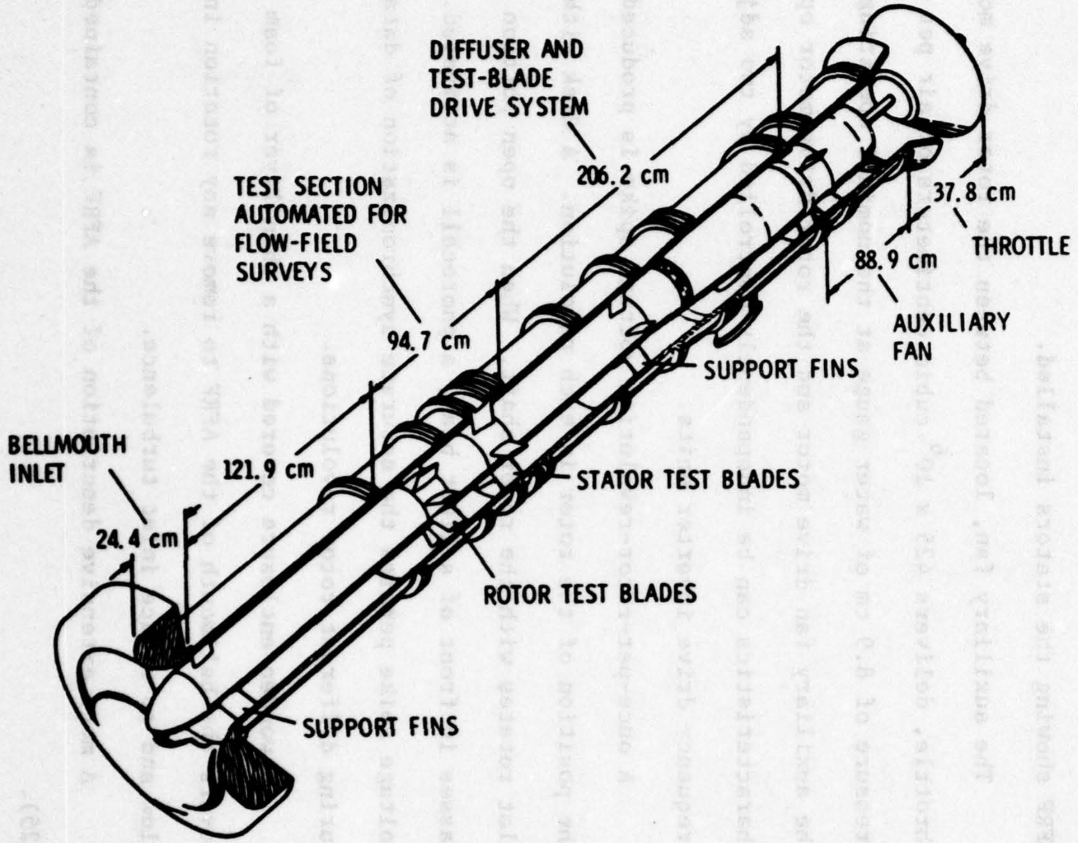
DIFFUSER AND TEST-BLADE DRIVE SYSTEM
TEST SECTION AUTOMATED FOR FLOW-FIELD SURVEYS
206.2 cm
37.8 cm
THROTTLE
88.9 cm
AUXILIARY FAN
94.7 cm
SUPPORT FINS
BELLMOUTH INLET
121.9 cm
STATOR TEST BLADES
24.4 cm
ROTOR TEST BLADES
SUPPORT FINS

Figure 10. Axial Flow Research Fan (AFRF)

1/2 to 2 chord lengths. This axial spacing is measured from the rotor trailing edge to stator leading edge. The stator blades are untwisted and have a stagger angle of 0°. Two of the stator blades are instrumented to measure the unsteady pressure ($\tilde{P}$). Figure 11 is a photograph of the AFRF showing the stators installed.

The auxiliary fan, located between the rotor drive motor and exit throttle, delivers 425×10^6 cubic centimeters of air per minute at a pressure of 8.9 cm of water gauge at the nominal operating condition. The auxiliary fan drive motor and the rotor drive motor operational characteristics can be independently controlled by two adjustable frequency drive inverter units.

A once-per-rotor-revolution voltage spike is produced to indicate the position of the rotor in each revolution. A disk with an open radial slot rotates with the rotor shaft. When the open portion of the disk passes in front of a light beam, a photocell is activated. The resulting voltage spike permits the accurate synchronization of data produced during different rotor revolutions.

A wooden enclosure covered with a thin layer of foam and screen covers the bellmouth of the AFRF to remove any rotation in the inlet flow and to reduce inlet turbulence.

A more extensive description of the AFRF is contained in Reference (25).

Instrumented Stator. Two of the stator blades were instrumented to measure the unsteady pressures resulting from the interaction of the stators and the wakes from the upstream rotor blades. One blade, fabricated from aluminum, contained six transducers located at 5%, 15%, 30%, 40%, 50%, and 75% of the chord. A second, brass blade contained

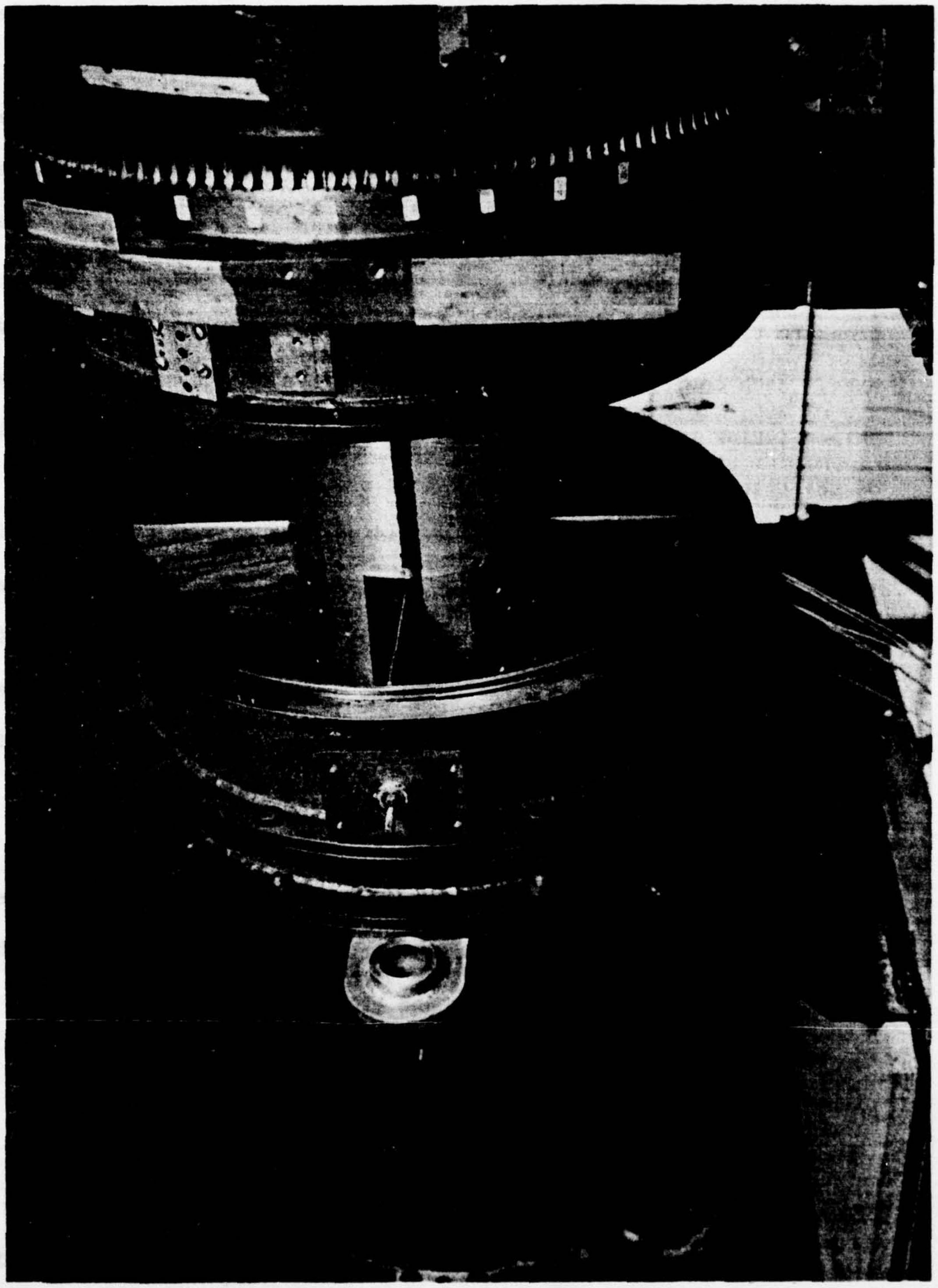

Figure 11. Installation of Stators in AFRF

transducers at 2%, 40%, and 95% chord locations. Each blade has a transducer at 40% chord to check whether the flow over the two blades is similar.

Each instrumented blade consisted of two sections that fit together to form internal cavities in which pressure transducers were mounted. A photograph of a disassembled blade and transducer is shown in Figure 12. The transducers were mounted between a pair of O-rings which form a pressure tight seal and permit assembly and disassembly with relative ease. Each cavity is connected to the surface of the blade by holes perpendicular to the blade surface. A blade cross-section and details of the transducer mounting arrangement are shown in Figure 13. The dimensions of the internal cavities and surface taps are shown in Figure 14. The surface taps were located about the mean radius in a staggered manner which covered a spanwise extent of approximately 2.5 cm. This staggering was used to minimize spurious pressure fluctuations caused by flow in the vicinity of an upstream surface tap on a downstream surface tap.

To measure pressures on only one side of a blade, the holes on the opposite side were covered with tape. Each blade also contained passages that lead from the transducer to the outside casing of the AFRF. These passages contain electrical leads and provided atmospheric pressure to the reference side of the transducer (see description of transducer below).

The transducers employed were Pitran Model PT-M2 differential pressure transducers manufactured by Stow Laboratories. The Pitran is a silicon NPN planar transistor with the emitter-base junction mechanically coupled to a diaphragm as shown schematically in Figure 15. Displacement

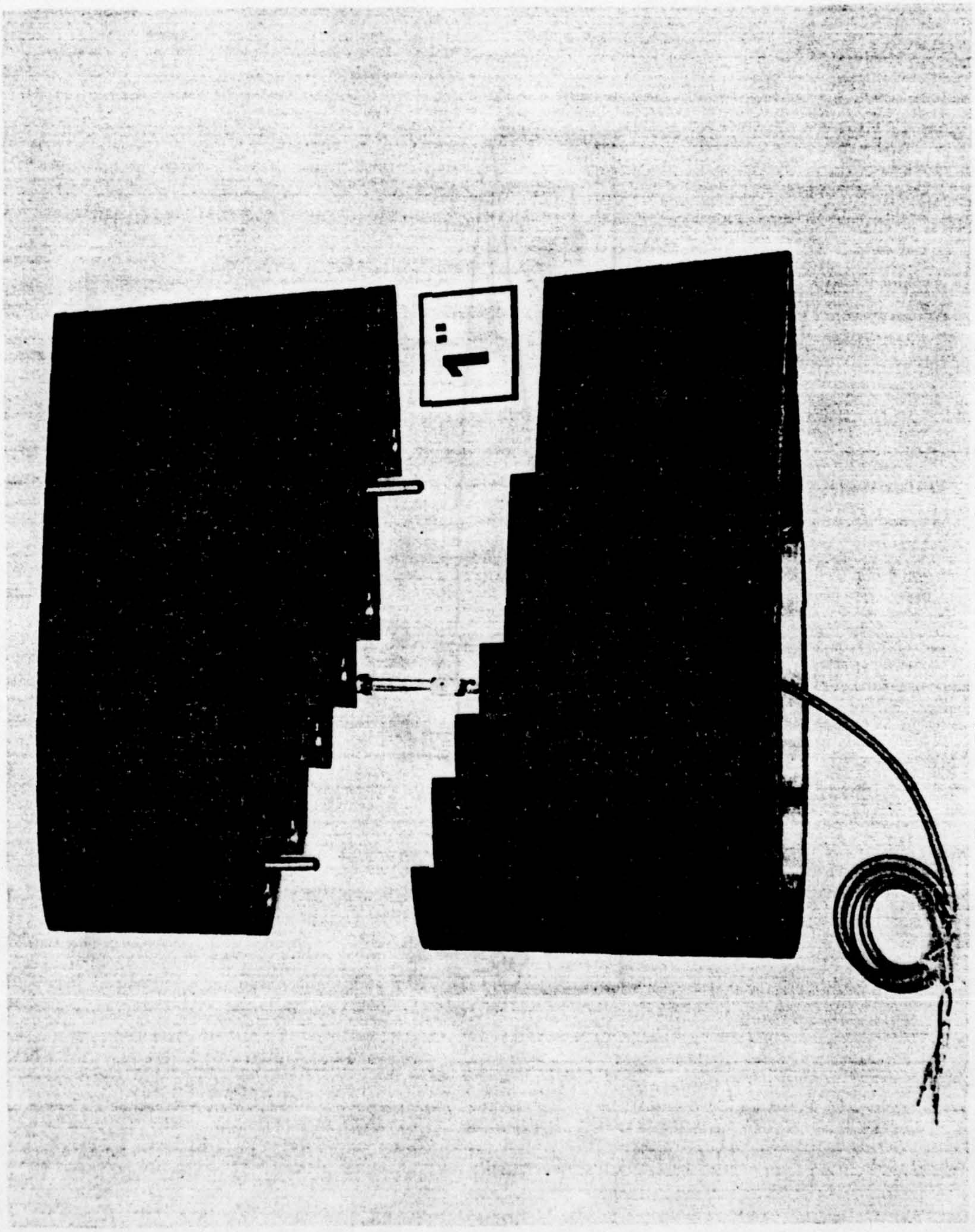

Figure 12. Instrumented Stator Blade

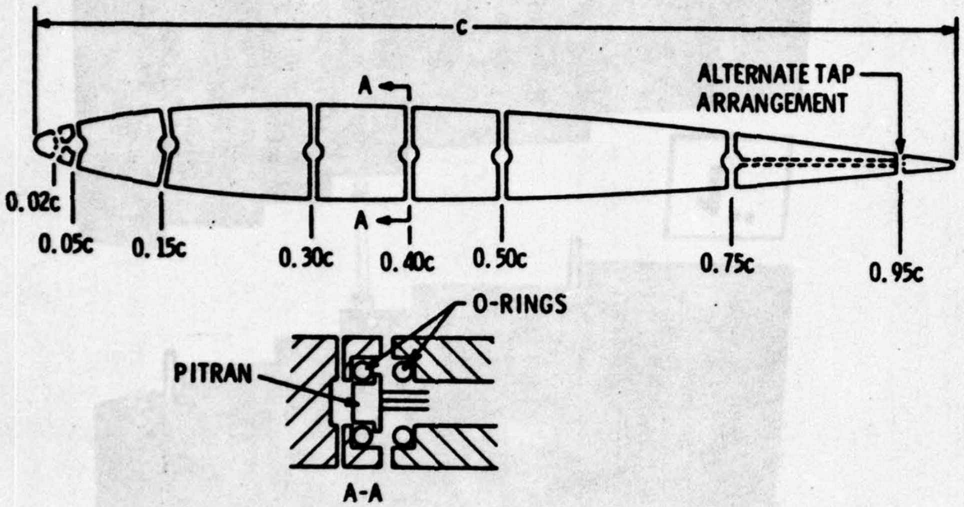
C
ALTERNATE TAP ARRANGEMENT
A
A
0.02c
0.05c
0.15c
0.30c
0.40c
0.50c
0.75c
0.95c
O-RINGS
PITRAN
A-A

Figure 13. Instrumented Stator Blade Cross Section and Transducer Mounting Arrangement

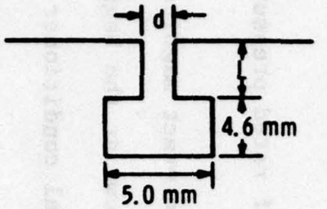

TRANSDUCER LOCATION	DIMENSIONS		RESONANT FREQUENCY		
% CHORD	d mm	L mm	HELMHOLTZ	IBERALL [29]	DYNAMIC CALIBRATION
0.02	0.9	0.5	5000	6100	2400 ± 300
0.05	0.9	1.5	3300	3500	3500 ± 300
0.15	1.8	3.8	4200	4900	3500 ± 300
0.30	1.8	5.0	3700	3800	3500 ± 300
0.40	1.8	4.8	3800	3900	3500 ± 300
0.50	1.8	4.1	4100	4300	3500 ± 300
0.75	1.8	1.3	6500	7700	> 5000
0.95	1.2	28.	1100	1000	1100 ± 200

Figure 14. Dimensions of Transducer Cavities and Predicted Resonant Frequencies

of the diaphragm produces a large, reversible change in the gain of the transistor.

The Pitran transducers measure a differential pressure. When installed in the stator, the unknown blade surface pressure is applied to the face of the diaphragm and atmospheric pressure to the reference side of the transducer.

The advantages of the Pitran include:

1. Linear output over the rated pressure range (0.25 PSID for Model PT-M2).
2. High level of output signal (on the order of 1 volt per cm of water).
3. Resonant mechanical frequency greater than 100,000 Hz.
4. Small size (0.5 cm).
5. Large overload capability (700% of rated pressure can be tolerated without damage).

The overload capability is important as the exact magnitude of the unsteady pressures on the blades were unknown at the beginning of this study. Included with the Pitran is a signal conditioner which is shown schematically in Figure 16.

Instrumented Rotor. One rotor blade was instrumented to measure unsteady force ($\tilde{L}$) and unsteady moment ($\tilde{M}$). As shown in Figure 17, a 2.54 cm span blade of this segment is cantilevered from the blade hub at the mid-chord position by means of a beam that has the lower portion of its length machined as a torque tube, and the upper portion of its length machined as a force cube. The center section of the blade segment is located at the mean radius. The torque tube and force cube have been instrumented using miniature strain gauges. The 2.54 cm span segment is made of magnesium to minimize its mass and movement of inertia and is structurally independent of the rotor blade except for the cantilever

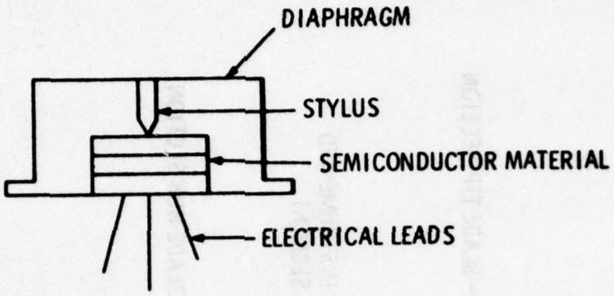
DIAPHRAGM
STYLUS
SEMICONDUCTOR MATERIAL
ELECTRICAL LEADS

Figure 15. Schematic of Pitran Transducer

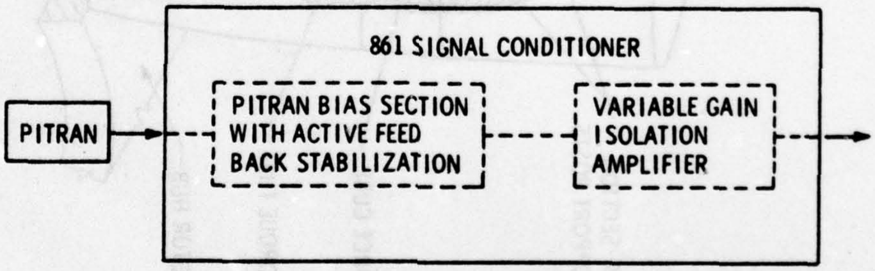
861 SIGNAL CONDITIONER
PITRAN
PITRAN BIAS SECTION WITH ACTIVE FEED BACK STABILIZATION
VARIABLE GAIN ISOLATION AMPLIFIER

Figure 16. Pitran Signal Conditioner

40

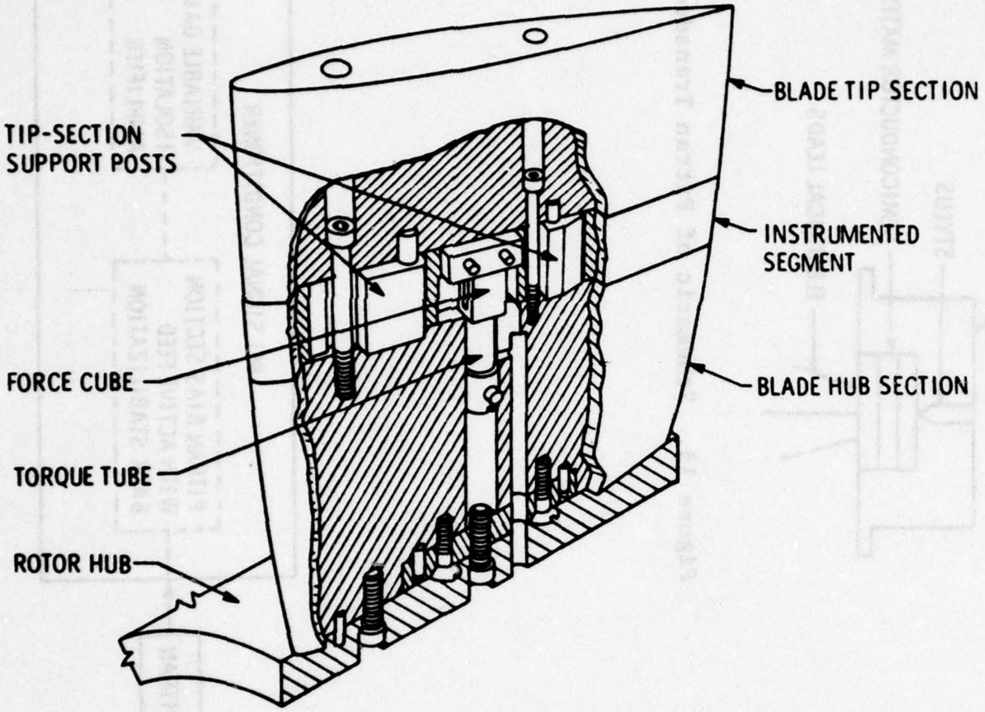
BLADE TIP SECTION
TIP-SECTION SUPPORT POSTS
INSTRUMENTED SEGMENT
FORCE CUBE
BLADE HUB SECTION
TORQUE TUBE
ROTOR HUB

Figure 17. Instrumented Rotor Blade

mount. The aluminum tip portion of the blade attaches to posts on the aluminum hub section which pass through slots in the instrumented section. A minimum clearance of 0.0127 cm is maintained at each mating surface. The magnesium has been mass-balanced to preclude uneven displacement. A more detailed description of this blade is presented in Reference (19).

Flow Field Measurement. Measurements were made of pertinent flow parameters in the vicinity of the stators. The axial velocity, V_x, the resultant velocity upstream of the stator, V, the angle of incidence, i, between V and the stator chord, and W, the velocity defect caused by the viscous rotor wakes were determined.

The axial velocity, V_x, was determined from the static pressure, P_s, measured by a pressure tap in the fan annulus 13.5 cm downstream of the inlet bellmouth from the following relation where P_{atm} is the atmospheric pressure:

$$V_x = \sqrt{\frac{2(P_{atm} - P_s)}{\rho}} . \tag{2}$$

A differential pressure transducer was used to measure $(P_{atm} - P_s)$ and ρ was calculated from the Ideal Gas Law. The pressure transducer used was a variable reluctance type manufactured by Validyne Engineering Corporation. The transducer was calibrated by comparing the output voltage to the pressure indicated by a micromanometer with an identical pressure applied to each instrument.

A three-hole wedge probe was positioned at the mean radius approximately 3 cm upstream of the stator. The two static taps of the three-hole probe are located symmetrically on opposite sides of a wedge so that the probe can be aligned in the direction of the flow by making the static pressure at each static tap equal. An indicator on the probe and a protractor fixed to the AFRF outer casing were used to measure the angle between the wedge and an axial reference line.

A hot-film anemometer probe was located at the mean radius and equipped with a pointer and protractor to permit alignment with the flow as determined from the three-hole probe. The average velocity upstream of the stator was determined from the D.C. voltage output of the anemometer. The velocity profile of the rotor wake was determined from total anemometer voltage. The hot-film probe measures the component of the rotor wake velocity profile that is parallel to the main flow. The velocity defect may then be calculated from the geometry shown in Figures 5 and 6. The hot-film probe is a commercially available type with sensor dimensions of 0.00254 cm diameter x 0.0528 cm long.

Both the three-hole and hot-film probes were located circumferentially in between stator blades to minimize the effect of the probe wake on the flow field on the blades, Figure 18. Because of the design of probe mounting holes in the outer casing of the AFRF, it was desirable to change the probe circumferential positions when the relative positions of the rotor and stator were changed in order to mount the hot-film probe at an axial location as close as possible to the leading edge of the stator. In such an axial location, the probe will record the rotor wake characteristics that more nearly represent the wake at the stator leading edge. The hot-film probe was 2 cm upstream of the stator leading edge when the stator was positioned at rotor/stator spacing of two chord lengths, and 2.5 cm upstream when the rotor/stator spacing equaled 1/2 chord length.

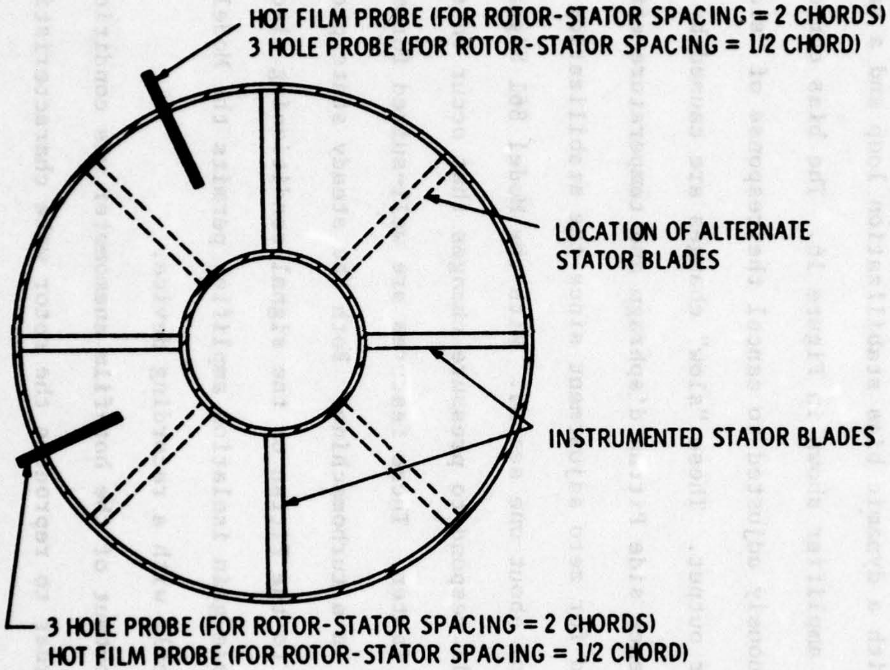
HOT FILM PROBE (FOR ROTOR-STATOR SPACING = 2 CHORDS)
3 HOLE PROBE (FOR ROTOR-STATOR SPACING = 1/2 CHORD)
LOCATION OF ALTERNATE STATOR BLADES
INSTRUMENTED STATOR BLADES
3 HOLE PROBE (FOR ROTOR-STATOR SPACING = 2 CHORDS)
HOT FILM PROBE (FOR ROTOR-STATOR SPACING = 1/2 CHORD)

Figure 18. Location of Probes at Stator Inlet

Data Acquisition

Instrumentation and Signal Conditioning. Figure 19 shows a schematic of the instrumentation and signal conditioning used. The Pitran signal conditioning was performed by a Stow Laboratories Model 861 Signal Conditioner. The Model 861 Signal Conditioner includes a Pitran biasing section with a dynamic bias stabilization loop and a variable gain isolation amplifier shown in Figure 16. The bias current to the Pitran is continuously adjusted to cancel the response of "slow" changes of transducer output. These "slow" changes are caused by the pressure on the reference side Pitran diaphragm and temperature effects. Thus, there is no need for zero adjustment since the stabilization circuit has a time constant of about one second. With the Model 861 Signal Conditioner, the Pitran will respond to pressure changes that occur on the order of one second or faster. These features are well-suited for measuring unsteady pressures in a turbomachine. Both the steady state pressure and voltage drift due to the Pitran or the signal conditioning electronics are ignored. The variable gain isolation amplifier permits the Model 861 output to be used directly with a recording device.

The output of the hot-film anemometer was conditioned to enable the tape recorder to reproduce the rotor wake characteristics with suitable accuracy. The anemometer output contains a D.C. voltage corresponding to the average velocity encountered and an A.C. voltage corresponding to the fluctuating velocity in the wake of the upstream rotor blades. Since the A.C. portion is considerably smaller than the D.C. portion of the signal, the tape recorder could not reproduce the rotor wake signal with the desired accuracy. Therefore, an amplifier was designed to enhance the A.C. portion of the signal. A schematic of the A.C. amplifier is shown in Figure 20.

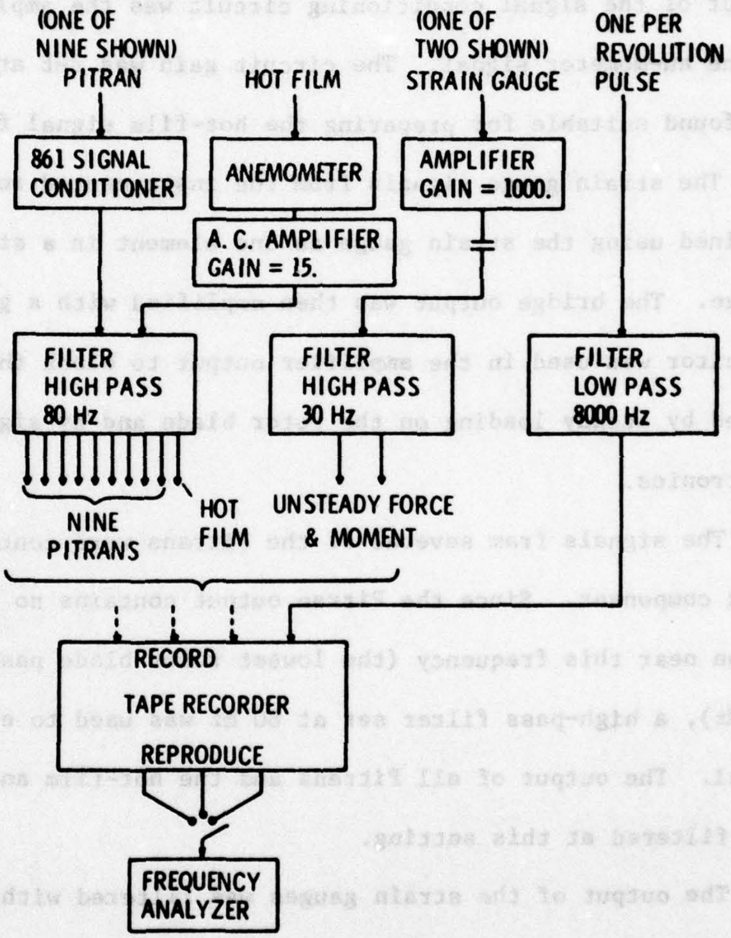
(ONE OF
NINE SHOWN)
PITRAN
HOT FILM
(ONE OF
TWO SHOWN)
STRAIN GAUGE
ONE PER
REVOLUTION
PULSE
861 SIGNAL
CONDITIONER
ANEMOMETER
AMPLIFIER
GAIN = 1000.
A. C. AMPLIFIER
GAIN = 15.
FILTER
HIGH PASS
80 Hz
FILTER
HIGH PASS
30 Hz
FILTER
LOW PASS
8000 Hz
NINE
PITRANS
HOT
FILM
UNSTEADY FORCE
& MOMENT
RECORD
TAPE RECORDER
REPRODUCE
FREQUENCY
ANALYZER

Figure 19. Instrumentation Schematic

The amplifier consists of two op-amp circuits. In the first op-amp circuit, a resistor was adjusted manually to control a "bucking" voltage to cancel the D.C. portion of the signal, leaving only the A.C. signal as the input to the second op-amp circuit. A resistor in the second op-amp circuit was adjusted to determine the gain of the circuit. The output of the signal conditioning circuit was the amplified A.C. portion of the anemometer signal. The circuit gain was set at 15.00. This gain was found suitable for preparing the hot-film signal for recording.

The strain gauge signals from the instrumented rotor blade were obtained using the strain gauge as one element in a standard Wheatstone bridge. The bridge output was then amplified with a gain of 1000. A capacitor was used in the amplifier output to block the steady voltage caused by steady loading on the rotor blade and by signal drift in the electronics.

The signals from several of the Pitrans were contaminated by a large 60 Hz component. Since the Pitran output contains no significant information near this frequency (the lowest rotor blade passing frequency is 200 Hz), a high-pass filter set at 80 Hz was used to eliminate the 60 Hz signal. The output of all Pitrans and the hot-film anemometer signal were filtered at this setting.

The output of the strain gauges was filtered with a high pass filter set at 30 Hz as the lowest frequency of interest is 67 Hz. The once-per-revolution pulse was filtered with a low pass filter set at 8000 Hz which has no significant effect on the pulse. The original purpose of filtering all the data, instead of filtering only the Pitrans having the 60 Hz contamination, was to minimize the effect of the phase shift introduced by the filter. With all data having the same phase shift, it was expected that relative timing of the transducer response would be maintained.

However, the filters do introduce a phase shift as a function of input frequency. Figure 21 shows the phase shift as a function of the ratio of input frequency to the cutoff frequency of the filter as given by Reference (22). This phase shift had a significant effect on the data. Figure 22 shows a hot-film signal that was recorded after being filtered and the same hot-film signal that was recorded unfiltered. Each signal has been ensemble averaged using 100 sums. The dramatic difference between the two signals is caused by the phase relation of the constituent frequencies and made it necessary, therefore, to correct the data. Each signal was Fourier analyzed, that is decomposed, into the form:

$$\sum_{n=1}^{\infty} C_n \cos(n\theta - \phi_n) \; . \qquad (3)$$

The Fourier analysis of the unfiltered signal considered the first 60 terms of the Fourier series, and the filtered signal calculated from the first 60 terms with the phase angle ϕ was adjusted to compensate for the filter. Figures 23 and 24 show the magnitude and phase of these signals. Since these two signals are virtually identical, it is feasible to use the Fourier analyses and phase shift compensation technique to correct the data.

The tape recorder used was a Bell and Howell seven-channel FM data tape recorder. The recorder was operated at 1-7/8 ips, resulting in a cutoff frequency of 1250 Hz. This was sufficient to record four times the highest blade passage frequency encountered. Subsequent frequency analysis of all the signals showed this frequency limit to be adequate. Frequencies greater than 1250 Hz were present in several hot-film signals;

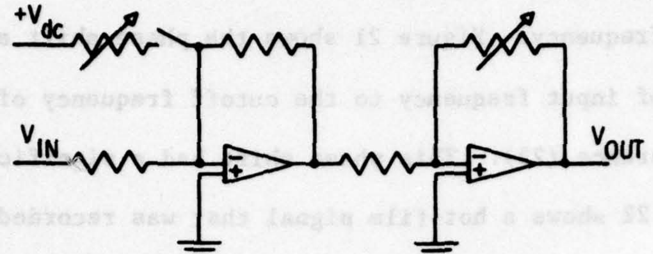

Figure 20. Schematic of Hot-Film Anemometer Signal Conditioner

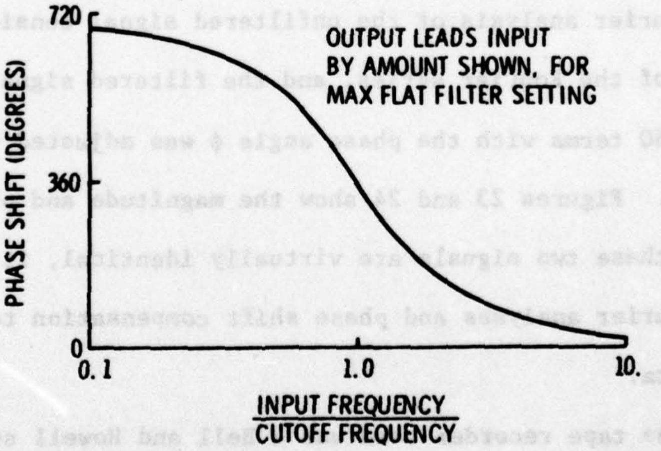

Figure 21. Phase Shift Introduced by Krohn-Hite Filter

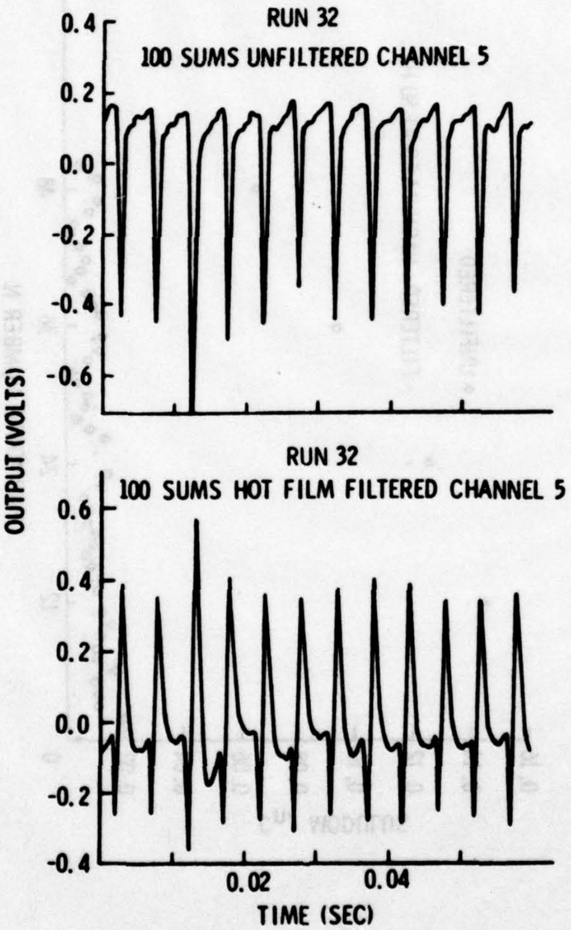

Figure 22. Unfiltered and Filtered Hot-Film Output

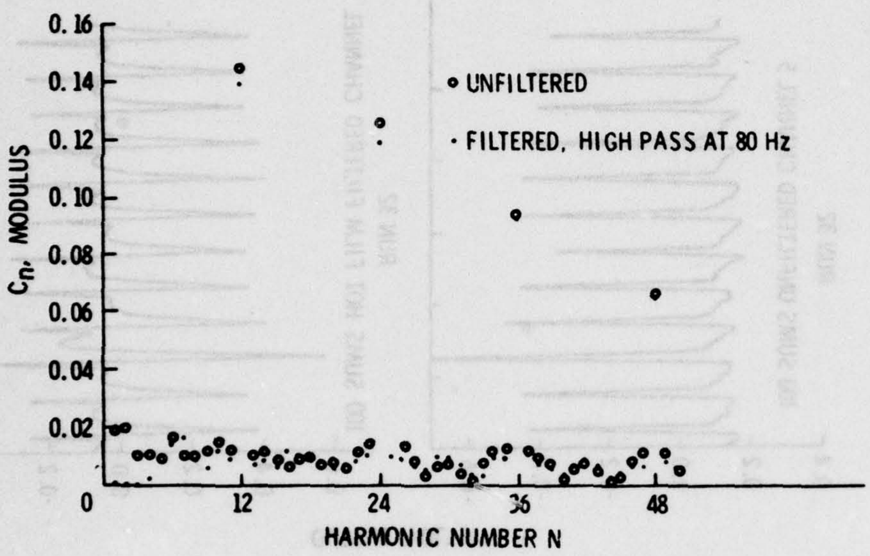

Figure 23. Comparison of Phase Angle of Unfiltered and Corrected Filtered Data

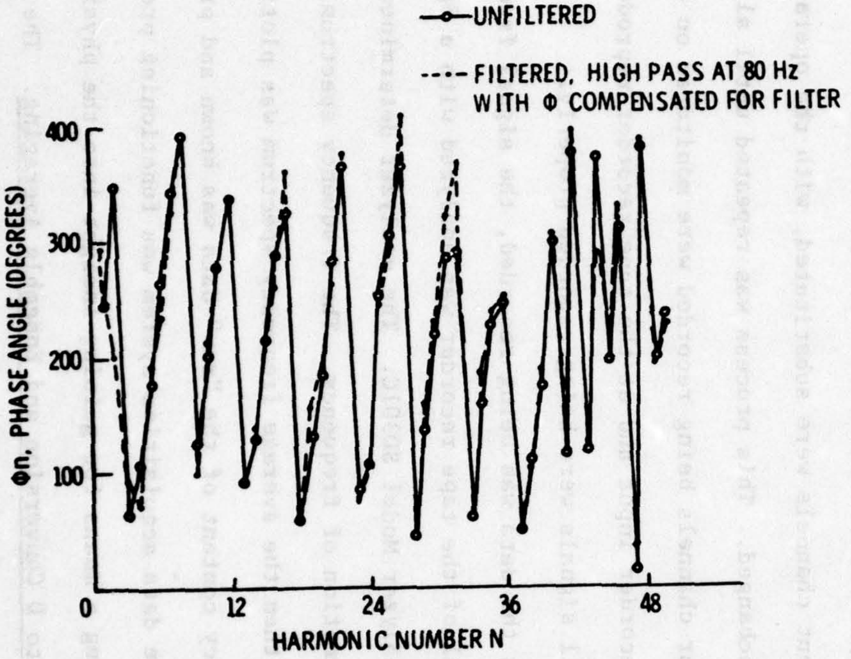

Figure 24. Comparison of Phase Angle of Unfiltered and Corrected Filtered Data

however, their magnitude was not sufficient to influence the results. Only four of the tape recorder channels were used, those channels using a single recording head, to eliminate the phase shift introduced by using different recording heads. To record the twelve channels of information (nine Pitrans, two strain gauges, and the hot-film anemometer), three channels plus the synchronization pulse were recorded, then three different channels were substituted, with the operating condition of the AFRF unchanged. This process was repeated until all the data was recorded. The four channels being recorded were monitored on an oscilloscope at the tape recorder input and at the tape recorder reproduce terminal to assure that all signals were being recorded properly.

As the data was being recorded, the signal from each reproduce terminal of the tape recorder was analyzed with a Spectral Dynamics Real Time Analyzer Model SD301C. The analyzer determined the signal output as a function of frequency. The frequency spectrum was averaged sixteen times; then the average frequency spectrum was plotted. In this way, the frequency content of the "raw" data was known and provided a useful check that the data acquisition system was functioning properly as well as providing a means for gaining insight into the physical situation.

A to D Conversion and Ensemble Averaging. The data were analyzed with an IBM System 7 real-time computer. The System 7 was programmed to perform an ensemble averaging technique. This technique enhances the portion of the signal that is periodic with respect to a synchronization pulse. Each signal, whether from pressure transducer, anemometer probe, or strain gauge bridge, can be considered to be the sum of a response to the phenomena of interest that is periodic with respect to the rotor period; e.g., the velocity fluctuation due to the rotor wake, plus a signal that is not periodic with respect to the rotor period. The nonperiodic signal could consist of turbulent fluctuations, electronic noise, or a response to events not related to the rotor/stator interaction. Since the Pitrans respond to pressure fluctuations, they not only respond to fluctuations caused by the interaction with the rotor, but also to acoustic noise generated inside and outside of the fan. As discussed later, there is a significant level of acoustic noise in the Pitran output.

Ensemble-averaging consists of the pointwise addition of a signal during one rotor period to the signal obtained during the previous rotor period. A signal periodic with the rotor period will have its amplitude doubled, thus preserving the signal, while a random or nonperiodic signal from one period will not correspond pointwise with another period and its sum will tend to diminish. To obtain the periodic signal, the summed value is then divided by the number of sums used. If a sufficiently large number of sums are used, the nonperiodic portion becomes negligible compared to the periodic portion. Figure 25 shows the effect of taking a different number of sums.

The three channels of data and the once-per-revolution synchronization pulse from the tape recorder were used as the input to System 7. The computer program used had a minimum sampling rate of 500 μsec. That is, it would digitize a point of the input signal every 500 μsec. This rate was too low to give sufficient resolution of the signal. To increase the resolution, the tape recorder playback-speed was halved, from 1-7/8 ips to 15/16 ips. The System 7 then digitized and ensembled-average the data channels sequentially, one channel at a time, storing the results from the previous channel then switching to the next channel until the analysis of all three channels was completed. The ensemble-averaged data were then punched on cards for storage and additional analysis.

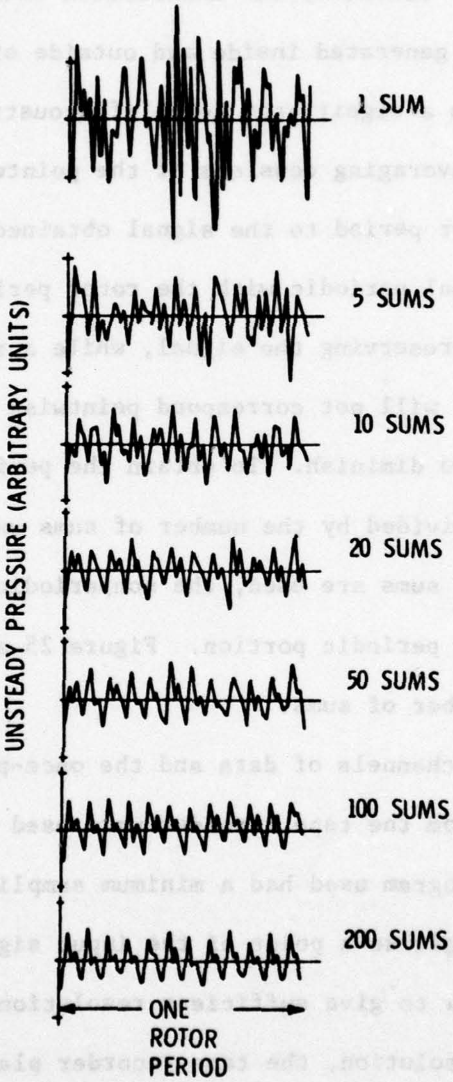

Figure 25. The Effect of the Number of Ensemble-Averaging Sums on Typical Pitran Output

Instrument Calibration

Instrumented Stator Static Calibration. A static calibration was performed to determine the sensitivity of the Pitran transducers to a known time-independent pressure. This sensitivity is then used to convert the voltage output of the transducers to a pressure. A schematic representation of the calibration procedure is shown in Figure 26. A known steady-state pressure, determined by a Validyne pressure transducer, was supplied to a test chamber containing the instrumented stator. The reference side of the Pitrans were connected to atmospheric pressure through the bottom wall of the test chamber. The pressure in the test chamber was not constant, but fell slowly with time, indicating a small amount of leakage along the O-ring seal holding the Pitran. The amount of leakage that would occur during a test with the blade installed in the AFRF is not believed to have any effect on the Pitran time-dependent output, however, since in the AFRF, the rate of change is several orders of magnitude faster. The small leakage flow would be vented to atmospheric pressure and should not affect the pressure on the reference side of the Pitran. A photograph of the stator mounted in the test chamber is shown in Figure 27.

The difference between the output of the Pitran before and after the pressure was applied and the output of the Validyne was compared to obtain the Pitran static sensitivity. This procedure was performed for a range of static pressures. The standard deviation of the sensitivity of the Pitrans at $x/c = 0.02$, 0.05, and 0.15 indicated an uncertainty of ±5%, ±3%, and ±8%, respectively.

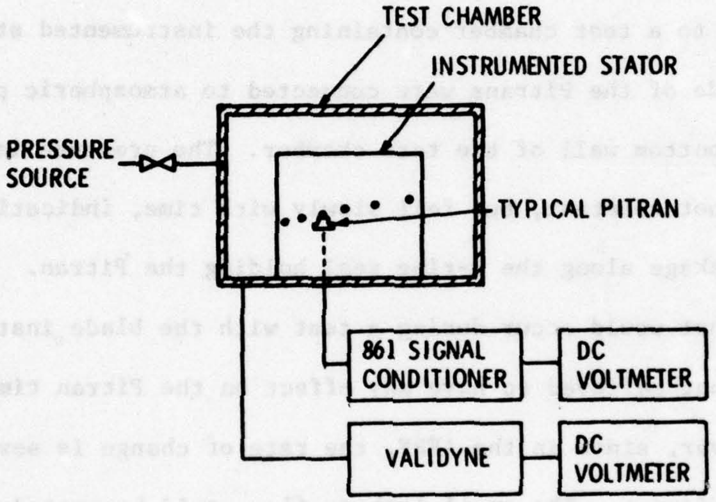
TEST CHAMBER
INSTRUMENTED STATOR
PRESSURE SOURCE
TYPICAL PITRAN
861 SIGNAL CONDITIONER
DC VOLTMETER
VALIDYNE
DC VOLTMETER

Figure 26. Schematic of Pitran Static Calibration Setup

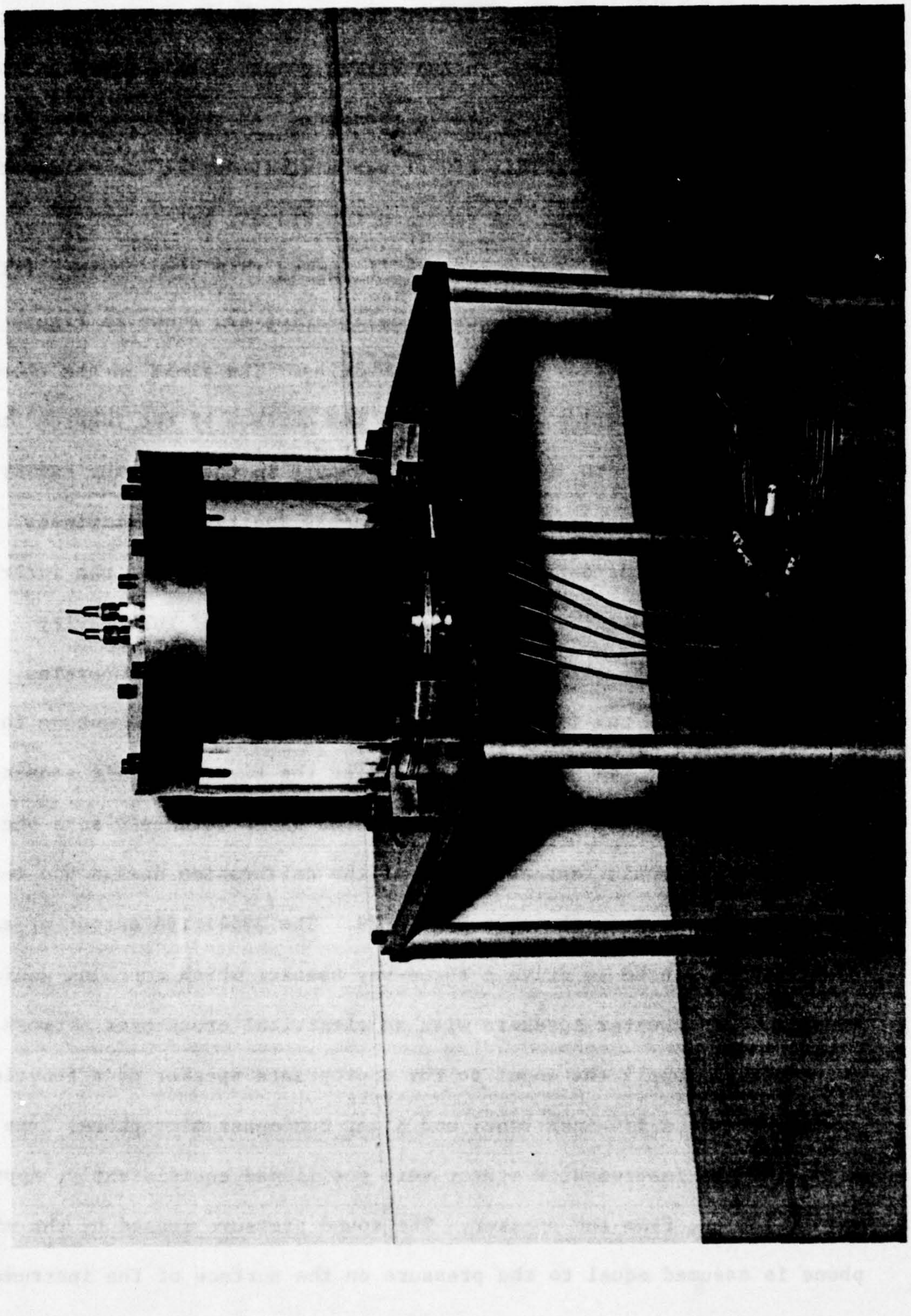

Figure 27. Pitran Static Calibration Apparatus

The 861 Signal Conditioners were modified per the manufacturer's instructions to eliminate the active feedback portion of the circuit that cancels long-term variations in the Pitran output. This permitted the Pitrans to respond to steady static pressure. In this mode, the Pitran output tended to drift. This effect was minimal during the calibration because the Pitran signal was recorded immediately before and after the pressure was applied. The signal drift during this time was negligible.

The data from a typical static calibration are shown in Figure 28.

Instrumented Stator Dynamic Calibration. The fluid in the tube-cavity system connecting the Pitran to the surface of the instrumented stator, Figure 13, can influence the pressure in the interior cavity since the fluid experiences friction and has inertia and stiffness. As discussed in greater detail in Appendix A, the pressure in the interior cavity varies in magnitude and phase as a function of tube-cavity geometry, frequency of pressure fluctuations, and fluid properties.

To determine the influence of the tube-cavity arrangement on the transducer output, as well as to determine the Pitran dynamic sensitivity, a dynamic calibration was performed. Sound waves were used as a pressure source. A schematic representation of the calibration design and instrumentation employed is shown in Figure 29. The amplified output of an oscillator was used to drive a three-way speaker which contains woofer, midrange, and tweeter speakers with an electrical cross-over network that functions to supply the input to the appropriate speaker as a function of frequency. A 1/4-inch Bruel and Kjaer condenser microphone, Type 4136, and the instrumented stator were positioned equidistantly, approximately 200 cm, from the speaker. The sound pressure sensed by the microphone is assumed equal to the pressure on the surface of the instrumented

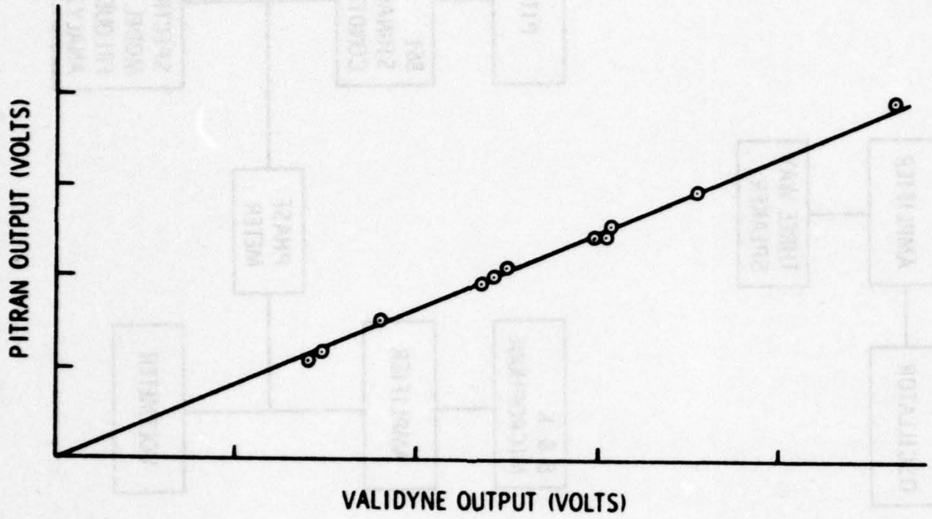

Figure 28. Typical Pitran Static Calibration Data

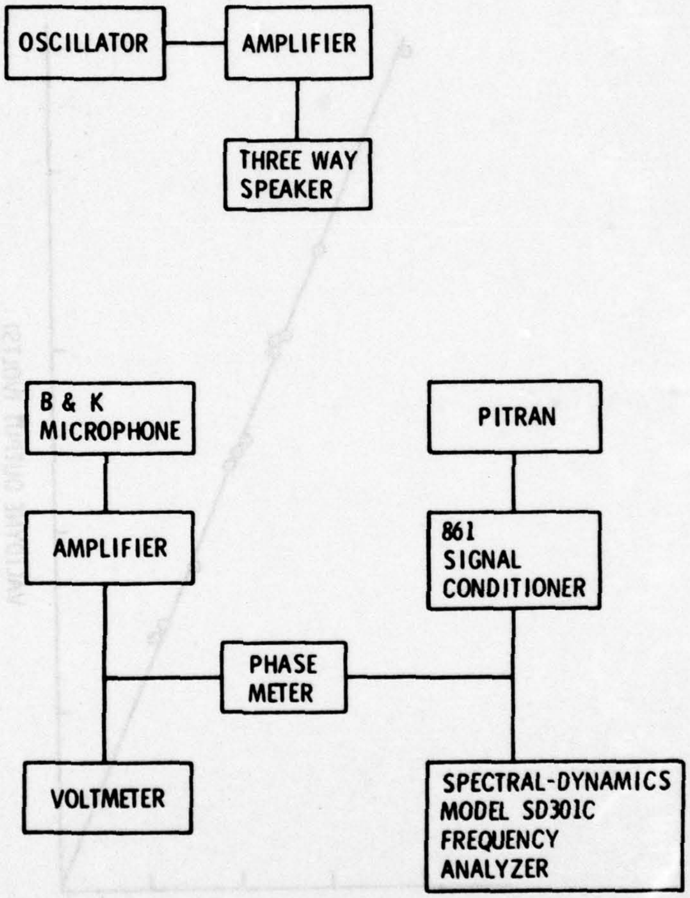
OSCILLATOR
AMPLIFIER
THREE WAY SPEAKER
B & K MICROPHONE
AMPLIFIER
PITRAN
861 SIGNAL CONDITIONER
PHASE METER
VOLTMETER
SPECTRAL-DYNAMICS MODEL SD301C FREQUENCY ANALYZER

Figure 29. Schematic of Pitran Dynamic Calibration Setup

stator. This assumption is only valid at frequencies at which the pressure increase caused by the reflection of sound waves from the stator blade and microphone are negligible.

The output of the 861 Signal Conditioner was analyzed with a Spectral Dynamics Corporation Model SD301C real-time analyzer. The analyzer output was displayed on an oscilloscope as a function of the frequency. The output of the Pitran at the frequency of the incident sound waves could be read from the oscilloscope. Using this value for the Pitran output allowed the noise present in the signal to be ignored.

Using the microphone calibration (a constant value from 150 to 15,000 Hz per the manufacturer's calibration), the microphone output and the output of each Pitran, the sensitivity of each Pitran can be determined as follows:

$$\text{Pitran Sensitivity } \frac{\text{VOLTS}}{\mu\text{ bar}} = \text{Microphone Sensitivity } \frac{\text{VOLTS}}{\mu\text{ bar}} \times \frac{\text{Pitran Output [VOLTS]}}{\text{Microphone Output [VOLTS]}} \, . \tag{4}$$

As the microphone and the instrumented stator are equidistant from the speaker, a phase meter connected between the Bruel and Kjaer amplifier output and the 861 Signal Conditioner output measures the phase difference between the pressure on the surface on the blade and the pressure in the interior cavity.

Sample calibrations showing Pitran sensitivity and phase angle versus frequency are shown in Figures 30 and 31. The effects of tube-cavity resonance can be seen. The sensitivity at frequencies greater than about 500-600 Hz may not be accurate due to wave reflection effects. The frequency at which wave reflection effects become significant are

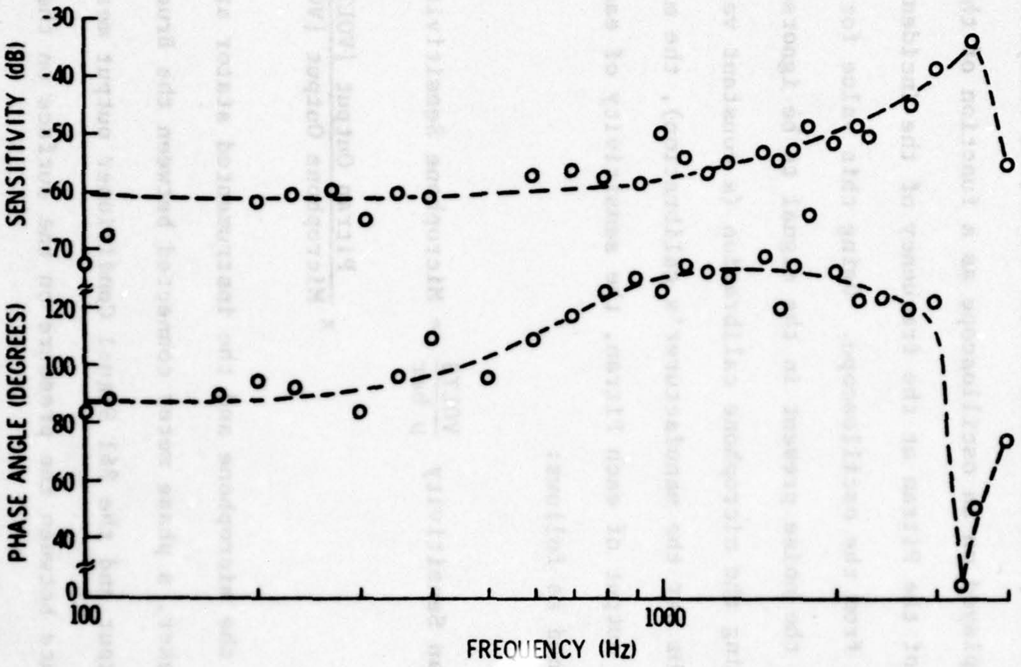

Figure 30. Results of Dynamic Calibration of Pitran at x/c = 0.15

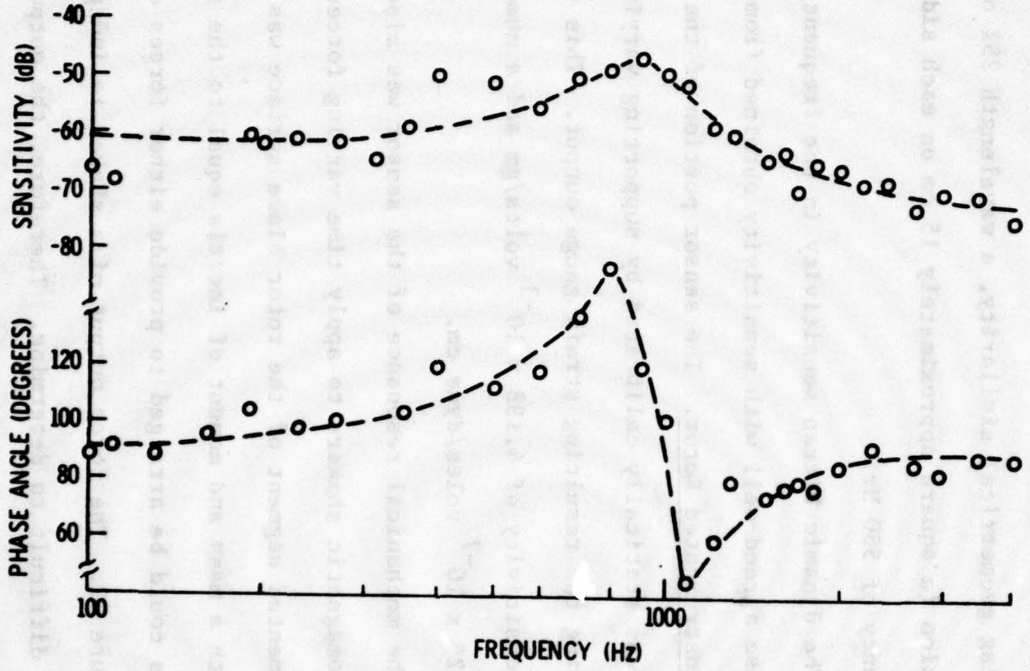

Figure 31. Results of Dynamic Calibration of Pitran at x/c = 0.95

specified in Reference (23) in which a correction for the pressure increase on a microphone diaphragm caused by the reflection of sound waves is given. A 2 dB change in the microphone sensitivity occurs when the incident wavelength is 25% of the microphone diaphragm diameter. Assuming geometrical similarity, a wavelength 25% of the stator blade dimension (a square approximately 15 cm on each side) corresponds to a frequency of 550 Hz.

The dynamic Pitran sensitivity in the frequency range giving a flat response agreed well with sensitivity obtained from the static calibration.

Instrumented Rotor. The sensor portion of the instrumented rotor blade was statically calibrated by supporting varying known masses and recording the resulting strain gauge output. This resulted in a force cell sensitivity of 4.198 x 10^{-3} volts/gm and a moment cell sensitivity of 7.929 x 10^{-7} volts/dyne cm.

The mechanical resonance of the sensor was also investigated using electromagnetic shakers to apply time varying forces and moments. The instrumented segment of the rotor blade surface was replaced by a metal bar with a mass and moment of inertia equal to the rotor segment. The shakers could be arranged to provide either forces or moments as shown in Figure 32. The force output of a shaker is independent of frequency, but is difficult to determine. Therefore, the output of the shaker is determined using the static calibration results at frequencies much less than the resonant frequencies of the sensor. The dynamic response of the sensor to an applied force is shown in Figure 33.

Hot-Film Anemometer. The hot-film anemometer was calibrated in a small wind tunnel shown schematically in Figure 34. This wind tunnel consists of a centrifugal fan, connecting ducting, a constricted test

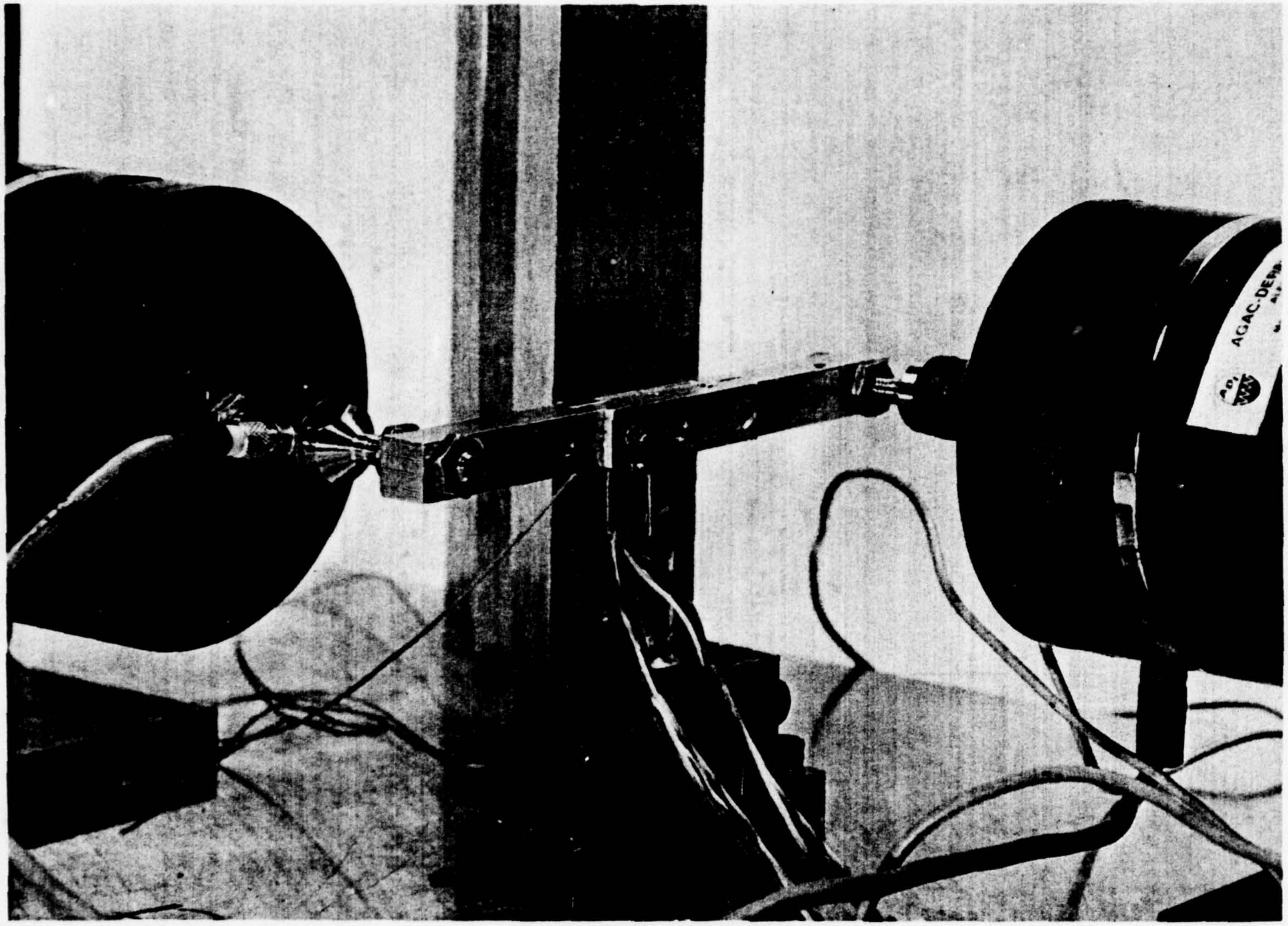

Figure 32. Dynamic Calibration Setup of Instrumented Rotor Blade

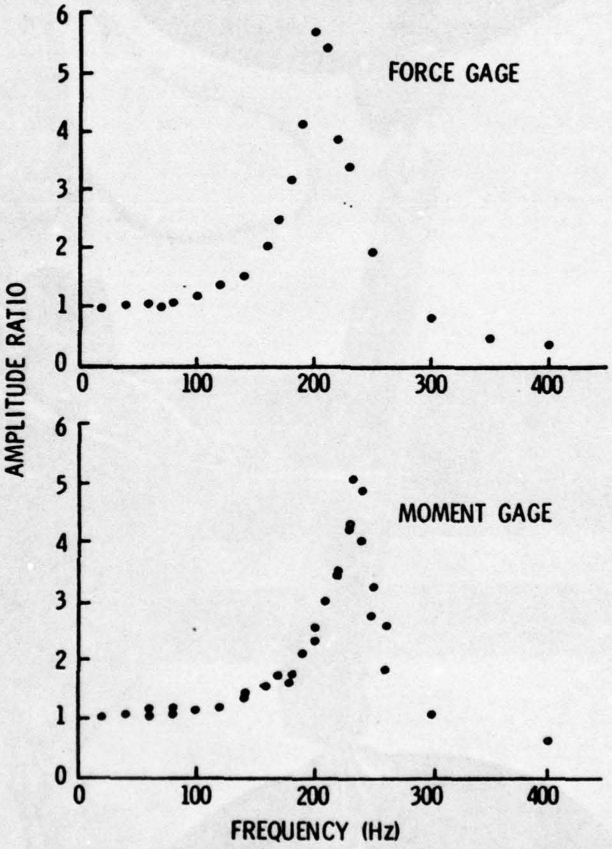

Figure 33. Dynamic Response of Instrumented Rotor Blade

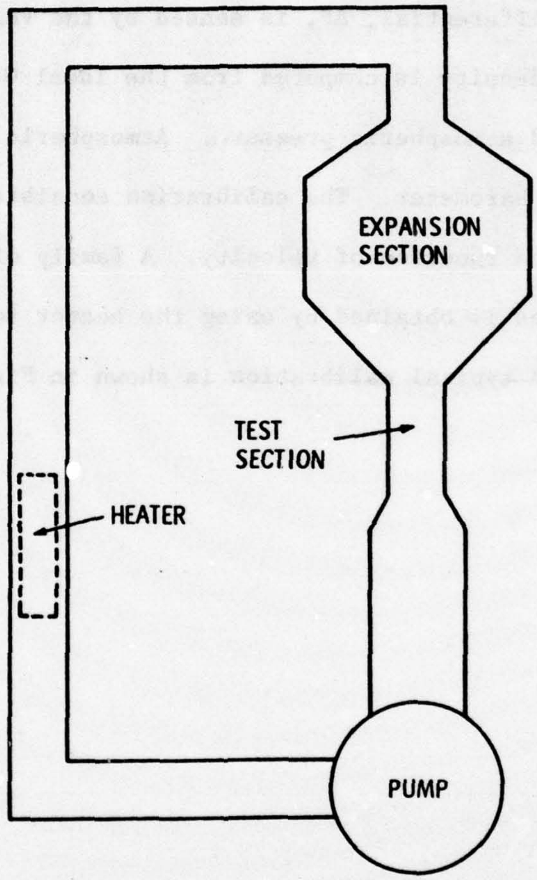
EXPANSION SECTION
TEST SECTION
HEATER
PUMP

Figure 34. Schematic of Hot-Film Calibration Tunnel

section, a large expansion section, a heater, and associated electrical controls. The hot-film probe is inserted into a probe holder in the test section. The probe holder also contains a temperature sensor. The velocity in the test section sensed by the hot film is computed knowing the pressure drop across the inlet nozzle and the density of the flow. The pressure differential, ΔP, is sensed by the Validyne pressure transducer and the density is computed from the Ideal Gas Law, knowing the temperature and atmospheric pressure. Atmospheric pressure was measured with a mercury barometer. The calibration consists of recording the hot-film output as a function of velocity. A family of curves for different air temperatures is obtained by using the heater to raise the air temperature. A typical calibration is shown in Figure 35.

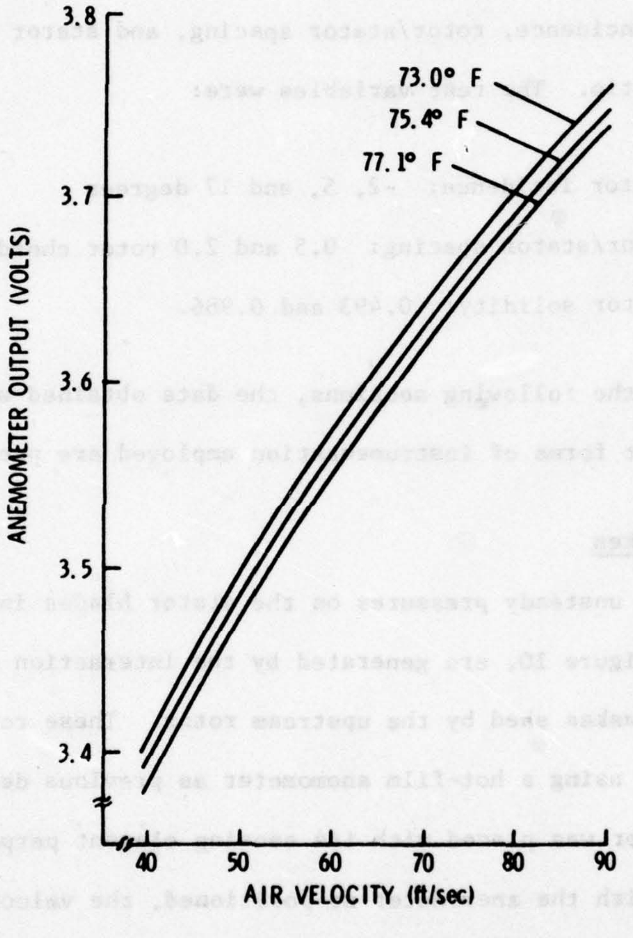

Figure 35. Typical Hot-Film Calibration Data

PRESENTATION AND DISCUSSIONS OF EXPERIMENTAL RESULTS

Using the instrumentation described above, measurements were conducted on the wakes shed by the rotor, the unsteady static pressures on the stator blades, and the unsteady lift and moment on the instrumented rotor blade. These measurements were conducted as a function of stator steady incidence, rotor/stator spacing, and stator solidity, or space-to-chord ratio. The test variables were:

Stator incidence: -2, 5, and 17 degrees
Rotor/stator spacing: 0.5 and 2.0 rotor chords
Stator solidity: 0.493 and 0.986.

In the following sections, the data obtained with each of these different forms of instrumentation employed are presented and discussed.

Rotor Wakes

The unsteady pressures on the stator blades in this experimental setup, Figure 10, are generated by the interaction of the stator blades and the wakes shed by the upstream rotor. These rotor wakes were measured using a hot-film anemometer as previous described. The anemometer was placed with its sensing element perpendicular to the flow. With the anemometer so positioned, the velocity variation as a function of time was determined. Knowing the position of the anemometer and the absolute flow angle, it is possible to determine the velocity variation due to the rotor wakes at the leading edge of the instrumented stator blades.

An important element in obtaining these time varying data is to reference the time from a given spatial location as the rotor blades move past the hot-film anemometer. This was accomplished by employing the once-per-revolution pulse from the rotor shaft mounted photoelectric device described above. With this once-per-revolution pulse, it is possible to ensemble-average the output of the hot-film anemometer to remove the random variations in the flow.

Figure 36 (a) and (b) shows the ensemble-averaged velocity variations at the instrumented stator leading edge as a function of time for each of the rotor/stator spacings, stator solidities, and incidence angles investigated. The instantaneous velocity is nondimensionalized by the time-mean circumferential averaged velocity which is given by the D.C. voltage output of the anemometer. Shown in Figure 36 are the wakes for one revolution of the twelve-bladed rotor, i.e., between consecutive trigger pulses. The rotor shaft speed (1000 RPM) was identical for stator incidences of -2 and 5 degrees. The RPM was increased to 1428 RPM to obtain the stator incidence condition of 17 degrees as evidenced by the shorter lapsed time for one rotor revolution.

At a rotor/stator spacing of 0.5 rotor chord lengths, Figure 36 (a), the wakes are observed to have a sharper deficit in velocity than observed at a rotor/stator spacing of 2.0. This is caused by the mixing and diffusion of the wake as the distance from the rotor trailing edge is increased. It is also evident that the blades are not all geometrically similar. One blade in particular has a greater velocity deficit, which is presumably caused by a slight misalignment of the blade in the rotor hub.

To describe the response of the stator blades to the wakes of the rotor blades, an averaged wake was constructed from those measured in one rotor revolution. This was accomplished by breaking the measurements,

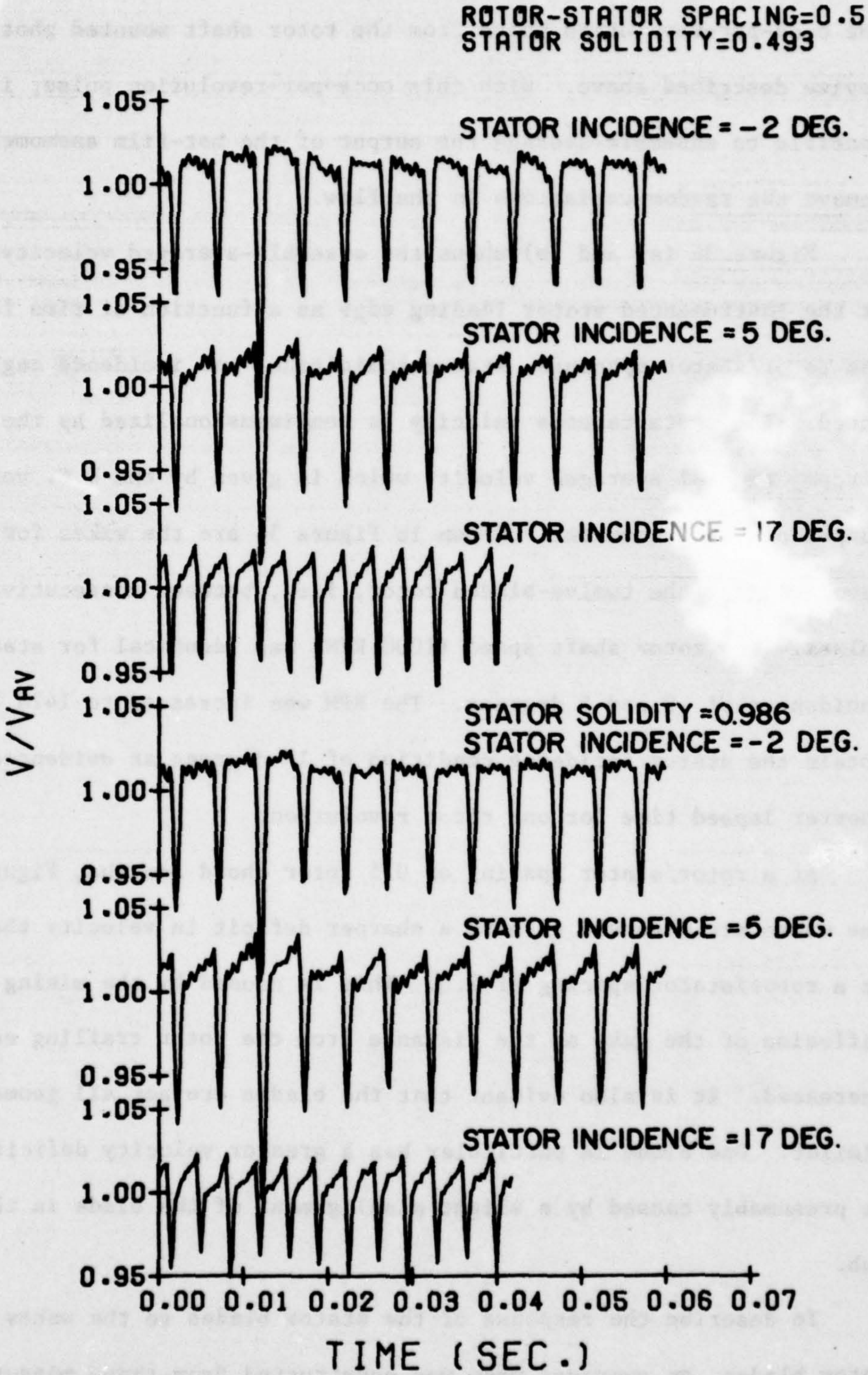

Figure 36 (a). Rotor Wake at the Stator Leading Edge

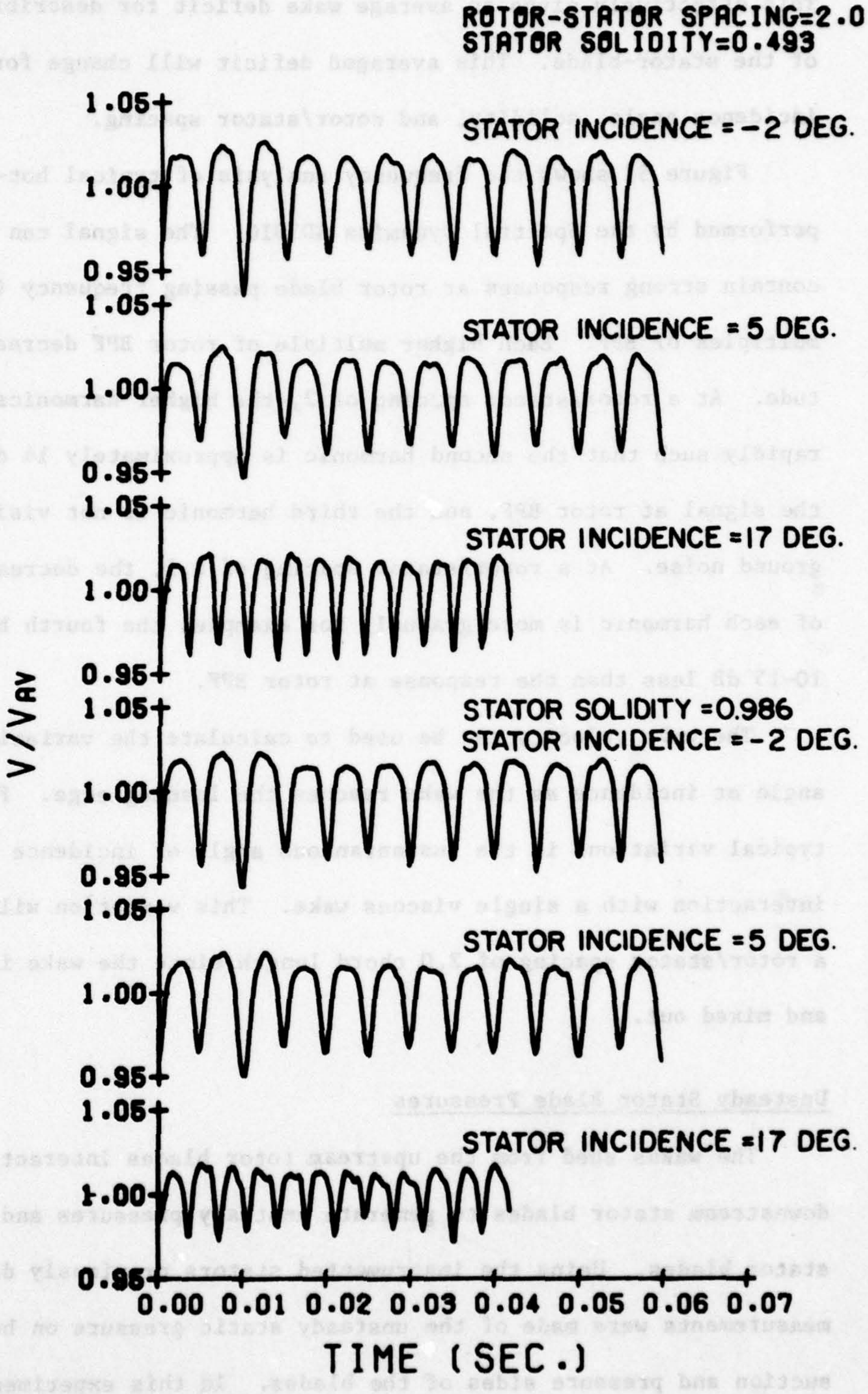

Figure 36 (b). Rotor Wake at the Stator Leading Edge

Figure 36, into twelve equal time intervals which were then averaged. This effectively gives an average wake deficit for describing the response of the stator-blade. This averaged deficit will change for each stator incidence angle, solidity, and rotor/stator spacing.

Figure 37 shows the frequency analysis of typical hot-film signals performed by the Spectral Dynamics SD301C. The signal can be seen to contain strong responses at rotor blade passing frequency (BPF) and multiples of BPF. Each higher multiple of rotor BPF decreases in magnitude. At a rotor/stator spacing of 2, the higher harmonics decrease rapidly such that the second harmonic is approximately 14 dB less than the signal at rotor BPF, and the third harmonic is not visible above background noise. At a rotor/stator spacing of 0.5, the decrease in magnitude of each harmonic is more gradual; for example, the fourth harmonic is 10-15 dB less than the response at rotor BPF.

The wake velocity can be used to calculate the variation of the angle at incidence as the wake reaches the leading edge. Figure 38 shows typical variations in the instantaneous angle of incidence during the interaction with a single viscous wake. This variation will decrease at a rotor/stator spacing of 2.0 chord length since the wake is more diffused and mixed out.

Unsteady Stator Blade Pressures

The wakes shed from the upstream rotor blades interact with the downstream stator blades to generate unsteady pressures and lift on the stator blades. Using the instrumented stators previously described, measurements were made of the unsteady static pressure on both the suction and pressure sides of the blades. In this experiment, the pressure side of the stator was defined as that surface facing the rotor

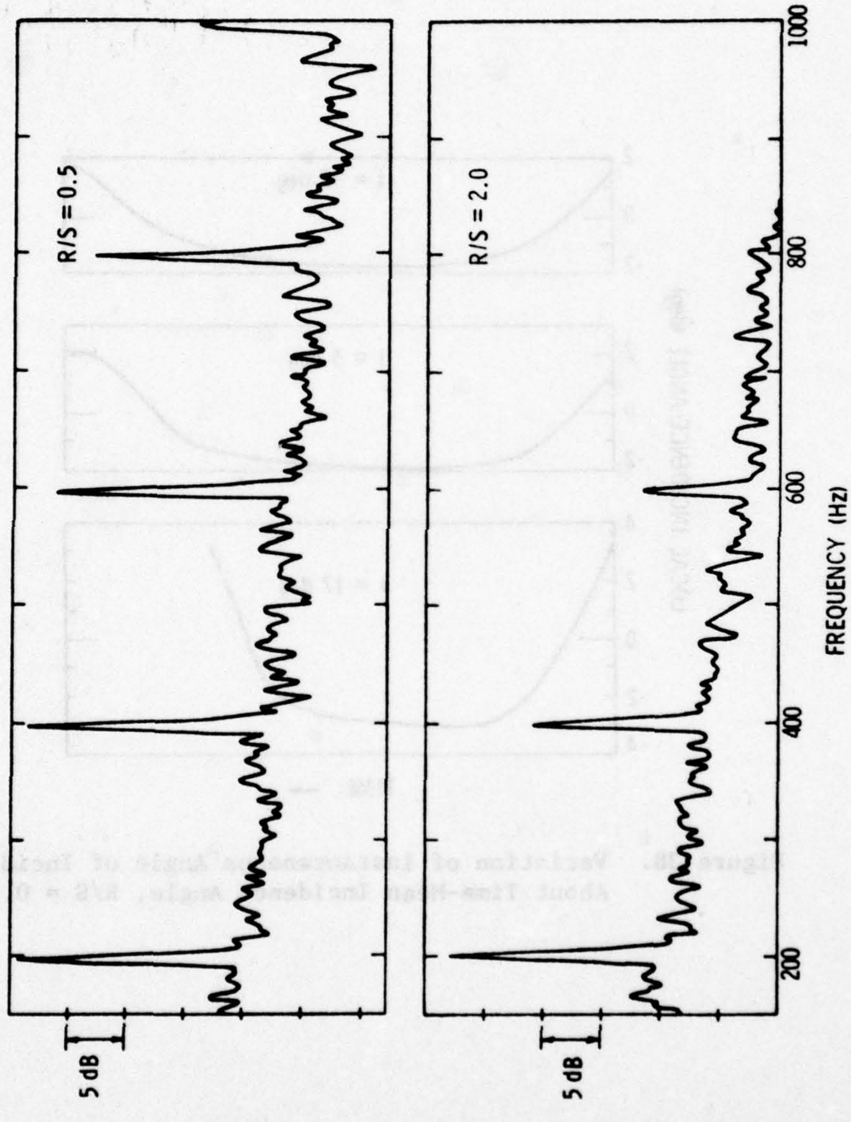

Figure 37. Spectral Analysis of Typical Hot-Film Output

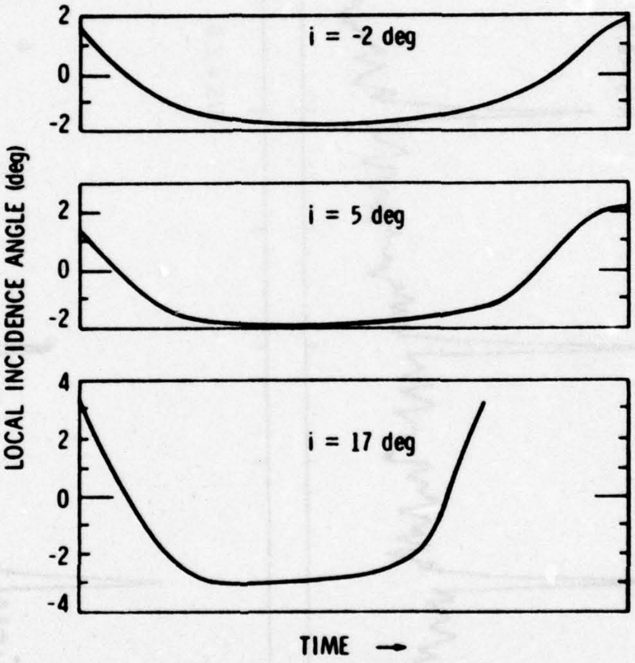

Figure 38. Variation of Instantaneous Angle of Incidence About Time-Mean Incidence Angle, R/S = 0.5

as the rotor moved toward the stator. The suction surface is then the opposite surface. This definition is consistent with the circumferential-mean steady flow which impinges on the pressure surface at a positive value of stator incidence.

The spectral analyses performed by the Spectral Dynamics Model SD301C real-time analyzer were used as a means of assuring that the data acquisition system was functioning properly and as an aid to understanding the nature of the unsteady pressures recorded by the Pitrans. At each chordwise location, the signal consists of a broadened background response, presumably from turbulence in the flow, and strong response at discrete frequencies. These discrete frequencies correspond to the rotor blade passing frequency, its multiples, and the downstream auxiliary fan blade passing frequency and its multiples. Figure 39 shows a typical Pitran response in the frequency domain. Also shown is the magnitude of the Fourier coefficients of the same data after being ensemble-averaged using 100 sums. Quite striking is the absence of the auxiliary fan blade passing frequency in the ensemble-averaged data. Since it is not harmonic with respect to the rotor period, the ensemble-averaging eliminated this response.

As discussed above, these unsteady static pressures were obtained at two values of rotor/stator spacing (0.5 and 2.0 rotor chord lengths), three stator incidences (-2, 5, and 17 degrees), and two stator solidities (0.493 and 0.986). As a result of this large number of variables, there was a considerable volume of data obtained. The presentation of all of these data is not possible. Therefore, a presentation will be made of some typical data to demonstrate the type of data obtained and the trends observed. These data will then be summarized to show the effects of the various test variables on the unsteady surface pressures.

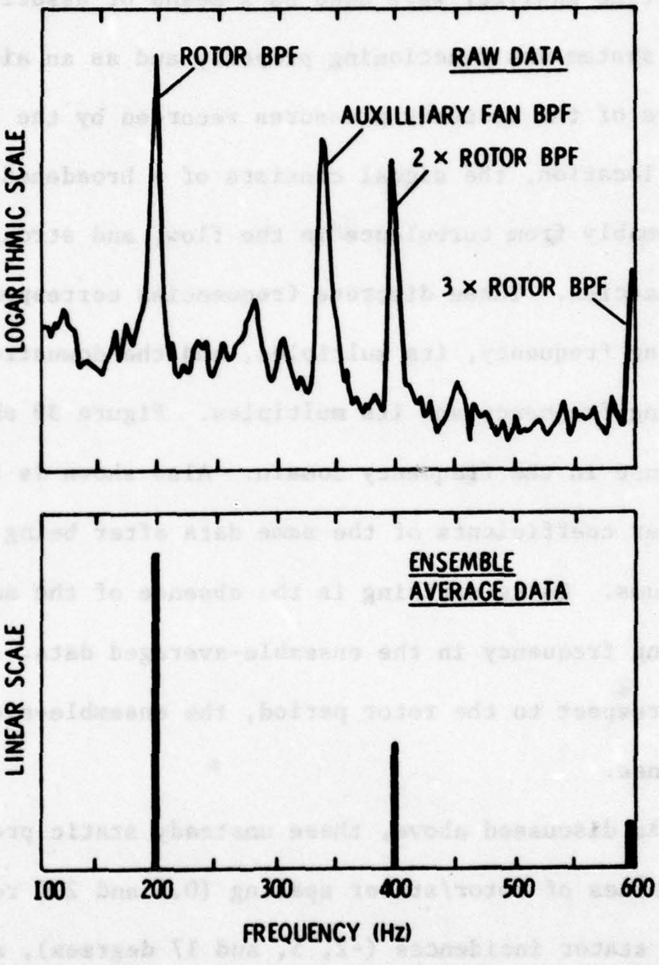

Figure 39. Typical Spectral Representation of Pitran Output

One method of presenting these data is to show the variation of static pressure on both the suction and pressure surfaces as a function of time. These measurements were obtained by taping one side of the transducer cavity closed, Figure 13. The pressures observed are then referenced to the atmospheric pressure, P_{atm}, acting on the back of the transducer. The resulting signals from the Pitran transducers were then ensemble-averaged and converted to a pressure, $\tilde{p}$, (psi) using the calibration constants obtained during the calibration of the Pitrans. These data were nondimensionalized by the fluid mass density, ρ, the time-mean circumferentially averaged velocity at the stator inlet, V, and the maximum deficit in the rotor wake, W_{max}. This results in an unsteady pressure coefficient for both the suction and pressure sides of the stator blade. Examples of these data are presented in Figures 40 and 41 for a stator incidence of -2 degrees and Figures 42 and 43 for a stator incidence of 17 degrees. In these figures, the time $t = 0$ is referenced to the once-per-revolution pulse. The presented data are for a rotor/stator spacing of 2.0 rotor chords and a stator solidity, at the mean radius of 0.986, and show the response of the transducers located at the various chordwise positions. Similar data were obtained for a rotor/stator spacing of 0.5 and a stator solidity of 0.493. These data are similar to those obtained by other investigators, Lefcort (9), Satyanarayana (17), and Ostdiek (24), in that large amplitude variations are observed near the leading edge of the blade which decrease rapidly with distance along the chord.

Large angles of incidence produce much larger pressure amplitude variations on the suction surface near the leading edge than are produced at smaller angles of incidence, Figure 42 versus Figure 40. Furthermore,

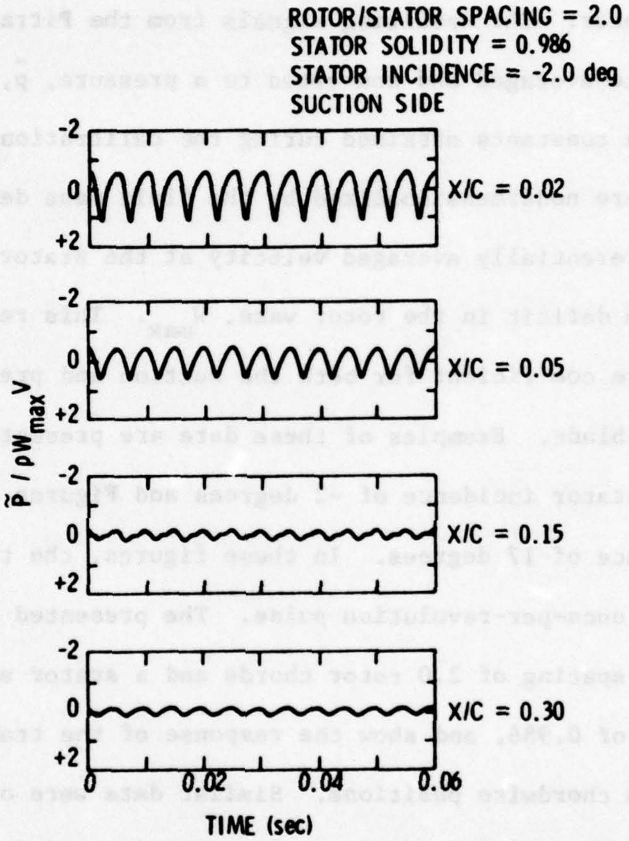

Figure 40. Unsteady Pressure Coefficient versus Real Time-Suction Surface, i = -2 deg

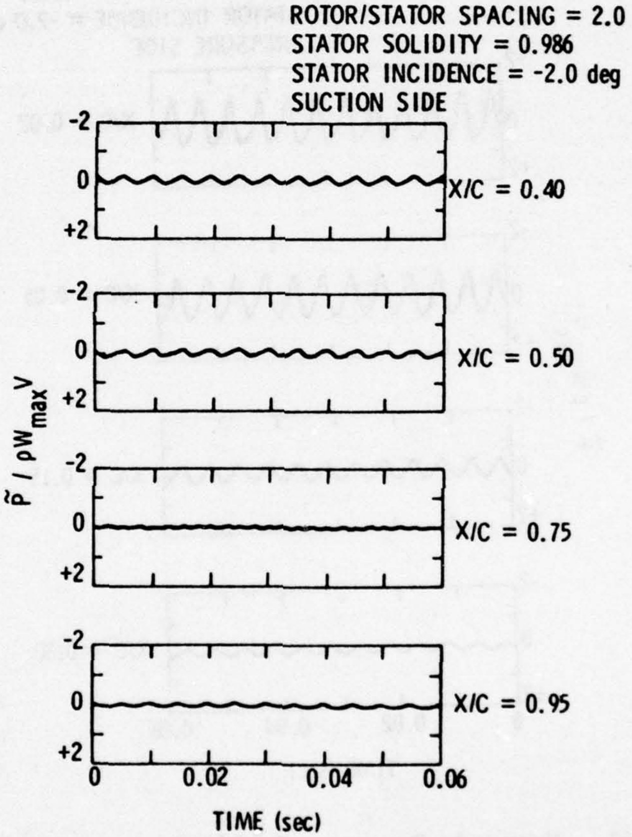

Figure 40. Unsteady Pressure Coefficient versus Real Time-Suction Surface, i = -2 deg (Continued)

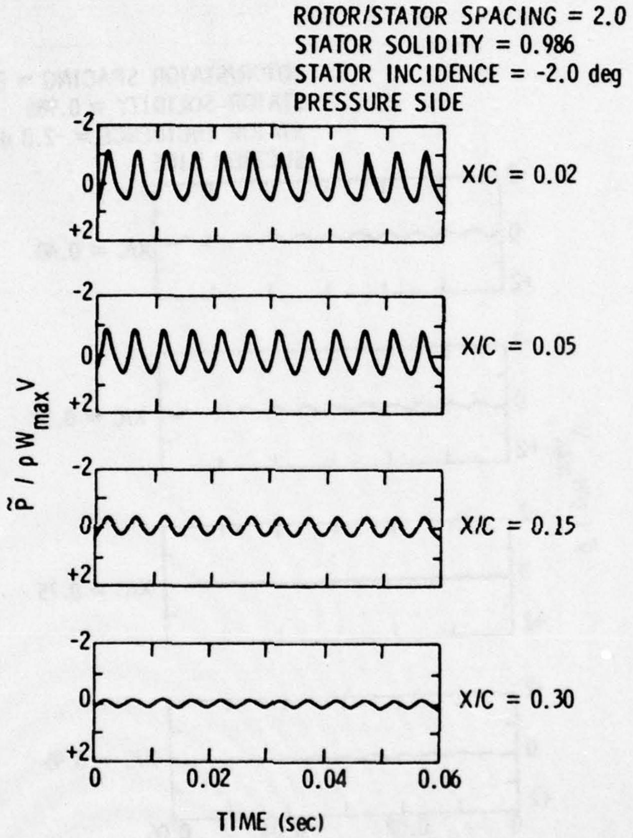

Figure 41. Unsteady Pressure Coefficient versus Real Time-Pressure Surface, i = -2 deg

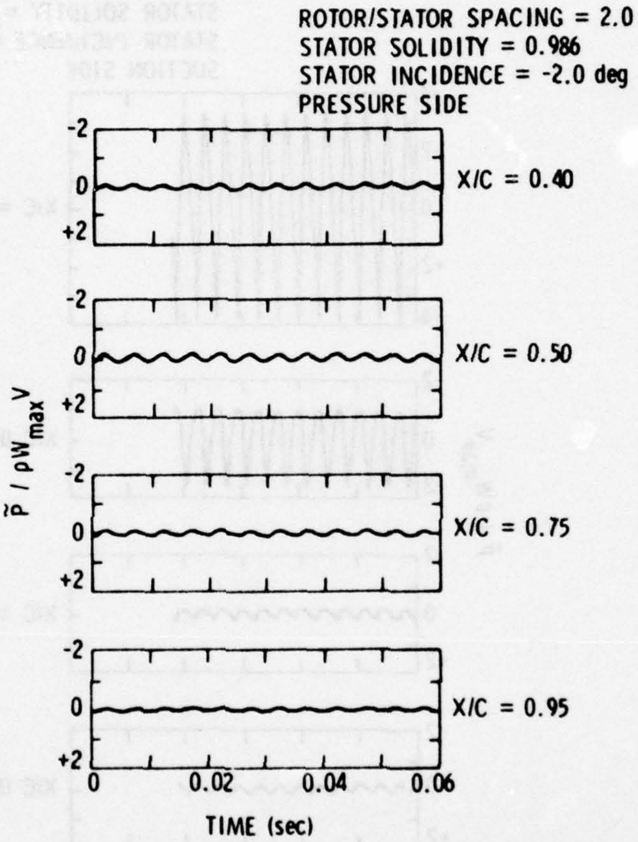

Figure 41. Unsteady Pressure Coefficient versus Real Time-Pressure Surface, i = -2 deg (Continued)

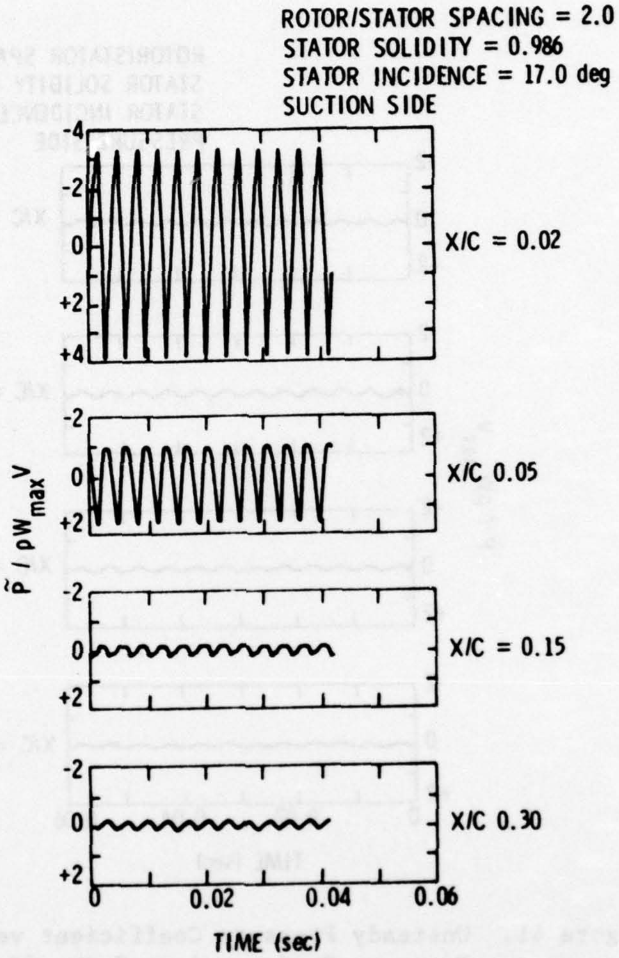

Figure 42. Unsteady Pressure Coefficient versus Real Time-Suction Surface, i = 17 deg

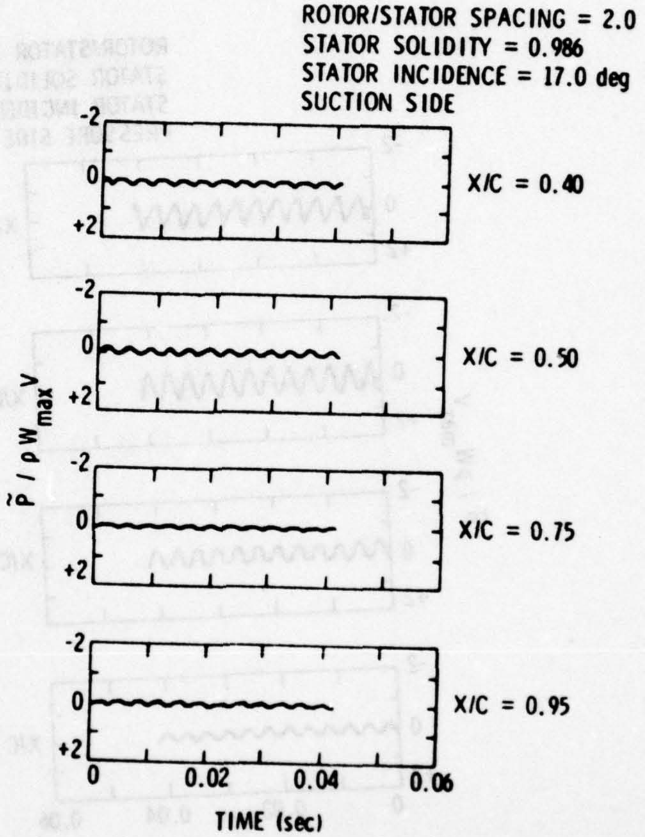

Figure 42. Unsteady Pressure Coefficient versus Real Time-Suction Surface, i = 17 deg (Continued)

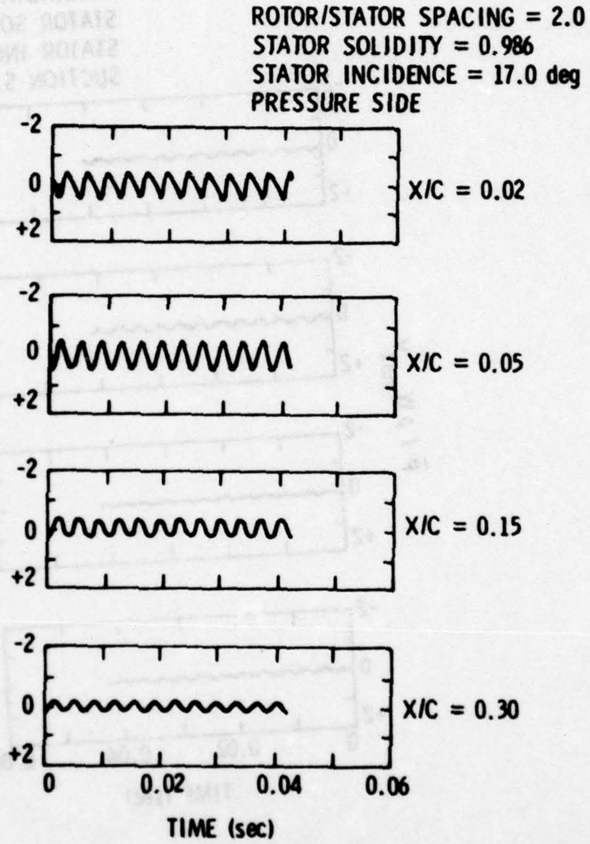

Figure 43. **Unsteady Pressure Coefficient versus Real Time-Pressure Surface, i = 17 deg**

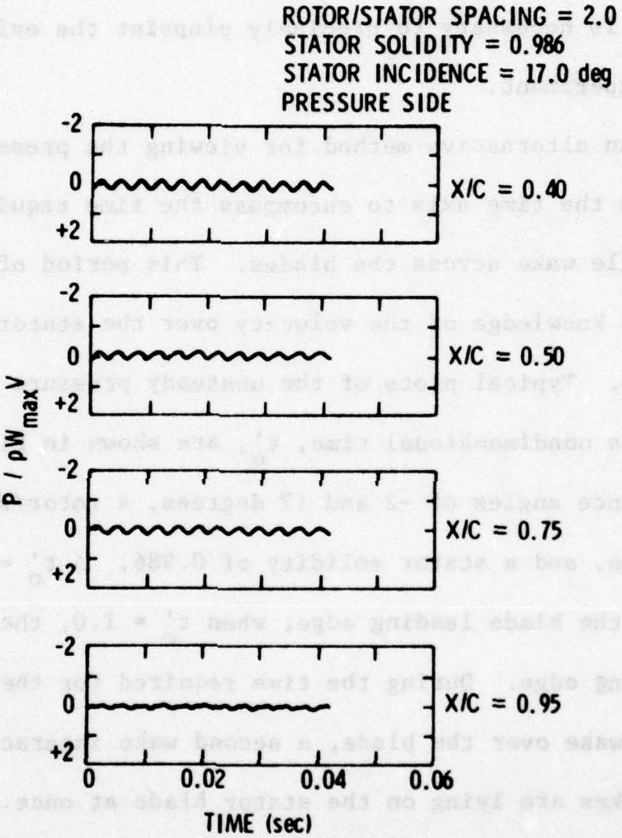

Figure 43. Unsteady Pressure Coefficient versus Real Time-Pressure Surface, i = 17 deg (Continued)

the pressure coefficient on the suction surface for i = 17 degrees at locations aft of the x/c = 0.05 position shows some degree of flattening near the pressure peaks. This type of response resembles that obtained by Satyanarayana (17) for a fixed cascade, and by Carter and St. Hilaire (25) on the oscillating airfoil. In both cases, this flattening is attributed to local flow separation. However, a more detailed experimental study is necessary to precisely pinpoint the existence of separation in the experiment.

An alternative method for viewing the pressure fluctuations is to expand the time axis to encompass the time required for the passage of a single wake across the blades. This period of time can be computed from a knowledge of the velocity over the stator and the stator chord length. Typical plots of the unsteady pressure coefficient as a function of this nondimensional time, t'_o, are shown in Figures 44 and 45 for stator incidence angles of -2 and 17 degrees, a rotor/stator spacing of 2.0 chord lengths, and a stator solidity of 0.986. A $t'_o = 1.0$, the wake centerline is at the blade leading edge; when $t'_o = 1.0$, the centerline is at the trailing edge. During the time required for the passage of a single rotor wake over the blade, a second wake interacts with the blade. Thus, two wakes are lying on the stator blade at once. These plots permit the examination of the variation of the suction and pressure surface pressure coefficients as a function of chordwise position and time.

One significant feature of these data is shown in Figure 45. There is an obvious phase shift in the pressure on the suction surface between locations x/c = 0.02 and x/c = 0.05 when the stator blade was operated at 17 degrees of incidence. The results of the Fourier analysis of these data can be used to quantify such phase shift observations. Each pressure

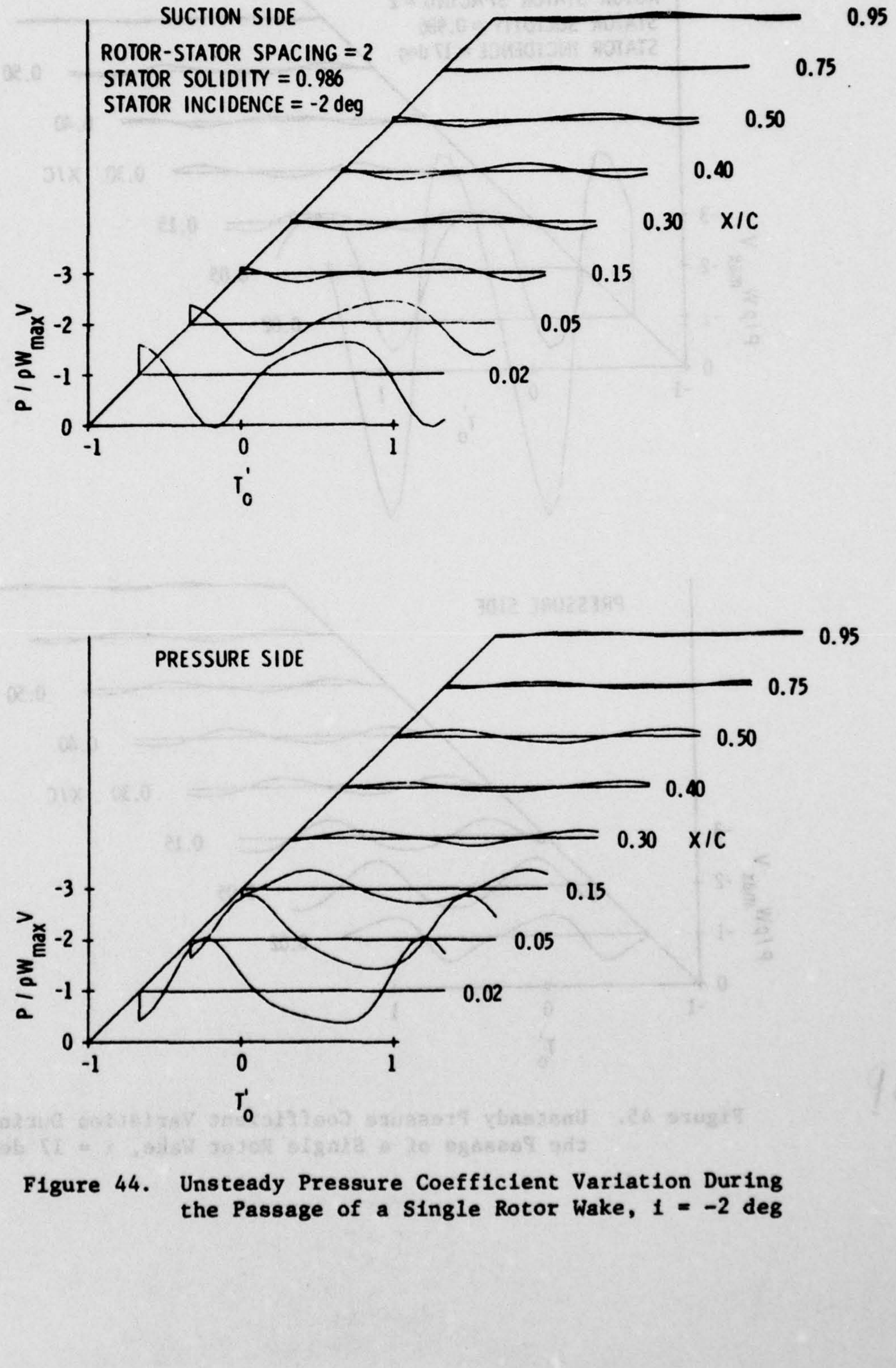

Figure 44. Unsteady Pressure Coefficient Variation During the Passage of a Single Rotor Wake, i = -2 deg

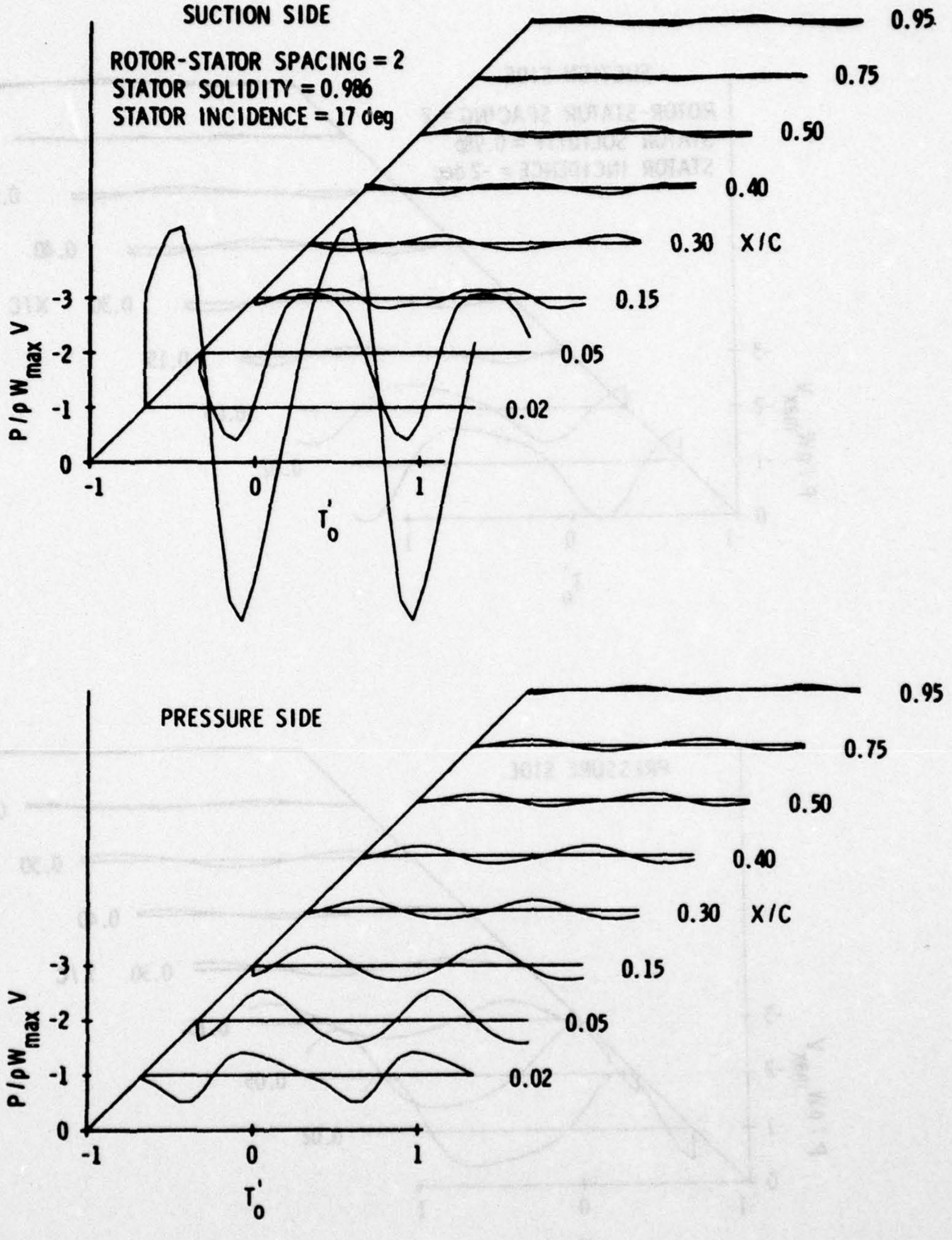

Figure 45. Unsteady Pressure Coefficient Variation During the Passage of a Single Rotor Wake, i = 17 deg

signal was decomposed into the form:

$$\tilde{p}(t) = \sum_{n=1}^{\infty} C_n \cos (n\Theta - \phi_n) \; , \qquad (5)$$

where one period of the signal (360°) is defined as one rotor revolution. Thus, n = 12 is the first harmonic of the blade passing frequency, and n = 24 is the second harmonic of blade passing frequency. The phase angle of the unsteady pressures on the suction and pressure surfaces of the blade are presented in Figures 46 through 49 as a function of x/c for different values of rotor/stator spacing, solidity, and incidence angle. These phase angles are referenced to the signal from the once-per-revolution timing signal. Thus, these data indicate the relative behavior of the pressures on the suction and pressure sides of the blade. They do not, however, indicate the absolute value of the phase angle of the pressure fluctuations with respect to the wake as it interacts with the leading edge of the blade.

Of major interest in these data is the observation that the phase angle is nearly constant on the pressure surface of the blade while it undergoes significant changes on the suction surface. This behavior is similar to that observed by Satyanarayana (17) for a cascade of airfoils operated in a sinusoidal low frequency, nonconvected disturbance flow. However, the variations observed by Satyanarayana were continuous compared to the erratic behavior observed in these tests. Further, Satyanarayana showed his variations in phase angle to be a function of the stagger angle of the blade. In these tests, it is suspected that these large variations in phase angle are associated with local flow separation. This is supported by the fact that at -2 degrees incidence, the variations of phase angle are much less than at 17 degrees incidence.

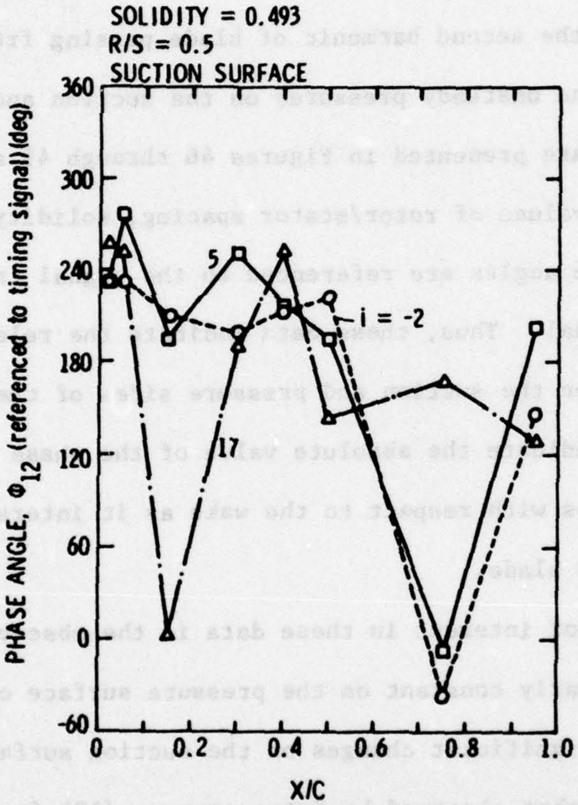

Figure 46. Unsteady Pressure Phase Angle versus x/c - R/S = 0.5, σ = 0.493

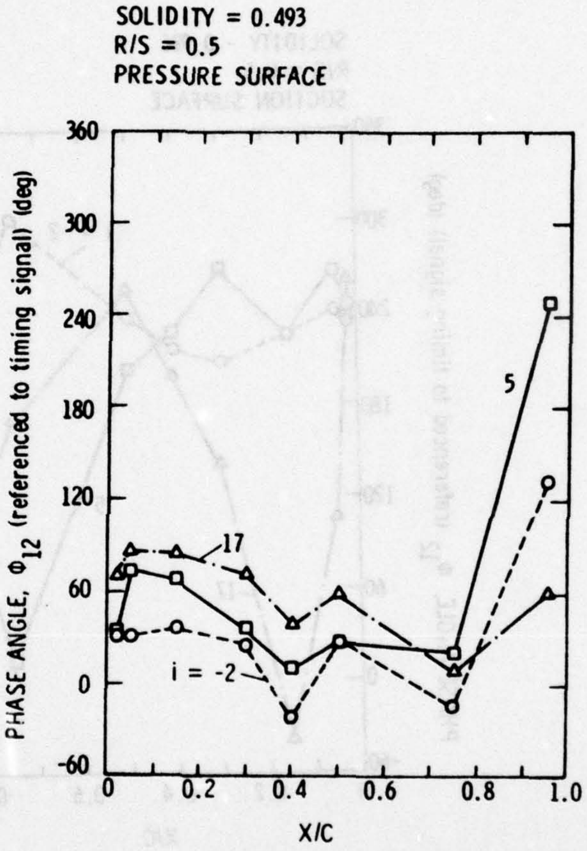

Figure 46. Unsteady Pressure Phase Angle versus x/c - R/S = 0.5, σ = 0.493 (Continued)

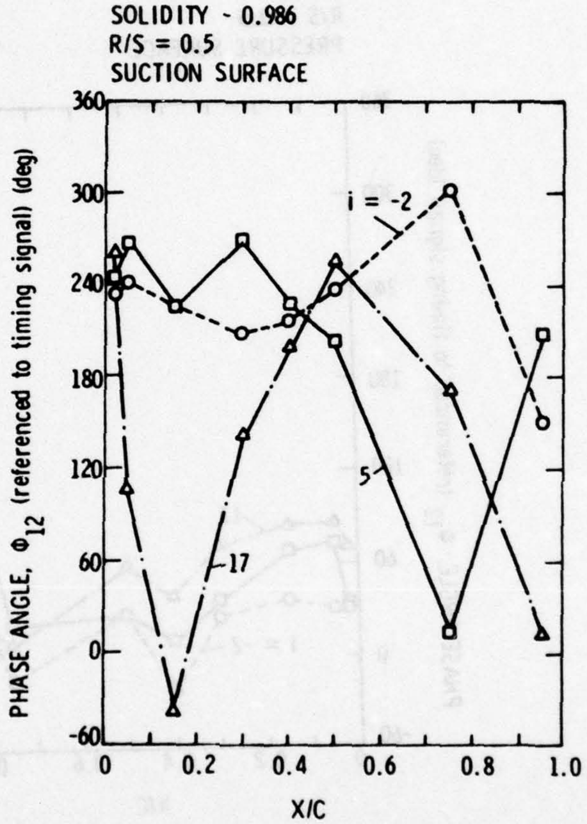

Figure 47. Unsteady Pressure Phase Angle versus x/c - R/S = 0.5, σ = 0.986

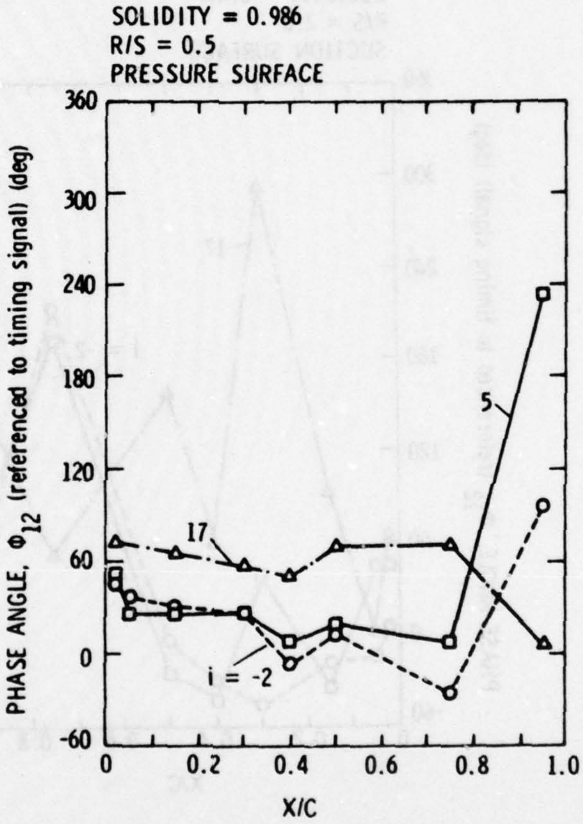

Figure 47. Unsteady Pressure Phase Angle versus x/c - R/S = 0.5, σ = 0.986 (Continued)

AD-A069 619 PENNSYLVANIA STATE UNIV UNIVERSITY PARK APPLIED RESE--ETC F/G 20/4
INVESTIGATION OF THE UNSTEADY PRESSURE DISTRIBUTION ON THE BLAD--ETC(U)
NOV 78 G FRANKE N00024-79-C-6043
UNCLASSIFIED ARL/PSU/TM-78-300 NL

2 OF 2
AD
A069619

END
DATE
FILMED
7-79
DDC

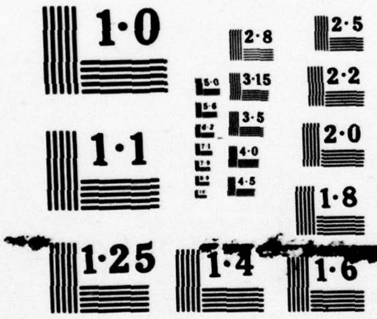
1·0
2·8
2·5
3·15
2·2
5·0
5·6
3·5
2·0
1·1
4·0
4·5
1·8
1·25
1·4
1·6

NATIONAL BUREAU OF STANDARDS
MICROCOPY RESOLUTION TEST CHART

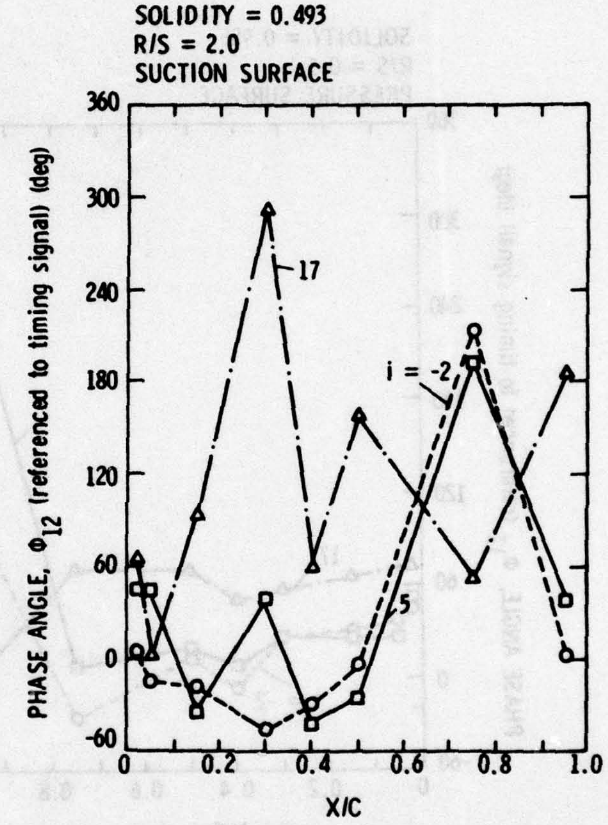

Figure 48. Unsteady Pressure Phase Angle versus x/c - R/S = 2.0, σ = 0.493

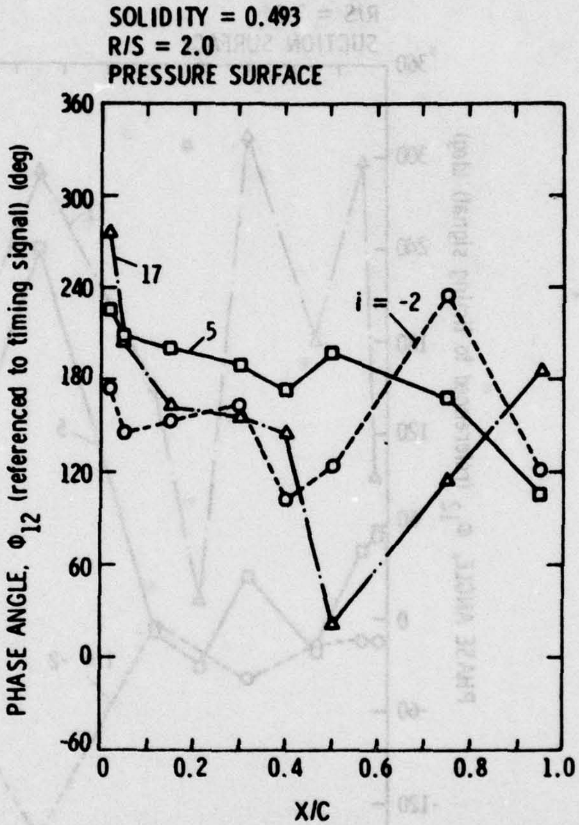

Figure 48. Unsteady Pressure Phase Angle versus x/c - R/S = 2.0, σ = 0.493 (Continued)

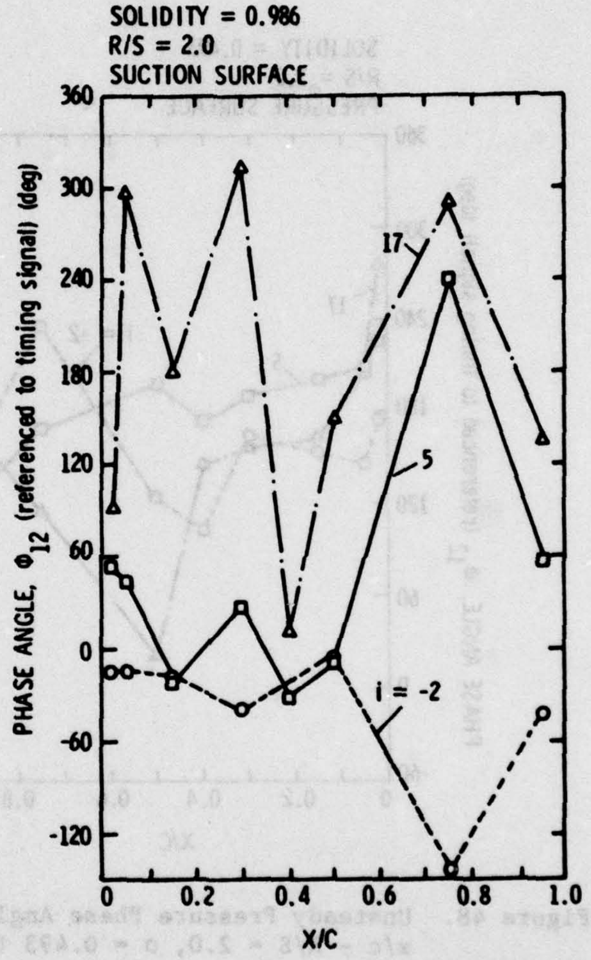

Figure 49. Unsteady Pressure Phase Angle versus x/c - R/S = 2.0, σ = 0.986

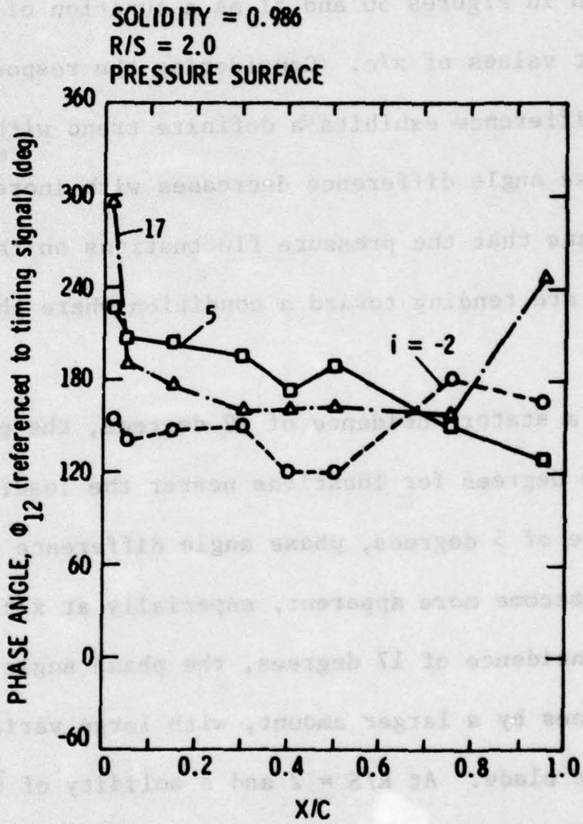

Figure 49. Unsteady Pressure Phase Angle versus x/c - R/S = 2.0, σ = 0.986 (Continued)

The phase angle ϕ for n = 12 and n = 24 can be used to compute the difference in phase angle between the pressure and suction surfaces of the blade. This phase angle difference, defined as:

$$\phi_n(\text{suction}) - \phi_n(\text{pressure}) \ , \qquad (6)$$

is shown in Figures 50 and 51 as a function of incidence angle at constant values of x/c. Considering the response when n = 12, this phase angle difference exhibits a definite trend with incidence angle in which the phase angle difference decreases with increasing incidence angle. This means that the pressure fluctuations on the suction and pressure surface are tending toward a condition where they are in phase with each other.

At a stator incidence of -2 degrees, the phase angle difference is near 180 degrees for locations nearer the leading edge. At stator incidence of 5 degrees, phase angle difference deviations from 180 degrees become more apparent, especially at x/c = 0.15. Finally, at a stator incidence of 17 degrees, the phase angle difference differs from 180 degrees by a larger amount, with large variations between positions along the blade. At R/S = 2 and a solidity of 0.986, for example, $\phi_{12}(\text{suction}) - \phi_{12}(\text{pressure}) = 3$ degrees at x/c = 0.15 indicates that the pressures on opposite sides of the blade are nearly in phase. The phase angle between the suction and pressure surfaces for n = 24, two times blade passing frequency, exhibits the same trends as the phase angle as when n = 12.

As shown in Figure 50, the phase angle difference consistently decreases with increasing incidence and also decreases with distance from the leading edge. While it is not plotted in Figures 51 and 52,

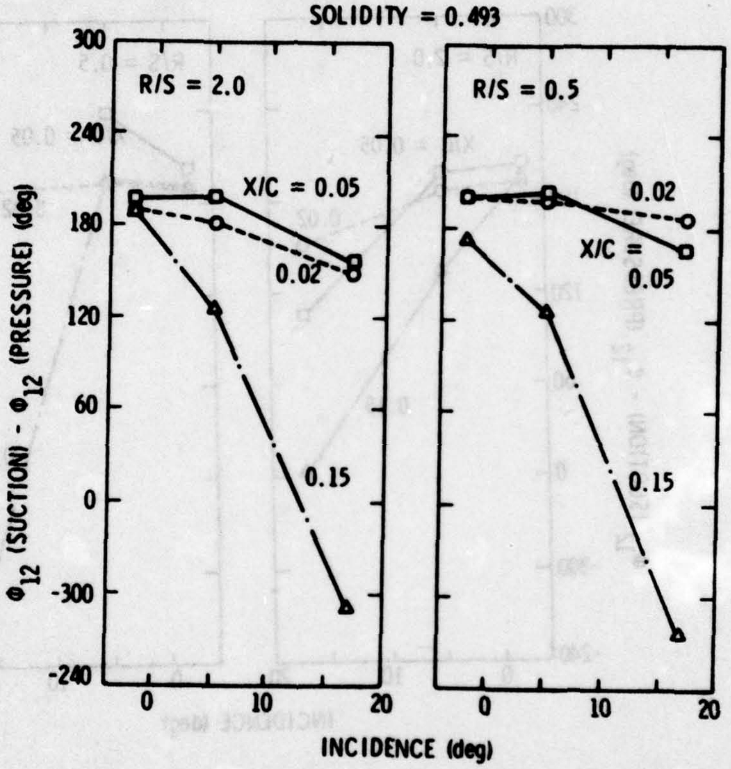

Figure 50. **Suction and Pressure Surface Phase Angle Difference versus Incidence Angle--Blade Passing Harmonic**

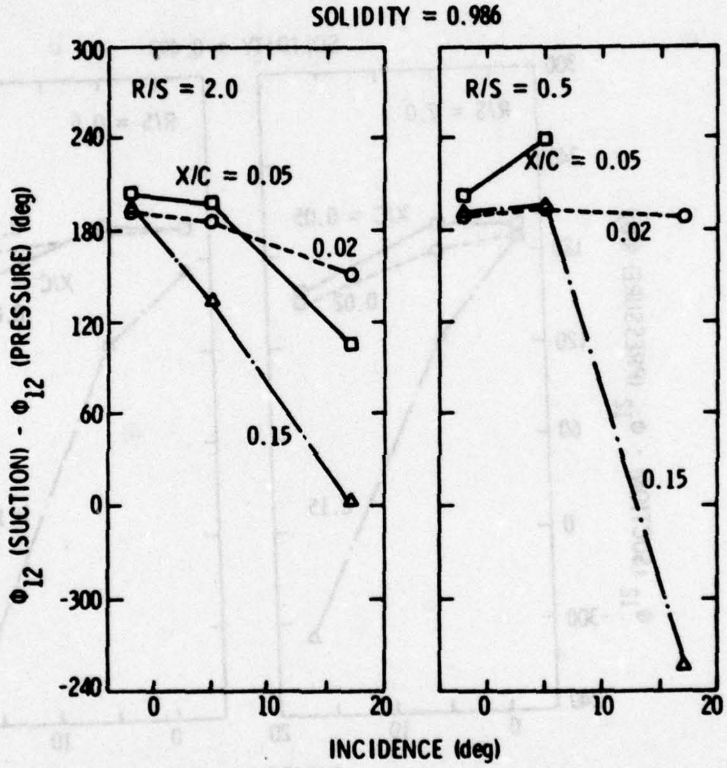

Figure 50. Suction and Pressure Surface Phase Angle Difference versus Incidence Angle--Blade Passing Harmonic (Continued)

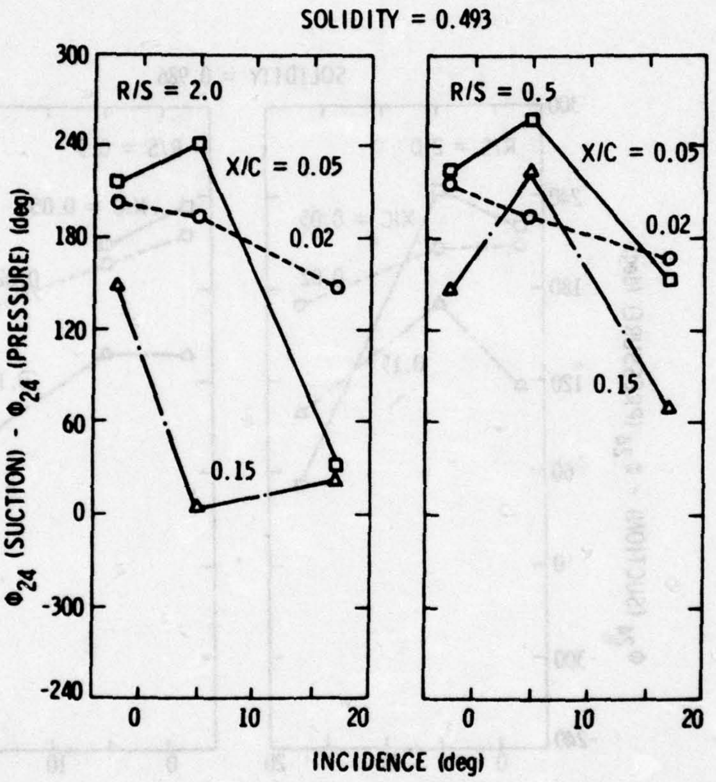

Figure 51. Suction and Pressure Surface Phase Angle Difference versus Incidence Angle--Twice Blade Passing Harmonic

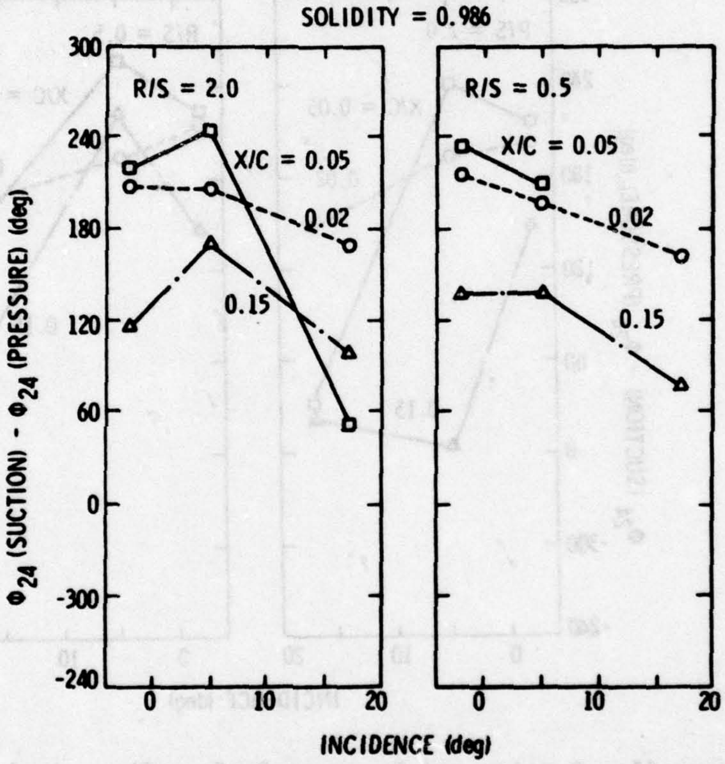

Figure 51. Suction and Pressure Surface Phase Angle Difference versus Incidence Angle--Twice Blade Passing Harmonic (Continued)

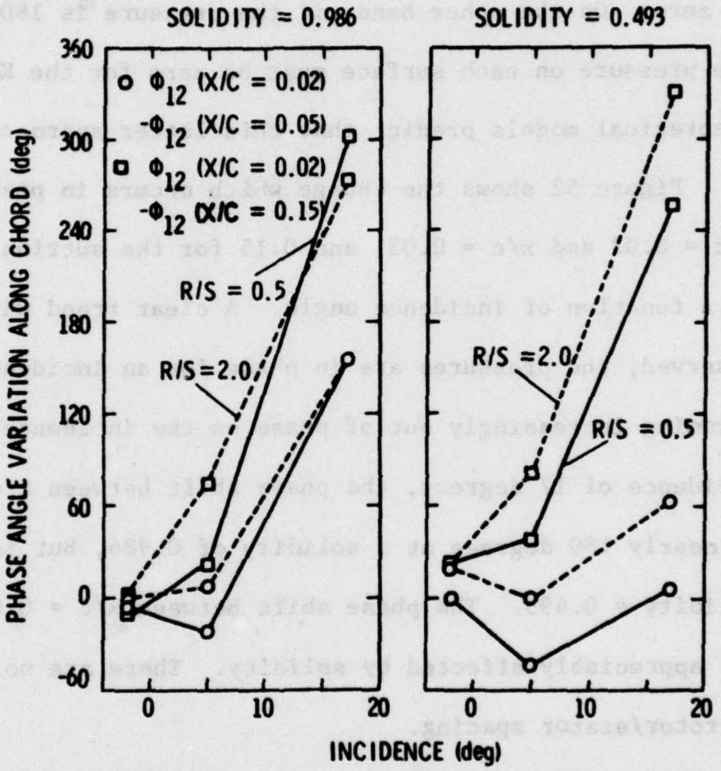

Figure 52. Relative Phase Angle Along Suction Surface with Incidence Angle--Blade Passing Harmonic

examination of Figures 46 through 49 indicates that the phase angle difference between the suction and pressure surfaces approaches zero at the trailing edge. This demonstrates the manner in which the Kutta condition that the pressure difference at the trailing edge, $\Delta p(TE)$, is satisfied. If the pressures on the suction and pressure surfaces are in phase, then a pressure can exist on both surfaces but their difference is zero. On the other hand, if the pressure is 180 degrees out of phase, the pressure on each surface must be zero for the Kutta condition to hold. Theoretical models predict that this latter approach is realized.

Figure 52 shows the change which occurs in phase angle between $x/c = 0.02$ and $x/c = 0.05$, and 0.15 for the suction side of the blade as a function of incidence angle. A clear trend with incidence is observed; the pressures are in phase for an incidence of -2 degrees and becoming increasingly out of phase as the incidence increases. For an incidence of 17 degrees, the phase shift between $x/c = 0.02$ and $x/c = 0.05$ is nearly 180 degrees at a solidity of 0.986, but is quite small at solidity = 0.493. The phase shift between $x/c = 0.02$ and $x/c = 0.15$ is not appreciably affected by solidity. There are no apparent effects due to rotor/stator spacing.

Because of the large number of variables in this test program, it is necessary to summarize the response of the stator blades to these variables. Since the pressure traces described above indicate that the major contribution of the wakes to the unsteady pressure on the stator occurs at the leading edge of the blades, those variations at $x/c = 0.02$ have been used to characterize the behavior of the entire blade. The trend of the unsteady pressures at $x/c = 0.05$ and 0.15 are similar.

Rather than considering the variation of pressure on each surface, the difference in pressure between the suction and pressure surfaces is used. This quantity is related to the magnitude of the unsteady lift, or the pressure dipole, at the blade leading edge. This pressure difference is defined as the RMS of the magnitude of the peak-to-peak variation. Thus, a pressure coefficient, $C_{P_{rms}}$, is defined as:

$$C_{P_{rms}} = \frac{\Delta P_{rms}}{\rho W_{max} V} = \frac{0.707}{\rho W_{max} V} \times \left\{\tfrac{1}{2}(\tilde{p}_{suction} - \tilde{p}_{pressure})_{peak\text{-}to\text{-}peak}\right\} . \tag{7}$$

Figures 53, 54, 55, and 56 present the variation of $C_{P_{rms}}$ as a function of rotor/stator spacing, solidity, incidence angle, and chordwise location, respectively.

These trends in the data should be considered, however, in the light that only two values of rotor/stator spacing and solidity were evaluated. As previously mentioned, the unsteady pressure response decreases rapidly with location along the chord. At $x/c = 0.15$, $C_{P_{rms}}$ is generally about 1/4 the value of $C_{P_{rms}}$ at $x/c = 0.02$. The following discussions are based on the trends of $C_{P_{rms}}$ at $x/c = 0.02$. These data indicate that a major effect on $C_{P_{rms}}$ is due to the solidity of the stator blade row. For example, at a low stator solidity, $\sigma = 0.493$, there is little effect of incidence angle and rotor/stator spacing on $C_{P_{rms}}$. However, at $\sigma = 0.986$, there are large effects, particularly at high values of incidence. Further, there is a significant increase in $C_{P_{rms}}$ at 17 degrees incidence for a solidity of 0.986. There appears to be a trend with incidence, Figure 55, which indicates a positive value of incidence angle at a minimum value of $C_{P_{rms}}$ is experienced. This effect is similar to that observed both experimentally and analytically with the unsteady lift on

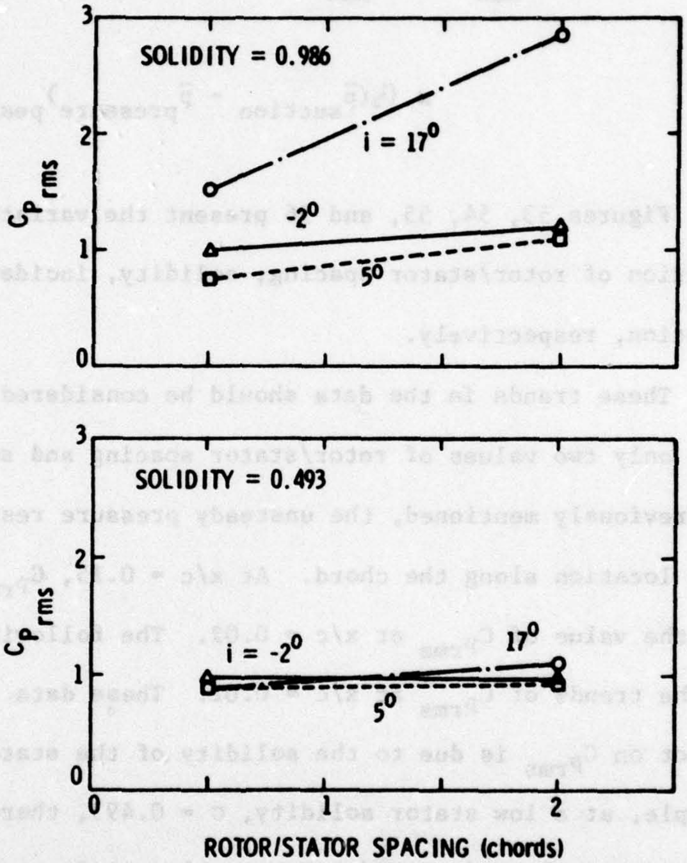

Figure 53. Variation of $C_{p_{rms}}$ with Rotor/Stator Spacing at x/c = 0.02

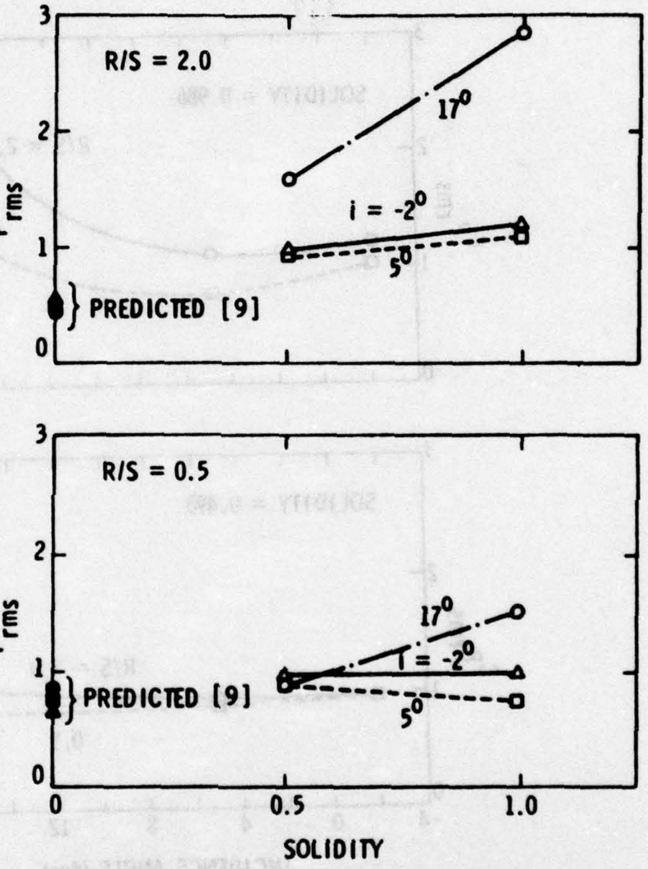

Figure 54. Variation of $C_{p_{rms}}$ with Solidity at $x/c = 0.02$

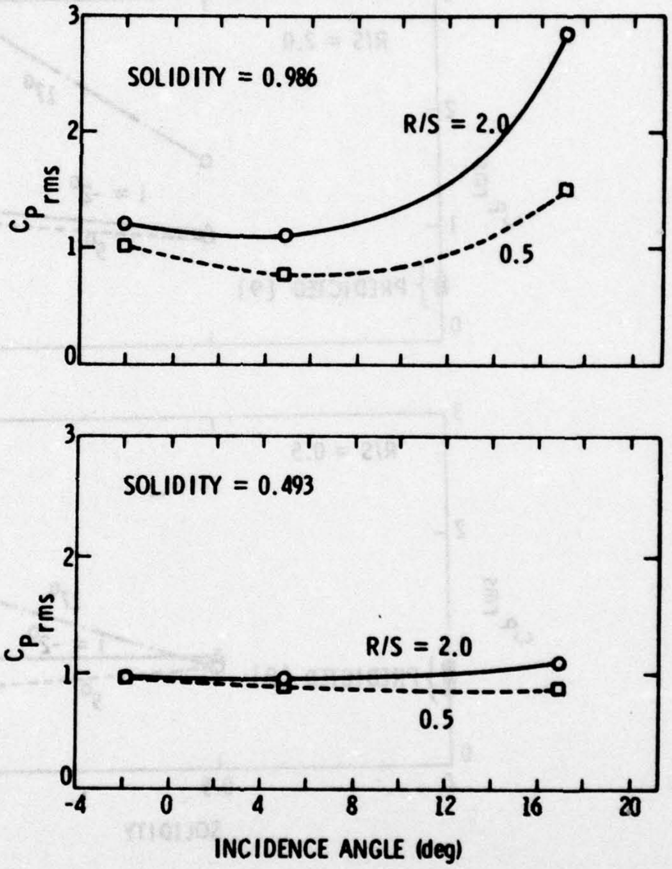

Figure 55. Variation of $C_{P_{rms}}$ with Incidence Angle at x/c = 0.02

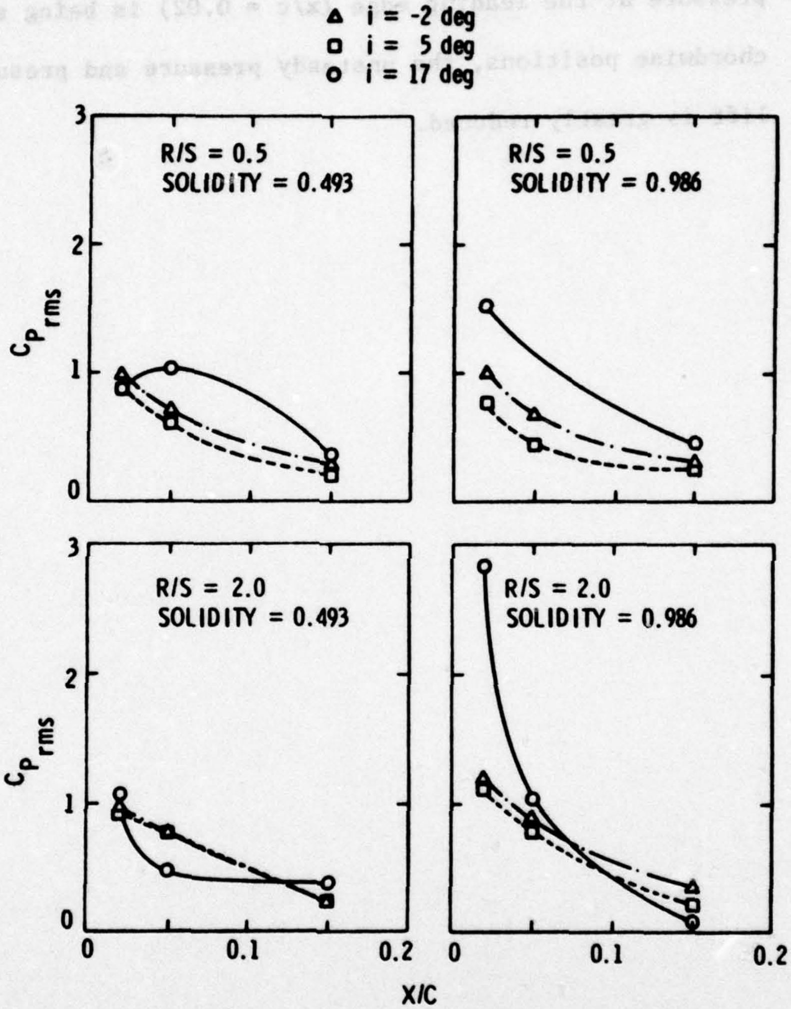

Figure 56. Variation of $C_{P_{rms}}$ with Chordwise Position

a cascade (16) for values of incidence less than 8 degrees. In this case, the unsteady lift decreases with positive incidence due to the existence of a chordwise component of the disturbance velocity. The increase in $C_{P_{rms}}$ at an incidence of 17 degrees is due to the fact that only the pressure at the leading edge ($x/c = 0.02$) is being shown. At other chordwise positions, the unsteady pressure and presumably the unsteady lift is greatly reduced.

COMPARISON OF THEORETICAL AND EXPERIMENTAL RESULTS

Unsteady Stator Pressure Distributions

Ideally, the data measured in this study should be compared with an existing theoretical analysis which predicts the unsteady pressures resulting from the interaction of the wakes of an upstream rotor on the stator blades. If such a comparison shows good agreement then the theoretical analysis could be employed to determine the influence of the various stator geometrical parameters--solidity, stagger angle, camber--on the generation of unsteady pressures for a given rotor wake flow field. However, the existing formulations for predicting the unsteady pressures in a cascade (13, 14) do not consider the interaction of the blades with narrow wakes, but rather a sinusoidal varying inflow, and furthermore, they are not formulated to calculate the unsteady pressures. The only known analysis in which the narrow wake interaction is considered is by Meyer (7). However, it considers only an isolated, two-dimensional airfoil. While there are many dissimilarities between a stator cascade and an isolated airfoil, the data obtained in this study were compared with Meyer's analysis.

Meyer (7) was able to obtain the unsteady pressure distribution of an isolated flat plate airfoil moving through a viscous wake when the flow is assumed to be two-dimensional, incompressible, and inviscid. Since perfect fluid theory (zero viscosity) cannot account for the formation of viscous wakes or their dissipation, a description of the wakes must be supplied from another source. The wake is analyzed as a region containing vorticity, but governed by the vortex laws of perfect fluids theory.

For lightly-loaded, thin airfoils, the equations of motion may be linearized. The effects of camber, blade thickness, and angle of attack of the main flow (outside of the wakes) may be calculated separately and the results superimposed on the solution for flow at zero angle of attack on a flat plate.

Meyer (7), however, considered a flat plate at zero angle of attack with the geometry shown in Figure 57. (Meyer's configuration with an upstream stator can be applied to a downstream stator arrangement by a careful interchange of velocity.) The wake axis, a line connecting the points of maximum velocity in the jet, is at an angle β to the airfoil or the blade under consideration. The velocity defect can then be expressed as components parallel and perpendicular to the blade:

$$u_d = -w(\xi) \cos \beta \tag{8}$$

and

$$v_d = w(\xi) \cos \beta \; . \tag{9}$$

It is also assumed that the wake maintains a constant velocity profile and is not distorted by the blade. Using the approximation that the velocity defect is small compared to the velocity relative to the blade outside of the wake, V, and neglecting terms of higher order, Meyer simplified the momentum equation to obtain:

$$\left(\frac{\partial}{\partial t} + V \frac{\partial}{\partial x}\right)\zeta = 0 \; , \tag{10}$$

where ζ is the total vorticity. The analysis is also restricted to thin wakes; i.e., if:

$$\lambda = \frac{2b}{c \sin \beta} \; , \tag{11}$$

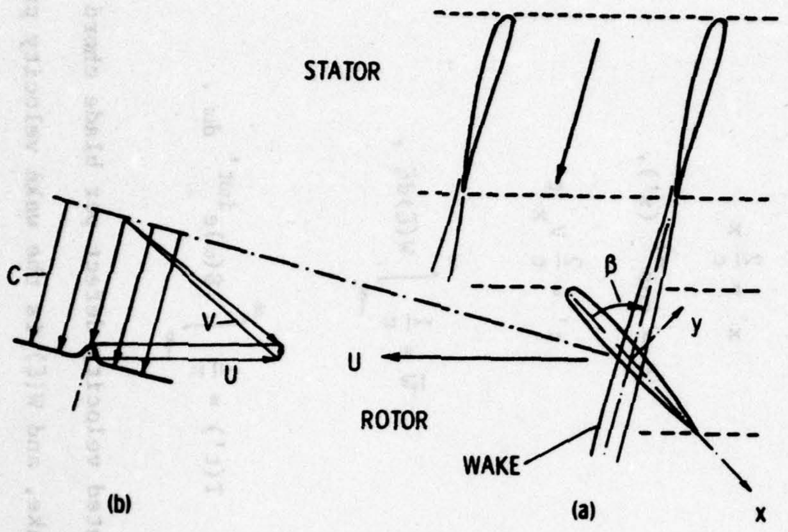
STATOR
C
V
U
U
β
y
ROTOR
WAKE
x
(b)
(a)

Figure 57. Compressor Blade Wake Interaction Considered by Meyer (7)

where 2b is the wake thickness where the wake velocity defect is one-half of the maximum defect, the analysis requires that $\lambda << 1$.

Meyer developed the following expression for the unsteady pressure assuming infinitely thin wakes:

$$\tilde{p}(\theta,\ t') = \pm\rho V\ \overline{W}T(t')\tan(\theta/2)\ , \tag{12}$$

where ± refers to the pressure and suction side of the blade, respectively. This expression uses the nondimensional quantities:

$$x' = \frac{2}{c}\,x\ , \tag{13}$$

$$\theta = \cos^{-1}\,(x'), \tag{14}$$

$$t' = \frac{2}{c}\,V_x\ t \tag{15}$$

and

$$\overline{W} = \frac{1}{c}\int_{-\infty}^{\infty} W(\xi)d\xi\ , \tag{16}$$

where

$$T(t') = \frac{1}{\pi}\int_{-\infty}^{\infty} S(\omega)e^{i\omega t'}\ d\omega\ . \tag{17}$$

$\overline{W}$ is the integrated velocity defect per blade chord and represents the effect of the wake, and $W(\xi)$ is the wake velocity profile where the variable ξ is the distance measured from the wake centerline. The component of the wake profile, $W(\xi)$, parallel to the blade is ignored and the function $S(\omega)$ is the familiar Sears function. The nondimensional time t' has the value -1 when the wake is at the leading edge of the airfoil and +1 when the wake reaches the trailing edge. The function T(t') has the value zero for $t' < -1$. At $t' = -1$, T(t') has a singular point in the pressure distribution at the leading edge in steady flow. For $-1 < t' < \infty$, $T(t')$ decreases monotonically to zero at ∞, indicating that the wake has a decreasing influence as it passes the leading edge and travels downstream.

Lefcort (9) extended Meyer's analysis for wakes of finite but small thickness by superimposing the solutions of many infinitely thin wakes and determined that:

$$\tilde{p}(\theta, t_0') = \pm\rho V \tilde{W}(t_0')\tan(\theta/2) , \qquad (18)$$

where

$$\tilde{W}(t_0') = \tfrac{1}{2} \int_{-\infty}^{\infty} W(\xi')T(t_0' + \xi')d\xi' . \qquad (19)$$

The nondimensional time t_0' is similar to the previously used t' but refers to the centerline of the wake. The nondimensional distance ξ' is defined as:

$$\xi' = \frac{2}{c}\xi . \qquad (20)$$

The equations for $\tilde{p}$ state that the pressure distribution on a flat plate remains similar at all times and does not depend on the shape of the wake. The function $T(t')$ is tabulated by Meyer (7) and more extensively by Lefcort (9).

Several aspects of the theory will be considered: the magnitude of the unsteady pressures and the shape of the pressure distribution; specifically, the decrease in magnitude with location along the chord. The expression for $\tilde{p}$, Equation (4), states the chordwise variation of the unsteady pressure depends only on tan $(\theta/2)$ and the time variation depends only on $T(t_0')$. Therefore, the unsteady pressure at any location on the blade is similar to but different in magnitude from all other locations at each instance in time.

The unsteady pressures on the pressure and suction side of the blade at a constant value of x/c are predicted to be opposite in signs; i.e., 180 degrees out of phase and equal in magnitude. The validity of the prediction that pressures on opposite sides of the blade are 180 degrees out of phase has been previously discussed. At locations near the leading edge, the pressures are nearly 180 degrees out of phase. The phase angle changes at other locations on the blade. This deviation from 180 degrees increases with increasing incidence angle.

The peak-to-peak magnitude of the measured pressure coefficient, $\tilde{p}/\rho W_{max} V$, summarized in Figure 58, shows the magnitude of the pressure coefficient on the suction and pressure side of the blade to be equal only at an incidence of -2 degrees, at the position $x/c = 0.02$ and with a solidity of 0.986. The pressure coefficients are within 10% of each other for these conditions with a solidity of 0.493. At all other positions on the blade and all other incidences, the magnitude of the coefficients are not equal. This demonstrates, as would be expected, that the influence on angle of incidence is to make the pressures on the suction and pressure surfaces unequal. If Meyer's analysis were altered to include the effects of angle of incidence, at best, it would predict the difference in pressure between the suction and pressure surfaces.

A comparison of the chordwise variation of the measured and predicted pressure difference across the blade, $C_{P_{rms}}$ [defined by Equation (6)], is shown in Figure 59 for a rotor/stator spacing of two chord lengths, a solidity of 0.986, and an incidence of -2 degrees. This comparison indicates that the shape of the variation of $C_{P_{rms}}$ along the chord from both the theory and the experiment are somewhat similar. The

Rotor/ Stator Spacing	Stator Solidity	Stator Incidence	$(\tilde{p}/\rho W_{MAX} V)_{peak-to-peak}$					
			x/c = 0.02		x/c = 0.05		x/c = 0.15	
			Suction	Pressure	Suction	Pressure	Suction	Pressure
2.0	0.986	-2	1.67	1.69	1.07	1.44	0.33	0.68
2.0	0.986	5	1.97	1.14	1.02	1.15	0.26	0.53
2.0	0.986	17	7.17	0.90	2.67	0.96	0.35	0.60
0.5	0.986	-2	1.43	1.40	0.78	1.14	0.28	0.60
0.5	0.986	5	1.38	0.77	0.93	0.48	0.37	0.35
0.5	0.986	17	3.46	0.84	2.38	----	0.75	0.89
2.0	0.493	-2	1.43	1.29	0.95	1.25	0.23	0.52
2.0	0.493	5	1.65	1.00	1.16	1.00	0.41	0.48
2.0	0.493	17	2.47	0.62	0.85	0.46	1.13	0.27
0.5	0.493	-2	1.31	1.43	0.82	1.17	0.27	0.52
0.5	0.493	5	1.64	0.85	1.09	0.65	0.39	0.28
0.5	0.493	17	1.83	0.63	1.98	0.95	0.95	0.47

Figure 58. Summary of Measured Peak-to-Peak Pressure Coefficients for x/c = 0.02, 0.05, and 0.15

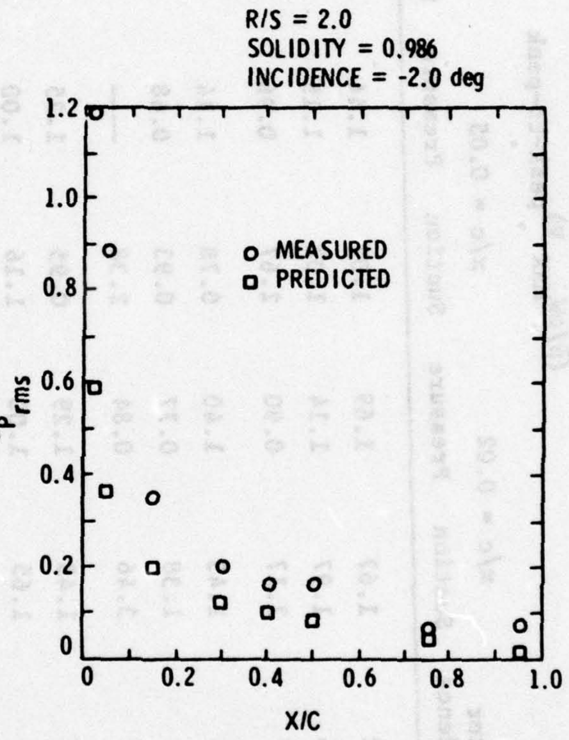

Figure 59. Comparison of Measured and Predicted $C_{P_{rms}}$

magnitude of the unsteady pressure difference, $C_{p_{rms}}$, at $x/c = 0.02$ predicted by theory is less than the measured value and are compared in Figure 60. The predicted value is generally about one-half the measured value. However, the predicted values are for an isolated airfoil, zero solidity. When these predicted values are compared with the variation of $C_{p_{rms}}$ with solidity (see Figure 54), it appears that the measured data are tending to the predicted value at $\sigma = 0$.

The parameter, λ, required to be much less than one in the development of the theory, varies from 0.15 at rotor/stator spacing of 2.0 to 0.07 at rotor/stator spacing of 0.5. Thus, the condition that $\lambda << 1$ has been fulfilled by the experimental data.

In general, the comparison of the measured unsteady pressures in a cascade with the isolated airfoil analysis by Meyer (7) is poor. The variation in measured data with rotor/stator spacing is a function of the wake flow interacting with the blades and represents the input to either a cascade or isolated airfoil analysis. On the other hand, the influence of solidity and the chordwise component of the wake are not included in Meyer's analysis. The present data indicate that: (1) at large angles of incidence which give an appreciable chordwise wake component, the chordwise component does indeed contribute, Figure 55; and (2) the solidity of the cascade does influence the unsteady pressures on the blades, Figure 54. Additionally, although not investigated in this study, there will be an influence of stagger angle as demonstrated by Satyanarayana's data (17). Thus, a better theoretical model should be developed for the interaction of thin wakes with a cascade of airfoils which includes the effects of the chordwise wake component, blade-to-blade interactions (solidity) and stagger angle.

Rotor/ Stator Spacing	Incidence	Solidity	$C_{p_{rms}}$	
			Measured	Predicted
2.0	-2	0.986	1.19	0.59
2.0	5	0.986	1.10	0.56
2.0	17	0.986	2.85	0.45
2.0	-2	0.493	0.96	0.55
2.0	5	0.493	0.94	0.54
2.0	17	0.493	1.10	0.48
0.5	-2	0.986	1.00	0.66
0.5	5	0.986	0.76	0.72
0.5	17	0.986	1.52	0.84
0.5	-2	0.493	0.97	----
0.5	5	0.493	0.68	----
0.5	17	0.493	0.87	0.76

Figure 60. Comparison of $C_{p_{rms}}$ Measured and Predicted at x/c = 0.02

Unsteady Rotor Force and Moment

The potential interaction between the moving rotor blades and the stationary stator blades generates an unsteady force and moment on each blade row. Using the instrumented rotor blade discussed above, measurements of the rotor unsteady lift and moment were made. The test variables were identical to those in the previously described measurements of the unsteady pressures on the stator blades. Measurements of the unsteady lift and moment were first made in the absence of unsteady potential flow effects by operating the rotor with the stator blades removed. In this condition, the output from the strain gauge instrumented rotor would result from: structural vibration, viscous wakes from the three center shaft support struts located far upstream of the rotor, turbulence in the rotor inflow, and any unsteadiness or steady circumferential flow distortion in the supposed uniform inlet flow. These data are used as a background reference, to be subtracted from data measured with the stator blades installed, thus establishing potential flow interactions.

All of the unsteady lift and moment data were ensemble-averaged using 100 sums and then Fourier analyzed. The strongest potential interaction would be obtained with the smallest rotor/stator spacing and highest steady loading (10). The magnitude of the Fourier coefficients of the unsteady lift, or normal force for this condition (rotor/stator spacing of 0.5 and stator incidence of 17 degrees) and the coefficients of the background are shown in Figure 61. These coefficients are shown as the gauge output voltage; the sensitivity of the gauge (static as well as dynamic characteristics) has not been included to give a force level. The magnitude of the fourth coefficient, with four stator blades installed, and the magnitude of the eighth coefficient with 8 stators

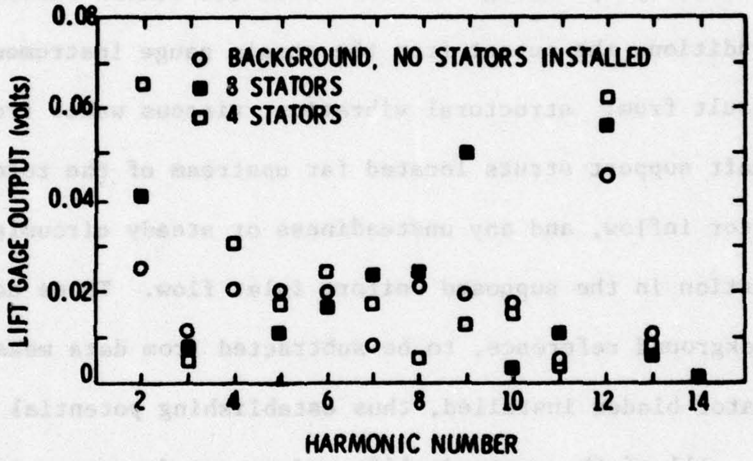

Figure 61. **Magnitude of Unsteady Lift Gauge Output versus Harmonic Number, R/S = 0.5 and i = 17 deg**

installed, is only slightly larger than the background levels. The magnitude of other coefficients such as the twelfth are sometimes greater than, sometimes less than the background. This indicates the magnitude of the unsteady lift, and similarly, the unsteady moment, is not sufficient to be resolved from the background. The magnitudes of the unsteady lift and moment at other rotor/stator spacings and incidence were also too small to be meaningfully measured.

These data indicate that the potential interaction is very small and, indeed, negligible as compared with the unsteady interactions caused by wake interactions. This is based on the fact that this strain gauge system has successfully measured the unsteady lift and moment in a spatially varying inflow (16).

SUMMARY AND CONCLUSIONS

The purpose of this study was to investigate the unsteady response of a stator blade caused by the interaction of the stator with the wakes of an upstream rotor. A major portion of this effort was the development of an instrumented stator to allow the measurement of the unsteady pressures on both its pressure and suction sides during such an interaction. This development was successfully completed and a series of measurements were conducted to demonstrate the effects of (1) rotor/stator spacing, (2) stator solidity, and (3) circumferential time-mean incidence angle on the unsteady pressures.

The following conclusions are drawn regarding the instrumentation employed in this study:

1. The range of pressure transducers used in this study was adequate to measure unsteady pressures on the blades of the Axial Flow Research Fan. The largest peak-to-peak pressure generated by a viscous wake was $\tilde{p}/\rho W_{max} V = 7.25$ which corresponds to a value of $\tilde{p}$ equal to 2.75 cm of water. The pressures actually experienced by the transducer were larger than this value due to the presence of perturbations which were not periodic with the rotor rpm. These pressure perturbations were eliminated by ensemble averaging. Peak-to-peak pressures as small as $\tilde{p}/\rho W_{max} V = 0.25$, which corresponds to a value of $\tilde{p}$ equal to approximately 0.095 cm of water, could be discerned in the plotted output.

2. The Pitran pressure transducers were adequate to conduct the required measurements. Several disadvantages, however, indicate the desirability of continuing to investigate alternate pressure transducers. The most severe disadvantage was the Pitran's susceptibility to electrical interference. Much effort was spent (unsuccessfully) trying to eliminate 60 Hz interference and high frequency electromagnetic pickup from the SCR's in the rotor and auxiliary fan motor controllers. The Pitrans were also very fragile and susceptible to mechanical damage; the calibration constant could change if the blade was disassembled and reassembled. Additionally, because of their temperature sensitivity, the D.C. output of the Pitran must be electrically cancelled which means that the time-mean pressure cannot be measured.
3. The ensemble-averaging technique employed was necessary to permit the analysis of these data. Random fluctuations and unsteady pressures which are not periodic with the rotor can be successfully eliminated by this technique.
4. The strain gauge instrumented rotor blade and associated signal conditioning did not have sufficient sensitivity to measure the rotor/stator potential interaction. Based on earlier measurements with this rotor blade, it is concluded that

the unsteady lift caused by potential interactions is significantly less than the blade-wake interaction unsteady lift.

5. The distribution of pressure sensing ports should be more heavily weighted toward the leading edge of the blade since the major changes in unsteady pressure occur at the leading edge.
6. The arrangement of a cavity-surface tap was well suited to measure the unsteady pressures. The cavity-surface tap arrangement can be designed to avoid cavity resonance problems. Thus, the difficulties of using flush-mounted transducers on a curved surface can be avoided.

From the unsteady pressure measurements obtained, it is concluded that:

1. A major effect on the unsteady stator pressure is due to the solidity of the stator blade row. At a low solidity, 0.493, $C_{P_{rms}}$ was observed to be relatively insensitive to rotor/stator spacing and stator incidence angle. At a solidity of 0.986, there are large effects due to the change in rotor/stator spacing and incidence. At the higher solidity, the blade-to-blade interactions have a larger contribution.
2. There is a positive value of the angle of incidence that minimizes $C_{P_{rms}}$. This agrees with the trends

predicted by both unsteady isolated airfoil and cascade analyses in which the effects of angle of attack are considered.

3. The range of rotor/stator spacing investigated has a weak influence on $C_{P_{rms}}$. $C_{P_{rms}}$ was slightly higher at a spacing of two chord lengths. This indicates a minor change in the wake characteristics in this range of rotor/stator spacing.
4. The phase angle of the unsteady pressure fluctuations on the blade shows significant variation on the suction surface while being relatively constant on the pressure surface. With increasing angle of incidence, the variations on the suction surface become much larger. It is suspected that this is due to local flow separation.
5. The difference in phase angle between the suction and pressure surfaces of the blades is approximately 180 degrees at the leading edge of the blade and tends to zero degrees at the trailing edge.
6. The Kutta condition can be satisfied at the trailing edge of the blade by the existence of a nonzero value of pressure on the suction and pressure surfaces of the blade. In this case, the surface pressures are in phase and equal in magnitude, thus giving a zero pressure difference at the trailing edge. This is different than the available theoretical analyses which state that the pressure on each surface is zero and 180 degrees out of phase at the trailing edge.

Several observations concerning the theoretical prediction by Meyer (7) and Lefcort (9), which were compared with the experimental data, are made:

1. The prediction that the unsteady pressures on opposite sides of the blade are 180 degrees out of phase is correct near the leading edge at low values of incidence angle.
2. The prediction that the unsteady pressure on opposite sides of the blade are 180 degrees out of phase is only true at low values of incidence and near the leading edge of the blade. The phase angle between pressures on *opposite sides* of the blade changes significantly with incidence angle. The prediction that the pressure *distribution* is similar at all times is approximately true on the pressure side of the blade and approximately true on the suction side of the blade, but only near the leading edge at low values of incidence. Discrepancies from the prediction increase with increasing incidence angle and increasing distance from the leading edge.
3. The predicted unsteady pressure coefficient is approximately one-half the measured unsteady pressure coefficient. This observation is the opposite of that observed by Ostdiek (24) for a cascade of airfoils at low reduced frequency. However, the measured values of unsteady pressure coefficient appear to approach the predicted values at zero solidity.

4. The prediction that suction and pressure side unsteady pressures are equal in magnitude was only found to be true only at $x/c = 0.02$ with an incidence of -2 degrees and solidity of 0.986 and approximately true at these at $x/c = 0.02$ with a solidity of 0.493. There were large differences at other values of incidence and x/c. This implies that theoretical analyses based on a thin-airfoil analysis can only be used to predict the difference in pressure between the suction and pressure surfaces and not the pressure on each surface.

RECOMMENDATIONS

Based on the experience and results obtained in conducting this study, there are several recommendations which are pertinent to further research conducted regarding the unsteady response of an axial flow fan to spatial inlet flow distortions. These are:

1. The investigation of the response of a stator to the wakes of an upstream rotor, while being a very important problem, does not represent a "clean" experimental setup. As a result, it is difficult to draw hard conclusions regarding the influence of various geometrical and flow characteristics on the unsteady response of the axial flow fan blades. A much "cleaner" experimental setup is that employed in Reference (16) with a rotating blade row and simplified sinusoidal spatial distortions.

2. The detailed measurement of unsteady pressures on the blades of an axial flow fan represent a necessary piece of experimental data to permit the determination of unsteady fan design data. Such data are also important in the development of a knowledge of the boundary layer and wake on a blade which experiences an unsteady interaction. It is necessary then to conduct additional measurements of the unsteady pressures in a test setup similar to that employed in (16), i.e., a rotor blade interacting with the simple sinusoidal spatial distortion.

3. The instrumentation developmented conducted in this study should be extended to provide a rotor blade on which unsteady pressure distribution can be measured. The same basic technique should be employed, except different pressure sensors which are less fragile and temperature sensitive should be employed.
4. Efforts should be made to develop an unsteady cascade analysis which will predict the unsteady pressure distributions while including the influence of solidity, stagger angle, camber, thickness and angle of incidence. This analysis should not be restricted to the prediction of the pressure difference across the blade, but should provide the pressures on each side. The effects of thin wakes such as studied by Meyer (7) and Lefcort (9) should also be included.
5. After verification of this advanced analysis by experiments, it should be used to obtain unsteady design data which demonstrate the influence of blade geometry and flow characteristics.
6. Experimental data should be obtained which demonstrates the behavior of the blade boundary layer, i.e., transition and separation, during the interaction of the blade with a spatial distortion. Such measurements could be obtained with flush mounted hot-film sensors. Additionally,

time varying measurements of the blade boundary layer profile and wake should be obtained to provide a better description of the unsteady blade interaction problem.

REFERENCES

1. Von Karman, T. and Sears, W. R. "Airfoil theory for non-uniform motion." Journal of Aeronautical Sciences, Vol. 5, 1938, pp. 379-390.

2. Sears, W. R. "Some aspects of nonstationary airfoil theory and its practical application." Journal of the Aeronautical Sciences, Vol. 8, No. 3, Jan. 1941, pp. 104-108.

3. Horlock, J. H. "Fluctuating lift forces on aerofoils moving through a transverse and chordwise gusts." ASME Paper No. 68-FE-28, 1968.

4. Horlock, J. H. "Unsteady flow in turbomachines." Presented at the Third Australian Conference on Hydraulics and Fluid Mechanics, Sydney, Australia, Nov. 1968.

5. Nauman, H. and Yeh, H. "Lift and pressure fluctuations of a cambered airfoil under periodic gusts and applications in turbomachinery." Presented at ASME Gas Turbine Conference, Paper No. 72-GT-30, San Francisco, Calif., Mar. 1972.

6. Holmes, D. H. "Lift fluctuations on aerofoils in transverse and streamwise gusts." Ph.D. dissertation, Engineering Department, University of Cambridge, Cambridge, England, Oct. 1972.

7. Meyer, R. X. "The effect of wakes on the transient pressure and velocity distribution in turbomachines." Presented at the ASME Annual Meeting, Paper No. 57-A-83, Dec. 1957.

8. Fujita, H. and Kovasnay, L. S. G. "Unsteady response of an airfoil to 'wake cutting'." The Johns Hopkins University, Baltimore, Md., Dec. 1971.

9. Lefcort, M. D. "An investigation into unsteady blade forces in turbomachines." Presented at the ASME Gas Turbine Power Division Winter Annual Meeting, Paper No. 64-WA/GTP-3, Nov.-Dec. 1974.

10. Kemp, N. H. and Sears, W. R. "Aerodynamic interference between moving blade rows." Journal of Aeronautical Sciences, Vol. 20, 1953, pp. 585-598.

11. Kemp, N. H. and Sears, W. R. "The unsteady forces due to viscous wakes in turbomachines." Journal of Aeronautical Sciences, Vol. 22, 1955, pp. 478-483.

12. Whitehead, D. S. "Vibration of cascade blades treated by actuator disk methods." Proceedings of Institute of Mechanical Engineers, Vol. 173, No. 21, 1959.

13. Whitehead, D. S. "Force and moment coefficients for vibrating airfoils in cascade." Aeronautical Research Council, Great Britain, England, R&M 3254, 1960.

14. Henderson, R. E. and Daneshyar, H. "Theoretical analysis of fluctuating lift on the rotor of an axial turbomachine." Aeronautical Research Council, Great Britain, England, R&M 3684, 1972.

15. Henderson, R. E. "The unsteady response of an axial flow turbomachine to an upstream disturbance." Ph.D. dissertation, Engineering Department, University of Cambridge, Cambridge, England, 1972.

16. Bruce, E. P. and Henderson, R. E. "Axial flow rotor unsteady response to circumferential inflow distortions." AGARD Conference Proceedings on Unsteady Phenomena in Turbomachinery, No. 177, Apr. 1976.

17. Satyanarayana, B. "Unsteady flow past aerofoils and cascades." Ph.D. dissertation, Engineering Department, University of Cambridge, Cambridge, England, 1975.

18. Holmes, D. W. "Lift and measurements of an aerofoil in unsteady flow." Presented at ASME Gas Turbine Conference, Washington, D.C., Paper No. 73-GT-41, Dec. 1974.

19. Bruce, E. P. "The ARL axial flow research fan - a new facility for investigation of time-dependent turbomachinery flows." ASME Paper No. 74-FE-27, 1974.

20. Wislicenus, G. F. Fluid mechanics of turbomachinery. Vols. I and II. New York, N.Y.: Dover Publications, Inc., 1965.

21. Howell, A. R. "The present basis of axial flow compressor design: Part I - Cascade theory and performance." Aeronautical Research Council, Great Britain, England, R&M 2095, 1942.

22. Krohn-Hite Corporation. Operating and maintenance manual. Model 3342. Cambridge, Mass.

23. Bruel and Kjaer. Instructions and applications, half-inch condenser microphones. Naerum, Denmark, 1969.

24. Ostdiek, F. R. "A cascade in unsteady flow." AGARD Conference Proceedings on Unsteady Phenomena in Turbomachinery, No. 177, Apr. 1976.

25. Carta, F. O. and St. Hilaire, A. "Experimentally determined stability parameters of a subsonic cascade oscillating near stall." Presented at the ASME Gas Turbine Conference, Paper No. 77-GT-47, Philadelphia, Pa., Mar. 1977.

26. Wood, A. Acoustics. New York, N.Y.: Dover Publications, Inc., 1966, p. 105.

27. Alster, M. "Improved calculation of resonant frequencies of Hemholtz resonators." Journal of Sound and Vibration, No. 24, 1972, pp. 63-85.

28. Hersh, A. S. and Rogers, T. "Fluid mechanical model of the acoustic impedance of small orifices." NASA CR-2682, 1976.

29. Iberall, A. S. "Attenuation of oscillatory pressures in instrument lines." J. Res. National Bureau of Standards, Vol. 45, No. 1, July 1950, pp. 85-108.

30. Bergh, H. and Tijdeman, H. "Theoretical and experimental results for the dynamic response of pressure measuring systems." National Aerospace Laboratory, The Netherlands, NLR Report F.238, 1965.

31. Baumeister, K. J. and Rice E. J. "Visual study of the effect of grazing flow on the oscillatory flow in a resonator orifice." NASA TM X-3288, 1975.

32. Rogers, T. and Hersh, A. S. "Effect of grazing flow on steady state resistance of isolated square-edged orifices." NASA CR-2681, 1976.

33. Groeneweg, J. F. "Current understanding of Helmholtz resonator arrays as duct boundary conditions." NASA SP-207, pp. 357-368.

34. Tijdeman, H. and Berg, H. "The influence of the main flow on the transfer function of the tube-transducer systems used for unsteady pressure measurements." National Aerospace Laboratory, The Netherlands, NLR Report MP 72023 U, 1972.

APPENDIX A

THEORETICAL RESPONSE OF TUBE-CAVITY SYSTEMS

The theoretical analysis of a tube-cavity system historically began with the classic resonator analogy. Similar to a mass on a massless spring, the significant fluid mass is assumed concentrated in the tube of the resonator, and the volume of the cavity acts as a massless spring, Figure A-1. This system is commonly known as a Helmholtz resonator. The resonant frequency is given in various references, e.g., (26) as

$$f_{resonant} = \frac{1}{2\pi}\sqrt{\frac{\pi d^2 c^2}{V(L+E)}}$$

where d is the tube diameter, c is the speed of sound, L is the tube length and V is the cavity volume. The end correction, E, is added to account for the motion of the fluid outside the tube. The end correction is generally taken as 0.3d.

Alster (27) improved the basic model by considering the effects of motion of mass particles inside the cavity and was able to show the resonant frequency depends on the shape of the interior cavity.

Hersh and Rogers (28) have an excellent discussion of the progress made in theoretical analysis of tube-cavity systems and of orifices. The behavior of an orifice, similar to a tube-cavity system having a tube of negligible length, is frequently described in terms of its impedance. Impedance is a complex quantity consisting of resistance and reactance. The magnitude of impedance is given by the ratio of cavity pressure to the orifice velocity. For orifices, two regimes may be considered. In the linear regime, which exists at low driving pressures, the reactance portion of the impedance is much greater than the resistance. The orifice

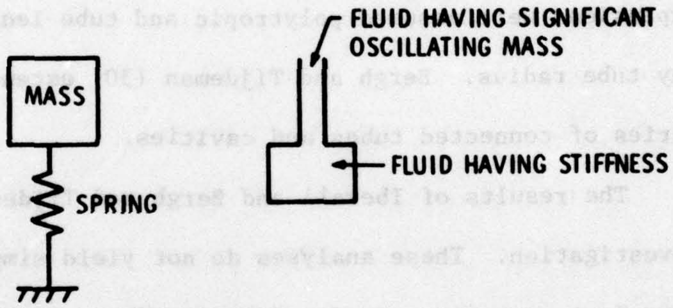
FLUID HAVING SIGNIFICANT OSCILLATING MASS
MASS
FLUID HAVING STIFFNESS
SPRING

Figure A-1. Cavity-Tube Model

impedance is essentially independent of incident pressure. In the nonlinear regime, at sufficiently high driving pressure, the fluid separates at the orifice and forms a jet. The orifice impedance can be related to a time-average discharge coefficient. Although these results are not directly applicable to tube-cavity systems, it is reasonable to expect some similarities between the fluid mechanics of orifices and of tube-cavity systems.

Iberall (29) derived the tube-cavity response using the equations of momentum, energy, continuity, and state. The flow is assumed laminar everywhere in the system with small sinusoidal pressure variations. Expansions were assumed polytropic and tube lengths are long compared to any tube radius. Bergh and Tijdeman (30) extended this analysis to a series of connected tubes and cavities.

The results of Iberall and Bergh and Tijdeman are used in this investigation. These analyses do not yield simple expressions and, therefore, are not reproduced here. The resonant frequency predicted by Iberall, by the classical Helmholtz resonator theory, and the resonant frequency indicate by dynamic calibration are shown in Figure 14. The uncertainty of the resonant frequency in the dynamic calibration indicated in Figure 14 is only a rough estimate based on the increment in driving frequency used in the dynamic calibration. Despite wave reflection effects mentioned in the discussion of the calibration setup, the resonant frequencies indicated by the dynamic calibration agree reasonably well with the values predicted by Helmholtz and Iberall. The dynamic sensitivity of the Pitran transducer at low frequencies is generally within 2 dB of the statically determined value.

The presence of flow parallel to the blade surface influences the tube-cavity response. The momentum of the tube inflow or outflow interacts with the momentum of the parallel flow past the blade. Baumeister and Rice (31) used thin streams of dye to observe streamlines in the parallel flow and in the tube flow. The parallel flow can act to restrict the tube outflow, or the streamline from the parallel flow can center the tube during inflow. Thus, flow conditions are different for inflow and outflow. Rogers and Hersh (32) modeled the effect of a flow parallel and orifice subject to high pressure levels and found good agreement with experimental data.

Groeneweg (33) shows predicted and experimental data for resistance of a Helmholtz resonator versus Mach number of the parallel flow, Figure A-2. For conditions generally encountered in the AFRF, Mach number less than 0.06, the effect was small.

Tijdeman and Bergh (34) presented similar data. They also modeled the effect of the parallel flow and developed an expression describing the response of the tube-cavity in the presence of parallel flow. Using an experimentally determined coefficient, good agreement was found between theory and experiment, Figure A-3. The effect for conditions encountered in this investigation is small.

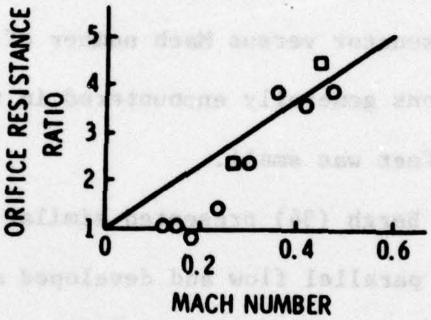

Figure A-2. Orifice Resistance Ratio versus Mach Number (33)

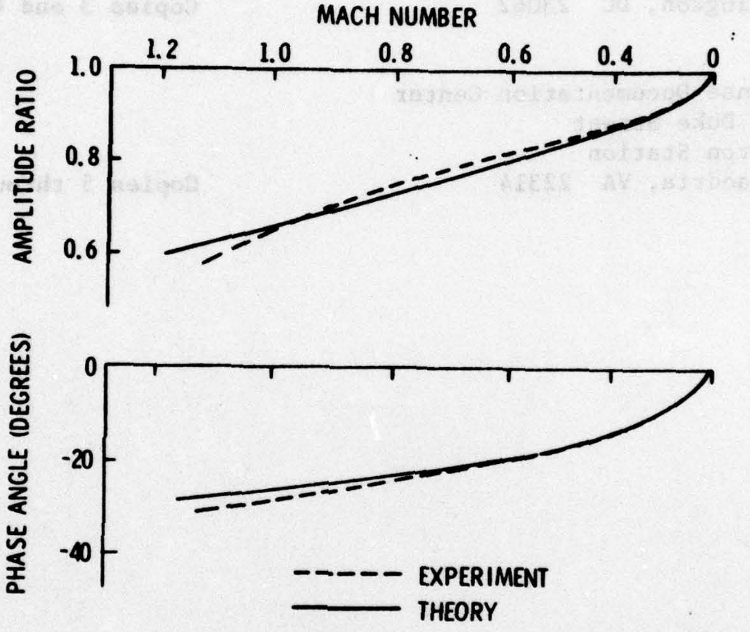

NOTE: INPUT FREQUENCY IS APPROXIMATELY
ONE HALF OF RESONANT FREQUENCY
FOR THE CONDITION SHOWN

Figure A-3. Mach Number Effects on Cavity-Tube Response (34)

DISTRIBUTION

Commander (NSEA 09G32)
Naval Sea Systems Command
Department of the Navy
Washington, DC 20362 — Copies 1 and 2

Commander (NSEA 0342)
Naval Sea Systems Command
Department of the Navy
Washington, DC 23062 — Copies 3 and 4

Defense Documentation Center
5010 Duke Street
Cameron Station
Alexandria, VA 22314 — Copies 5 through 16